Final Report:

Passive Calibration of the Backscattering Coefficient of the Envisat RA-2

PREPARED by: Nazzareno **Pierdicca**, Christian **Bignami**, Luca **Pulvirenti**, *Dept. Electronic Engineering – University La Sapienza of Rome, Italy*

Piero **Ciotti**, Frank Silvio **Marzano**, *Dept. of Electrical Engineering - Univ. of L'Aquila, 67040 Poggio di Roio, L'Aquila, Italy*

Patrizia **Basili**, Vinia **Mattioli**, Stefania **Bonafoni**, *Dept. of Electronic and Information Engineering - Univ. of Perugia, Italy*

Paolo **Ferrazzoli**, Giovanni **Schiavon**, Leila **Guerriero**, *Dept of Informatics, Systems and Production - University Tor Vergata of Rome, Italy*

APPROVED by: Nazzareno **Pierdicca**, *Dept. Electronic Engineering – University "La Sapienza" of Rome, Italy*

Acronyms and abbreviations

CFI	Customer Furnished Item
ECMWF	European Centre for Meteorological and Weather Forecasts
ESA	European Space Agency
FTP	File transfer protocol
MWR	Microwave Radiometer, on-board ERS and ENVISAT satellites
PTN	Point Target Noise response (no-echo operation mode of the RA)
RA	Radar Altimeter, on-board the ERS satellites
RA-2	Radar Altimeter 2, on –board the ENVISAT satellite
SOW	Statement of Work
UTC	Universal Time Co-ordinated
WBS	Work Breakdown Structure
WP	Work Package
DIE	Dept. Electronic Engineering, University La Sapienza of Rome
DISP	Dept. Computer, System and Industrial Engineering, University of Tor Vergata
SAP	University La Sapienza of Rome
TOV	University of Tor Vergata
DC	Digital Counts
ATMO	Atmospheric
Tmr	Atmospheric Mean Radiative Temperature
TOA	Top Of the Atmosphere
TB	Brightness Temperature
tau	Atmospheric Opacity
TRMM	Tropical Rainfall Measuring Mission
TMI	TRMM Microwave Imager
DMSP	Defence Meteorological Satellite Program
SSM/I	Special Sensor Microwave / Imager
CLS	

Applicable documents

PO-TR-ALS-RA-0042, Issue 4, date 01/12/99, ANNEX 7: Instrument characterization data, Alenia Spazio
PO-NT-RAA-004-CLS, Issue 2, Rev. 1, 14/11/97, Algorithm Definition and Accuracy, CLS

TABLE OF CONTENT

1.0 INTRODUCTION **6**

2. 0 GENERAL REQUIREMENTS FOR PASSIVE CALIBRATION **6**

2.1 PROJECT OVERVIEW **6**

2.1.1 PHASE-1 ACTIVITY 7
2.1.2 PHASE-2 ACTIVITY 8

2.2 MODEL DESIGN AND IMPLEMENTATION **9**

2.2.1 MODEL DESIGN 9
2.2.2 ATMOSPHERE MODELS 10
2.2.3 SEA MODELS 11
2.2.4 LAND MODELS 12
2.2.5 CANDIDATE INPUT DATA 12

2.3 CALIBRATION AREAS **15**

3.0 ATMOSPHERIC MODELS **18**

3.1 INTRODUCTION **18**

3.2 RANGE OF EXPECTED VALUES, AND SENSITIVITY TO FREQUENCY AND MAIN INPUT DATA **18**

3.3 ON-LINE INPUT DATA **27**

3.4 ALGORITHMS FOR τ, TMR (UP AND DOWN) AND RAIN FLAG **27**

3.4.1 USING CONVENTIONAL DATA 27
3.4.2 USING REMOTELY SENSED DATA 28

3.5 PROCESSED DATA AND RESULTS **36**

3.6 VALIDATION AND PRODUCT ACCURACY ESTIMATES **37**

4 SEA MODEL **41**

4.1 INTRODUCTION **41**

4.2 DESCRIPTION OF THE "TWO SCALE MODEL" FOR SEA EMISSION **41**

4.3 SENSITIVITY TO MAIN INPUT AND MODEL PARAMETERS **43**

4.3.1 SEA WATER SALINITY 43
4.3.2 FOAM MODELING IMPACT 44
4.3.3 ECMWF SEA SURFACE DATA 46

4.4 DEVELOPMENT OF MICROWAVE SEA EMISSIVITY MODEL FUNCTIONS **48**

4.5 COMPARISON WITH LITERATURE MODELS **49**

4.5.1 S BAND MODEL 50
4.5.2 WENTZ MODEL 50

4.6 VALIDATION AND TUNING **52**

4.6.1 NEED OF A CLEAR-SKY MASK 52
4.6.2 PHASE 1 VALIDATION 54
4.6.2 PHASE 2 VALIDATION AND FINAL MODEL SETUP 58
4.6.3 ESTIMATE ACCURACY OF SIMULATED BRIGHTNESS AT KU AND S BAND 60

5.0 LAND MODELS **61**

5.1 SELECTION OF CALIBRATION AREAS **61**

5.2 MODELS DESCRIPTION 61

5.2.1 FOREST 61
5.2.1.1 Electromagnetic characterization of crown *62*
5.2.1.2 Electromagnetic characterization of soil *62*
5.2.1.3 Electromagnetic characterization of trunk *62*
5.2.1.4 Computation of the emissivity *62*
5.2.1.5 Selection of input variables for Amazonian forest *63*
5.2.2 DESERT 63
5.2.3 CONTINENTAL ICE 64

5.3 VALIDATION AND TUNING 64

5.3.1 APPROACH 64
5.3.2 VALIDATIONS WITH SIGNATURES OF YEAR 2000 65
5.3.3 VALIDATIONS WITH SIGNATURES OF YEARS 2002-03 67

5.4 ESTIMATED ACCURACY OF SIMULATED BRIGHTNESS AT KU AND S BAND 69

5.4.1 KU BAND 69
5.4.2 S BAND 69

6 RA-2 RECEIVER CALIBRATION RESULTS 71

6.1 THE RA-2 RECEIVER CHAIN 71

6.1.1 THE PRE-FLIGHT RECEIVER GAIN 74

6.2 THE CALIBRATION APPROACH 75

6.2.1 RA-2 INTERNAL CALIBRATION 75
6.2.2 THE RECEIVER GAIN CALIBRATION EQUATION USING THE PASSIVE APPROACH 76
6.2.2 ANTENNA EFFICIENCY 77
6.2.3 INFLUENCE OF SENSOR TEMPERATURE 78

6.3 OVERVIEW OF RA-2 ACQUISITIONS FOR "PASSIVE CALIBRATION" 79

6.4 THE RA-2 PASSIVE SIGNATURE OF CALIBRATION TARGETS 80

6.5 ESTIMATES OF RA-2 RECEIVER GAINS 81

6.5.1 INTRODUCTION 81
6.5.1 KU BAND 82
6.5.1 S BAND 83

6.6 ERROR BUDGET FOR GAIN ESTIMATION 84

6.7 OVERALL ERROR BUDGET FOR SIGMA NAUGHT ESTIMATION 87

6.8 INTERFREQUENCY BIAS 87

7 CONCLUSIONS 88

REFERENCES 89

APPENDIX A.1 91

APPENDIX A.2 94

APPENDIX A.3 96

1.0 Introduction

The Radar Altimeter 2 (RA-2) on board of the ENVISAT satellite operates in two bands (S and Ku) and is primary conceived to measure the range to the Earth surface. By combining this information with accurate orbit data, it is possible to determine the surface level in a geocentric co-ordinate system (or with respect to a reference ellipsoid). Besides this primary objective, RA-2 is also capable to measure other parameters of the surface, and in particular the backscattering coefficient (sigma nought) at nadir (geodetic pointing). Though the history of spaceborne altimeters goes back to the early seventies, the calibration of the backscattering coefficient has never been done. Historically, this information has been used only to infer the wind speed via an empirical model. Recently, the question of the physical modelling of the sea backscattering became a scientific priority and several methods were discussed to tackle the problem. For these purposes the accuracy is expected to be better then 0.4 dBs and possibly 0.2 dBs. The calibration of sigma nought requires the exact knowledge of all the instrument and observation parameters that appear in the radar equation. They include transmitted power, antenna gain pattern, range and pointing angle, receiver characteristics. During the on-ground testing, the RA-2 has been rather well characterised to ensure its performance in orbit, and that information can be used in ground processing to invert the radar equation and to calculate the sigma nought. As the accuracy of some of these parameters may be not enough for the purpose of sigma nought calibration and/or they may change during the flight, the calibration must be performed by observing radar targets of a well know radar cross section σ (such as transponder calibration devices), or an extended surface of known sigma nought σ°. An accurate calibration exercise was therefore envisaged during the ENVISAT commissioning phase.

This project report regards an innovative technique to calibrate the σ° estimates of RA-2. It has been carried out independently on the other techniques envisaged during the commissioning phase (transponder calibration). This technique is based on the main assumption that the antenna and the transmitter characterization errors during flight are of minor importance for the purpose of σ° calibration. In any case, the transmitted power level is monitored, and its changes can be easily detected. If the altimeter can operate in noise-listening mode, i.e., detecting only the radiation emitted by the observed scenario in the absence of radar echo, the receiver response function can be characterised with techniques similar to those used for spaceborne radiometers.

More specifically, assuming a linear receiver, the digital receiver readout P_{tlm} at the output of the altimeter in noise-listening mode is:

$$P_{tlm} = 10^{\frac{AGC}{10}} G * P_r + R \tag{1.1}$$

where P_r is the received power at the antenna front-end, G is the receiver gain and R is the internal receiver noise, AGC is the Automatic Gain Control (gain setting, in dB). The two unknowns are the parameters G and R; the determination of the above two requires to know the brightness temperature impinging on the RA-2 antenna from the observed scenario related to diverse targets (e.g., water, ice, forest, etc.) generating very different environmental noise. Assuming the targets can be accurately modelled the corresponding P_r is known, whilst P_{tlm} is supplied by RA-2 itself; therefore, it becomes possible to write a system of 2 or more equations and to invert it to compute G and R. The calibration now is reduced to the determination of the received noise power from the different targets. This can be achieved by means of models and/or with the support of other spaceborne well-calibrated radiometers flying at the same time as the altimeter. It is important to point out that, when observing the environmental noise, P_{tlm} fluctuates according to a well know statistic that depends on the integration that is performed by the receiver. The standard deviation of these fluctuations depends on the receiver bandwidth and the integration time. Bigger fluctuation will determine less accurate estimation of the unknowns. Since the bandwidth of the altimeter receiver is very small when compared to radiometers, it will be necessary to consider many different data points to estimate the unknowns by using a best fitting technique instead of just inverting a system of equations. This is one of the drawback of the method, whose success depends on the number of acquisition in noise-listening mode becomes available during the calibration exercise.

Last item to be considered for pulse-limited altimeters is the antenna pattern. In fact, in active mode the altimeter collects radiation only from the very central part of the antenna beam, while in passive mode it involves the entire antenna pattern. This translates into a correction factor, possible to be computed using the antenna pattern measured on ground.

2. 0 General requirements for Passive Calibration

2.1 Project overview

The project has been divided into two subsequent phases:

1. *Phase 1*. Its main objective was to set up the procedures to simulate the brightness temperature at the RA-2 frequency bands coming from different scenarios and to test it for a set of *calibration training areas* all over the globe. These cases correspond to those where data were available from current spaceborne microwave radiometers (SSM/I and TMI) and/or from ERS-1 Radar Altimeter (RA) which was operated in a noise-listening mode for about three orbits in 1998 and 1999.

2. *Phase 2*. This phase was focused on the actual calibration of RA-2 on board of ENVISAT, using data acquired during the 6-month commissioning phase. The calibration is performed within the so-called *calibration test areas*, identified during the Phase 1 within the calibration training areas. The simulations of brightness temperature have been validated against co-located spaceborne microwave radiometers (SSM/I, TMI) collected for each Envisat overpass of the test areas. Some acquisitions from MWR have been also considered.

A better insight of the main features of the mentioned two phases is given below, while candidate models and data flow are described in the next section 2.2.

2.1.1 Phase-1 activity

During Phase 1, it has been understood how to quantify by models the brightness temperature apparent at the RA-2 antenna (hereinafter called also apparent antenna temperature T_A) during passive calibration acquisitions.

Due to the complexity of radiometric response models, the implementation of the methodology has been split into three Work Packages regarding the atmosphere, the sea surface and the Earth land surface (i.e., WP1-3, WP1-4, WP1-5, respectively). Interactions among these work-packages, aimed at coupling the atmospheric models with the surface ones, have been managed.

Once the methodology had been set up during Phase 1, detailed requirements concerning the acquisition of RA-2 data in noise-listening mode have been defined. These requirements consisted in the specification of the *calibration training areas* (over ocean, land, desert and continental ice) where a verification of the model error has been accurately performed in terms of T_A at RA-2 operating frequencies. The amount of RA-2 data to be requested during the ENVISAT Commissioning phase was estimated.

Modeling the Earth emission for spaceborne radiometry applications and for environmental noise analyses is a challenging objective where research activities are progressing, but many improvements are still necessary (Mätzler, 1997). The critical issue of Phase 1 was represented by the degree of accuracy and completeness of the adopted radiometric models to be confronted to the input data requested by the same models. In other words, it would be almost useless to consider a very accurate and complete radiometric model if it is not feasible to gather the required input data at a time-space resolution compatible with RA-2 observations. The adopted radiometric models should be able, for example, to tackle with spatial inhomogeneity of target areas whose characteristics may vary significantly within the RA-2 antenna footprint. This model ability should be carefully evaluated in terms of the amount of necessary input parameters, their actual availability and expected accuracy. To this aim sensitivity analyses of the adopted radiometric models to the input data has helped to define an optimal compromise between theoretical and operational needs.

With previous considerations in mind, for our purposes we have identified three basic categories of radiometric models:

Numerical-physical models: they are more complete and accurate since they start from a detailed electromagnetic description of the medium under observation (i.e., Earth atmosphere over land or sea described in terms of a set of environmental parameters). They numerically solve the Maxwell Equations and/or the Radiative Transfer Equation to determine the surface emissivity (or reflectivity) and the spaceborne apparent antenna temperature T_A. Their advantages are represented by their high accuracy and flexibility in terms of input parameters and satellite observation modes. Their drawbacks are related to both physical model underlying assumptions and cumbersome implementation and efficiency, as well as input data availability

Semi-empirical models: they make use of experimental data to tune a few parameters of a *model function* which relates input environmental parameters to spaceborne T_A. The model function can be suggested by theoretical considerations or by purely empirical approaches (e.g., regression analysis). Their advantages are represented by their simplicity of use and efficiency within iterative schemes, while their drawbacks are linked to both tuning procedures generally performed for specific instruments and lack of generality of the chosen functional relation.

Frequency-scaling models: they estimate the spaceborne T_A at the considered frequency (i.e., RA-2 frequencies) starting from upwelling brightness temperature measurements available at different frequencies from co-located well-calibrated spaceborne radiometers. The regression model may be tuned by using the outputs of physical or semi-empirical models. Their advantages are represented by the implicit tuning to actual radiometric measurements and high efficiency of use, while their drawbacks are related to the limitations of the adopted training data set and of the regression model.

The final selection of the radiometric model approach has been performed during Phase 1 of the project by considering the error of each model to be included in the overall error budget. The upper bound for the root mean square error (rms) of Earth brightness temperature modeling has been considered 12 K, as demonstrated by the work by Schiavon et al. (1998), and this value has been assumed as a goal for the procedure to be implemented.

2.1.2 Phase-2 activity

The Phase 2 has consisted in the actual processing of the RA-2 data acquired during the ENVISAT Commissioning Phase, together with the collection and processing of all other data needed to run the models within the *calibration test areas*. A general scheme of the overall procedure is shown in the block diagram of Fig. 2.1.

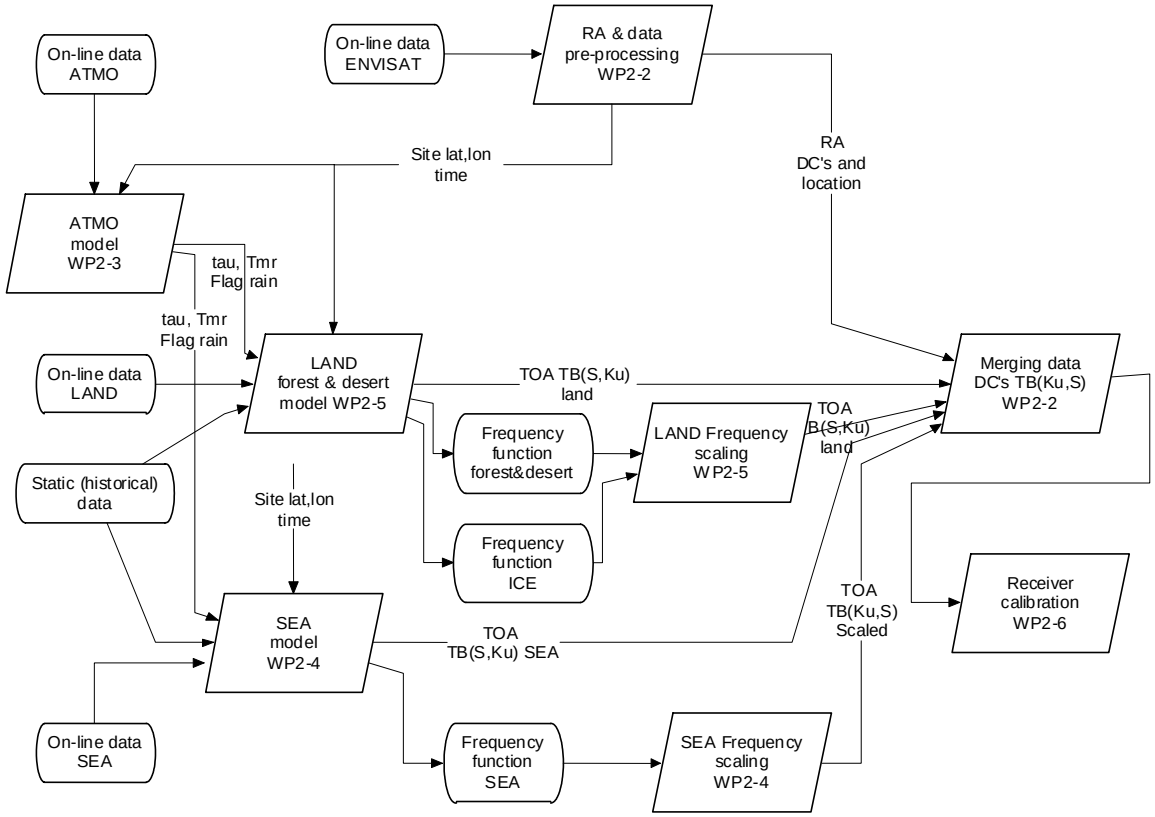

Fig. 2.1: *Block diagram of the procedure implemented during Phase 1 and used during Phase 2. Rhombi indicate functions, arrows indicate data flow, and ovals represent databases both to be accessed and to be generated. TB, tau and Tmr indicate brightness temperature, atmospheric opacity and mean radiative temperature, respectively. TOA stands for Top Of the Atmosphere. Note that the Work Packages in which each function will be performed during Phase 2 are also reported.*

In the previous figure rhombi indicate functions, arrows indicate data flow and ovals represent databases to be both accessed or built during the Phase 2 of the project. The scheme is only conceptual and its aim is only to show the rationale underlying this study.

The scheme identifies a number of homogeneous tasks within the project. In particular, runs of radiometric models simulating the atmosphere, the sea surface and the Earth solid surface has been considered as separated tasks and WP's (WP2-3, WP2-4 and WP2-5 of Phase 2). The collection, organization and pre-processing of all input data and of the outputs of the previous tasks has been considered together in a separated WP (WP2-2 of Phase 2).

Finally, the calibration exercise has produced the estimation of the receiver parameters of the RA-2 for calibrating the surface backscattering coefficient on the bases of the pre-launch characterization of instrument modules performed by ESA or his sub-contractor (WP2-6 of Phase 2).

2.2 Model design and implementation

In previous sections we have pointed out the three basic approaches which have pursued during Phase-1 to evaluate the spaceborne antenna noise temperature of RA-2: numerical-physical models (NPM), semi-empirical models (SEM) and frequency-scaling models (FSM). Here we will illustrate some details about the design of each radiometric model during Phase 1, emphasizing their synergies, input data and data flow.

A general overview of the radiometric models will be also given by considering the Atmosphere, Sea and Land as separate targets. This choice responds to the anticipated work structure, described in the previous section. For each sub-section a short description of available NPM, SEM and FSM will be included.

2.2.1 Model design

Numerical physical models generally require a full set of environmental parameters as input data. This parameters should be available at each RA-2 overpass over the *calibration areas* (both in the training and test phases) with a given spatial resolution. The following figure shows a block diagram of a possible simulation scheme to use NPM basically similar for Atmosphere, Sea and Land procedures.

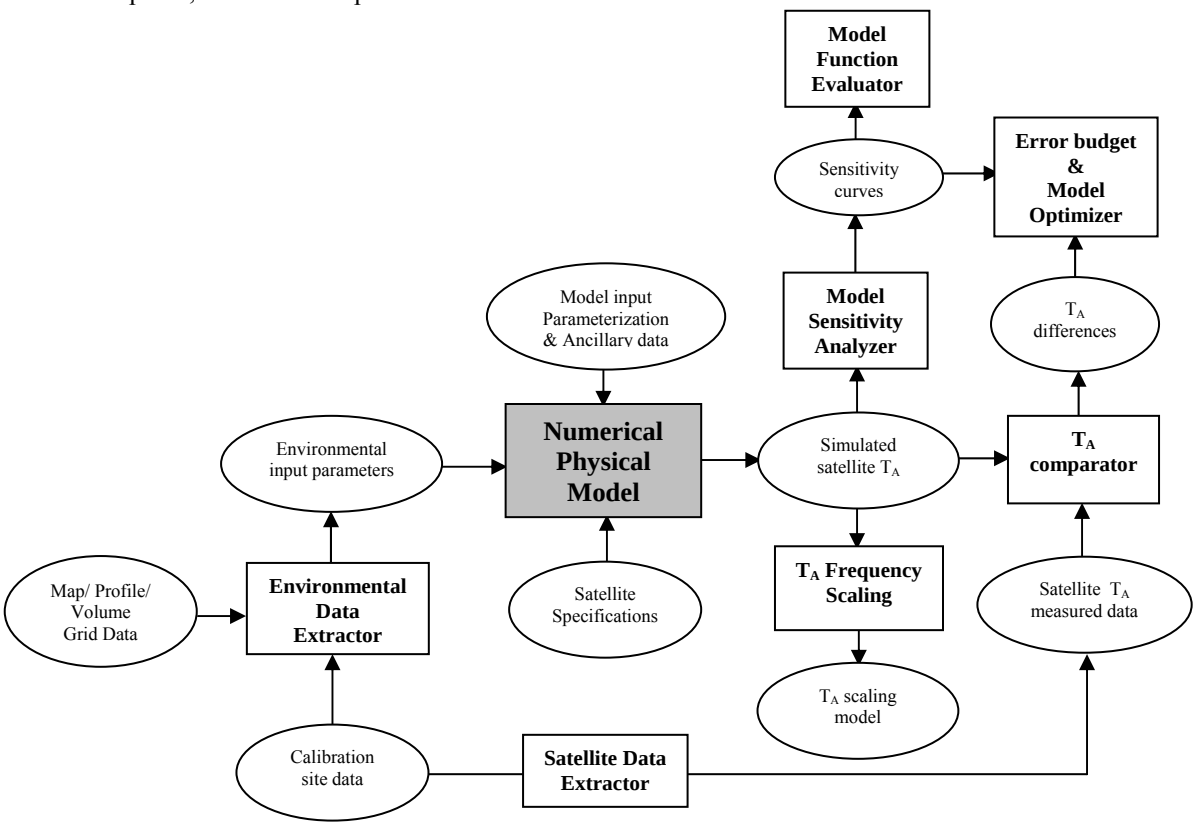

Fig. 2.2.: *Block diagram of the procedures to apply Numerical Physical Models to RA-2 antenna noise temperature calibration. Rectangles indicate operators, arrows indicate data flows, and ovals represent data sets.*

The Environmental Data Extractor accepts maps, profile or volume grid data, coming from various sources:

i) output volumes from general circulation models (GCM) operated by Numerical Weather Prediction (NPW) centres, such as the European Centre for Medium-range Weather Forecast (ECMWF) and the National Centre Environmental Prediction (NCEP);
ii) meteorological data profiles from radiosounding observations (RAOB), which are available at given sites and are characterized by random distribution in space all over the globe; they are available at synoptic hours either 4 or 2 times per day;
iii) maps available from Low Earth Orbit (LEO) satellites and Geosynchonus Earth Orbit (GEO) satellites, with a time and space resolution depending on the given sensor and platform. Useful ancillary products can be cloud coverage, sea surface temperature, surface wind speed vector.

The Environmental Data Extractor selects environmental parameters within the given calibration areas (i.e., latitude/longitude boxes and time intervals) to be injected into NPM's. The latter are selected on the bases of satellite specifications (e.g., view angle, frequency, polarizations), ancillary data (e.g., pre-set parameters) and model input parameterizations.

Within NPM's, the assumption to work in clear-air conditions or, at least, in the absence of precipitation, is needed to avoid complex computations for atmospheric radiative modelling. This assumption has to be supported by data analysis. If satellite data are considered, rain and cloud flags can be derived from spaceborne microwave radiometers with a good accuracy over ocean. Cloud coverage can inferred by METEOSAT data as well. If NWP data are considered, cloud and rain presence is indicated for each grid point so that it could be used to detect unwanted local meteorological conditions. This cloud-screening is, of course, common to all model approaches.

The output of NPM will consist of a set of simulated satellite T_A's which can have a twofold use:

i) to perform a sensitivity analysis of the model to various input parameters with the aim to yield sensitivity curves for model optimization, error budget evaluation and Model Function evaluation;
ii) to compute the coefficients of a regressive frequency/angle scaling algorithm which should be able to estimate T_A's at RA-2 frequencies (i.e., S and Ku bands) and view angle (i.e., nadir) from T_A's at frequencies (i.e., basically 10, 19, 21, 22, 37, and 85 GHz at both polarizations except water vapor channels) and view angles (i.e., about 50° zenith) of currently available satellite microwave radiometers (e.g., SSM/I and TMI).

Over the selected areas, measured microwave satellite T_A data can be extracted by a Satellite Data Extractor. To our purposes we have considered the following:

- Special Sensor Microwave Imager (SSM/I) aboard DMSP platforms with frequencies at 19.3, 22.3, 37.0 and 85.5 GHz and view zenith angle at 53° on a sun-synchronous near-polar orbit;
- TRMM Microwave Imager (TMI) aboard the TRMM platform with frequencies at 10.6, 19.3, 21.2, 37.0 and 85.5 GHz and view zenith angle at 51° on a inter-tropical orbit;

Measured T_A data are used by a T_A Comparator, which can include a data quality module, to perform a discrepancy analysis between simulated and measured T_A data within the *calibration areas*. The output of this module should be used by a Model Optimizer whose goal is to tune the NPM in case a discrepancy higher than a given threshold and to perform an Error Budget Analysis on the basis of these results.

It is apparent from this description the reason why a NPM approach is valuable in itself. Its accomplishment can help developing both semi-empirical models (i.e., ad hoc model functions) and frequency-scaling models (i.e., relationships expressed as function of the electromagnetic frequency based on a best fitting of simulated data).

Semi-empirical models requires a limited set of environmental parameters, often related to surface characteristics and average atmospheric conditions. Conceptually they are similar to NPM, but with respect to the latter they present less flexibility and a reduced potential in the tuning phase.

In some cases model functions can be also designed in cascade steps and can refer to intermediate radiometric quantities. For instance, within the Atmosphere module the atmospheric optical thickness τ_a and mean radiative temperature T_{mr} can be derived not directly from T_A measurements, but from integrated variables (e.g., water vapor and liquid columnar contents) initially obtained from T_A measurements at given frequencies.

This difference is appreciated in Fig. 2.3here, with respect to Fig. 2.2 Frequency Scaling module is absent (unless the model function itself is designed to perform frequency scaling) and only ancillary data are input to the SEM.

Frequency scaling models are much simpler than previous two approaches. We can distinguish between FSM whose scaling function is derived: i) from measured satellite T_A data at different frequencies; ii) from regression curves derived from numerical physical model simulations. Fig. 2. 4shows the FSM block diagram.

2.2.2 Atmosphere models

Among the numerical physical models for clear-air conditions, the Liebe model of atmospheric complex refractivity (Liebe, 1985; Liebe et al., 1993), coupled with the NOAA model for cloud liquid water extinction (e.g., Decker et al., 1978), have been considered to compute antenna noise temperature for calibration purposes. An alternative choice for cloud liquid water extinction is represented by the Salonen model (Salonen et al., 1991). The Liebe model requires as input the vertical profiles of atmospheric temperature, relative humidity and pressure. The model is fairly accurate in clear sky conditions, but final accuracy may be limited by the accuracy of input data. Atmospheric data to be used for running the model could be radiosoundings in specific areas, data from other atmospheric profilers and product supplied by numerical weather prediction centers (e.g., NCEP and ECMWF). Moreover, observations of the atmosphere from

satellite microwave radiometers can be used. In particular, the ENVISAT Microwave Radiometer can be used, but also other spaceborne radiometers such as DMSP-SSM/I and TRMM-TMI are candidate sources of data.

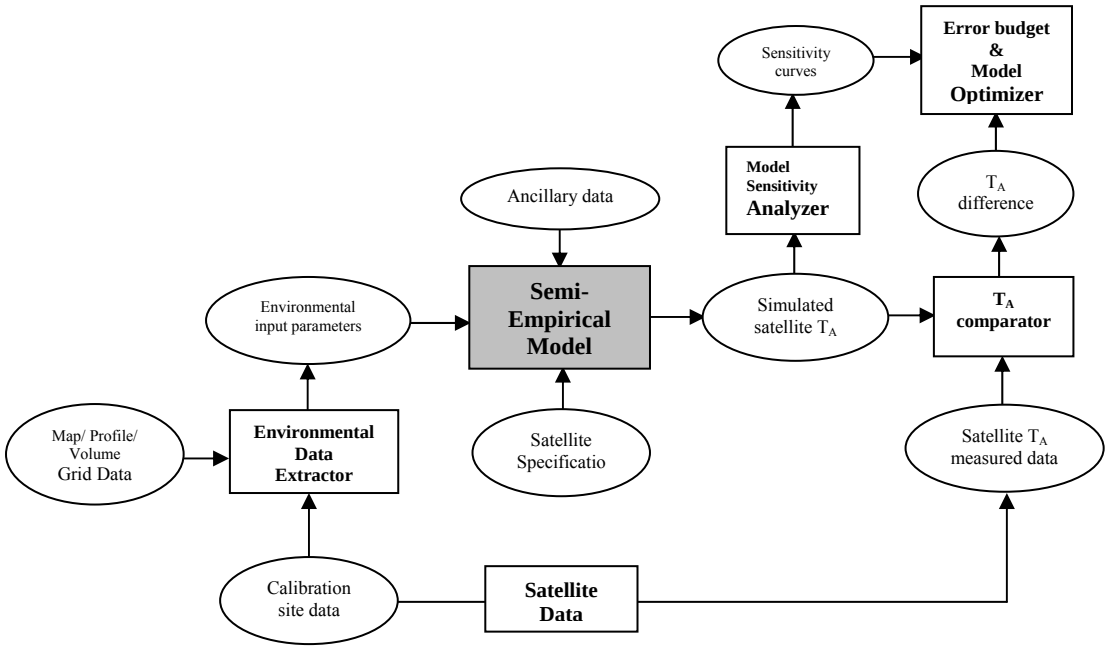

Fig. 2.3.: *Block diagram of the procedures to apply Semi Empirical Models to RA-2 antenna noise temperature calibration.*

Semi-empirical models are illustrated in literature, but not specifically oriented to the instrument frequencies of interest within this study (e.g., Basili et al., 1997; Marzano and Riva, 1999). Ad hoc model functions can be derived from radiative transfer simulations applied to available meteorological profiles on the candidate calibration areas.

Frequency scaling models need to be determined from measured and/or simulated T_A data within this study since no available scaling relations have been published so far to our knowledge.

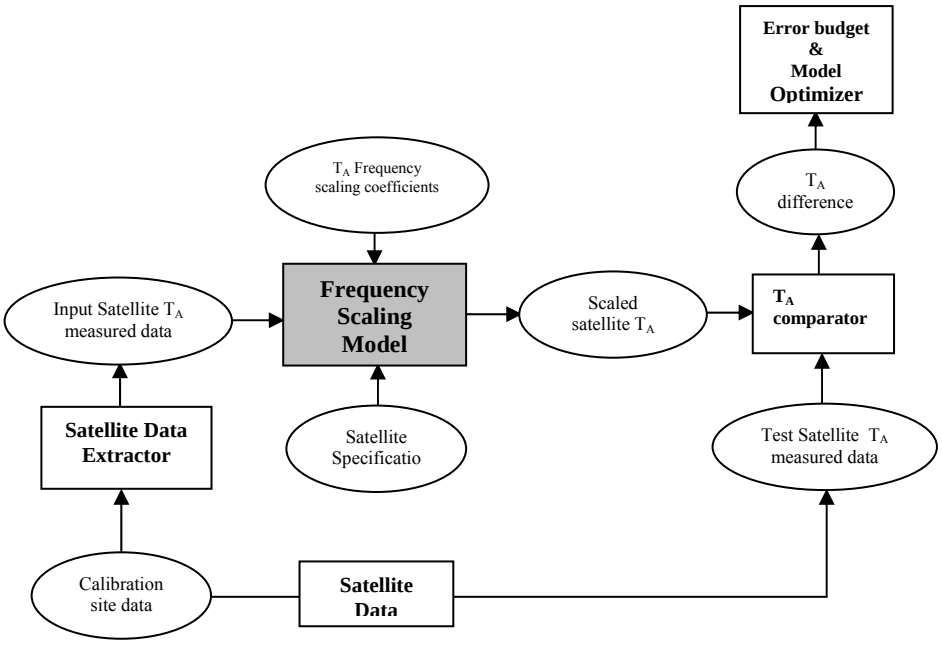

Fig. 2.4: *Block diagram of the procedures to apply Semi Empirical Models to RA-2 antenna noise temperature calibration.*

2.2.3 Sea models

A fairly accurate numerical physical model is the two-scale roughness model for sea polarimetric scattering and emission (e.g., Yueh et al., 1994; Lemaire et al., 1999), including the effect of the foam (e.g., Pandey and Kakar, 1982)

and a model for sea water permittivity (e.g., Klein and Swift, 1977; Ellison et al., 1996). A version of this model, including atmospheric effects as well, has been developed within a previous ESA contract (Pampaloni et al., 1997; Pierdicca et al., 2000). This version accounts for both emission and scattering from an anisotropic surface in a fairly accurate way.

This two-scale model requires as input the surface wind speed and water temperature together with the sea salinity for predicting emission below 5 GHz. Previous analyses have demonstrated its accuracy, even if in case of not fully-developed sea state the model may fail. Input data may be provided by NWP centers (i.e., temperature, wind), spaceborne scatterometers (wind), climatological analysis (i.e., salinity).

Considering the heavy computation load of this model, semi-empirical models have been also taken into consideration (Wentz, 1983; Schluessel and Luthard, 1991; Wentz, 1992). A new semi-empirical model has been also developed in this project based on the available outputs of the NPM model.

Frequency scaling models need to be determined from measured and/or simulated T_A data within this study since no available scaling relations have been published so far to our knowledge.

2.2.4 Land models

Numerical physical models for spatially homogeneous areas, such as large forests and bare soils, are available. They consist in the numerical solution of the polarized radiative transfer equation modeling discrete scatterer media and in closed-formed solutions of the integral equation for the electromagnetic field scattered by rough surfaces (Ferrazzoli et al., 1997). Snow packs and bare soils show larger emissivity variations which depend on several factors so that the usefulness of these physical models must be carefully evaluated, particularly at S band.

Semi-empirical models are also described in the literature. These algorithms essentially modify the Fresnel reflectivity of a flat surface by considering a roughness parameter and a polarization mixing factor. In case of vegetated areas they include radiative parameters of the canopy (i.e., opacity, albedo). They have been developed by using radiometric observations of different types of land cover classes (e.g., Wang and Choudhury, 1981; Bauer and Grody, 1993; Prigent et al., 1998).

Small-scale land cover maps (e.g., forest maps, DEM, etc.) as well as other parameter produced by the weather prediction centers (including surface skin temperature) have been considered to feed the models. However, the lack of reliable inputs for other parameters (such as surface roughness o snow parameters) has suggested us different levels of details to be inserted in the models depending on the observed target. Moreover, it has been preferred to consider small calibration sites in order to make feasible an empirical tuning of the relevant parameters within an homogeneous areas.

As far as ice surface is considered, the driving variables are various and very often unknown, especially for sea ice. Physical models for continental ice can be considered more reliable. The ice location, age, temperature profile and the type of snow cover (dry snow or wet snow) are the most important input data required. Candidate models can be found in literature (e.g., Winebrenner et al., 1992; Fuhrhop et al., 1997), but their usefulness has not fully demonstrated so that calibration areas over ice have been considered less reliable for the purpose of RA-2 calibration.

2.2.5 Candidate input data

Numerical physical models, as well as semi-empirical models, requires a description of the environmental scenario in terms of input parameters, as previously mentioned. To this aim we can enumerate the following sources:

- Numerical weather prediction/analysis data
- Radiosounding observations
- Standard satellite products
- High-level products from satellites (i.e., geophysical parameters)

Concerning radiometric data, during Phase 1 we have selected the following set of microwave radiometers currently available:

- SSM/I aboard DMSP
- TMI aboard TRMM
- Microwave Radiometer (MWR) aboard ERS-1

A brief description of the previous data sources is illustrated in the following.

Numerical weather prediction data

A candidate source of physically-consistent volume grid, describing main atmospheric, sea and land parameters is represented by the outputs of Numerical Weather Prediction (NPW) centers, such as the ECMWF and NCEP.

Spatial and temporal resolution of NWP data should be compared with corresponding characteristics of satellite data. Microwave sensor products can have ground pixels of the order of tens of kilometers (e.g., SSM/I pixel at 19 GHz and 85 GHz is about 60 km and 15 km, respectively; TMI pixel at 10 GHz and 85 GHz is about 60 km and 5 km, respectively), while infrared radiometers can go down to 1 km (e.g., AVHRR at thermal infrared channels). Temporal resolution for a given site is of the order of 12 h. for scanning radiometers with a 1000-km swath aboard LEO platforms.

Major characteristics of NWP output data are:

i) coarse spatial resolution (i.e., tens of kilometers) going from about 40 km for ECMWF data to more than 100 km for NCEP ones;
ii) reduced temporal resolution which goes from 3 hours for NWP forecasts data to 6 hours for NWP analyses.

The analyses are available every 6 hours starting from 0 GMT; alternatively, it is possible to collect from NPW forecasted volume grid with a time resolution of 3 hours. The parameters available from analysis and forecasts are comparable from our point of view. Considered the spatial and temporal characteristics of the mentioned sources, the ECMWF data have been finally adopted and we have preferred forecasts only when analysis were not close in time to the RA-2 acquisitions. In few cases, collection of data before and after the RA-2 passage has become necessary to allow one to interpolate parameters at the Envisat acquisition time. Notice that profile data consist of 16 predefined altitude levels given on a regular lat/lon horizontal grid. In order to account for surface topography and the changing depth of the atmosphere, an interpolation of the atmospheric parameters at the altitude of the Earth surface has been done.

Due to their intrinsic relevance to the project, we will describe the main parameters available from NWP. Generally speaking, NCEP represents a sub-set of ECMWF data. For each grid point, NWP data of interest for radiometric modeling consist of the following fields, ordered with respect to Atmosphere, Land and Sea modules. In the last column we list the NCEP equivalent field if available (otherwise, the field is left blank). Not all variables are, indeed, necessary as model inputs. The actual use of these parameters in the model is discussed in the relevant sections.

ECMWF Field description	*Name*	*Code*	*Units*	*NCEP Equivalent Field*
Land				
Lake cover	CL	026	0-1	
Surface roughness	SR	173	m	
Standard deviation of orography	SDOR	160	adim	
Anisotropy of sub-gridscale orography	ISOR	161	adim	
Slope of sub-gridscale	SLOR	163	adim	
Variance of sub-gridscale orography	VSO	200	m^2	
Soil type	SLT	043	#	
Soil temperature level 1	STL1	139	K	TMPSoilT
Soil wetness level 1	SWL1	140	m	
Volumetric soil water layer 1	SWVL1	039	$m^3\ m^{-3}$	SOILWSoilT
Vegetation fraction	VEG	199	0-1	
Low vegetation cover	CVL	027	0-1	
High vegetation cover	CVH	028	0-1	
Type of low vegetation	TVL	029	#	
Type of high vegetation	THV	030	#	
Snow melt	SMLT	045	m	
Snow depth	SD	141	m	WEASDsfc (in kg m^{-2})
Temperature of snow layer	TSN	238	K	
Ice surface temp. layer 1	ISTL1	035	K	
Ice age	ICE	250	1,0	
Sea				
Sea surface temperature	SSTK	034	K	
Skin temperature	SKT	235	K	
Surface pressure	SP	134	Pa	
Boundary layer height	BLH	159	m	HPBLsfc
U wind component at 10 m	10U	165	m s^{-1}	UGRD10m
V wind component at 10 m	10V	166	m s^{-1}	VGRD10m
10-m wind speed	10SI	207	m s^{-1}	
Temperature at 2 m	2T	167	K	TMP2m
Dew-point temperature at 2 m	2D	168	K	RH2m (in %)

Atmosphere

Land/sea mask	LSM	172	0,1	LANDsfc
Pressure profile	PRES	054	Pa	
Temperature profile	T	130	K	TMPisbl
Relative humidity profile	R	157	%	RHisbl
Specific humidity profile	Q	133	kg kg^{-1}	
U velocity profile	U	131	m s^{-1}	UGRDisbl
V velocity profile	V	132	m s^{-1}	VGRDisbl
Vertical velocity profile	W	135	Pa s^{-1}	VVELisbl
Total column water (ice+liq.+vap.)	TCW	136	kg m^{-2}	CWATeatm
Total column water vapor	TCWV	137	kg m^{-2}	PWATeatm
Total cloud cover	TCC	164	0-1	
Cloud cover	CC	248	0-1	TCDCccy (in %)
Convective cloud cover	CCC	185	0-1	
Low cloud cover	LCC	186	0-1	
Medium cloud cover	MCC	187	0-1	
High cloud cover	HCC	188	0-1	
Cloud liquid water content profile	CLWC	246	kg kg^{-1}	CLWMRisbl
Cloud ice water content profile	CIWC	247	kg kg^{-1}	
Stratiform precipitation accum.	LSP	142	m	
Convective precipitation accum.	CP	143	m	
Total precipitation accum.	TP	228	m	

Access to the ECMWF site is restricted to registered users only. Registration is conditioned to permission from the National Agency of Weather Forecast.

Radiosounding observations

The distribution of radiosounding observation (RAOB) stations is fairly not uniform and they do not provide routinely measurements over ocean for obvious reasons. The location of RAOB sites close to our calibration sites are reported in Fig. 2.5.

Vertical profiles, acquired by radiosondes, are generally available every 6 hours starting from 0 GMT. Profiles of the following quantities are usually provided:

- Altitude (m) above sea level;
- Pressure (hPa);
- Temperature (K);
- Relative humidity (%) or dew-point temperature (K);
- Wind speed (m s-1);
- Angle of wind vector with respect to the North

As an example, RAOB data, gathered all over the globe and available for research purposes, are archived at: http://www.noaa.gov

Standard satellite products

As already mentioned, product data from the following satellite platforms could be used as inputs to the models:

- Cloud coverage from VISSR aboard METEOSAT-7 and MODIS aboard TERRA;
- sea surface temperature from AVHRR aboard NOAA platforms;
- surface wind speed vector from SeaWind aboard QuickScatt;
- vegetation index from TM aboard LANDSAT or AVHRR aboard NOAA platforms.

The use of satellite data is hampered by the difficulty to locate them in time and space in correspondence to RA-2 overpasses. Moreover, the Earth picture in term of environmental parameters is rarely complete due to different temporal repetitivities.

Satellite radiometric data

As already mentioned, product data from the following microwave radiometers could be used as inputs to the models or for validating the simulations against well calibrated instruments:

- Special Sensor Microwave Imager (SSM/I) aboard DMSP platforms with frequencies at 19.3, 22.3, 37.0 and 85.5 GHz with dual linear vertical (V) and horizontal (H) polarization (except at 22 GHz where only V channel is available) and view zenith angle of 53° on a sun-synchronous near-polar orbit; field-of-views (FOV's) are about 60, 30, 15 km at 19, 37 and 85 GHz, respectively, with a time repetition of about 12 hours due its large swath (about 1400 km).
  Data have been requested through: http://www.saa.noaa.gov

- TRMM Microwave Imager (TMI) aboard TRMM platform with frequencies at 10.6, 19.3, 21.2, 37.0 and 85.5 GHz with dual linear vertical (V) and horizontal (H) polarization (except at 21 GHz where only V channel is available) and view zenith angle at 51° on a inter-tropical orbit; field-of-views are about 60, 30, 15, and 5 km at 10, 19, 37 and 85 GHz, respectively, with a time repetition of about 8 hours and a swath of about 800 km. Due to orbital configuration, data are limited to latitudes in the range –35/+35 degrees.
  Data have been requested through: http://trmm.gsfc.nasa.gov

- Microwave Radiometer (MWR) aboard ERS-2 and ENVISAT with 2 frequencies at 23.5 and 36.5 GHz with ground resolution of about 22 km.
  The MWR is nadir pointing so that its time repetition is extremely low. Indeed, it is the only instrument really co-located with respect to the RA-2 radar altimeter aboard ENVISAT, even though at different frequencies. Note that the orbit of ERS-2 have been made coincident with that of ENVISAT for inter-calibration requirements. Therefore, the two satellites have overpassed the same sites with half an hour time delay.
  Only a small amount of these data have been made available for the purpose of this project.

2.3 Calibration areas

As previously mentioned, we distinguish between *training calibration areas* used during Phase 1 from the *test calibration areas*, where RA-2 data in noise listen mode have been acquired. Indeed, the latter are introduced to ensure a larger degree of model verification during Phase 1 using historical data archives.

The selection of calibration and training areas has been driven by some specific criteria:

i) to select various Earth scenarios for various seasonal periods in order to get a large dynamics range of the spaceborne radiometric response for a better model calibration and, within Phase-2 of the project, for a better assessment of the RA-2 receiver response;
ii) to optimize the number of co-located platform passes over the areas by looking at the archived satellite data to be used during Phase 1 and also at the orbital characteristics of candidate spacecrafts during Phase 2;
iii) to maximize the number of radiosounding stations present within the chosen area in order to have a better characterization of atmospheric state, at least during Phase 1 when ENVISAT orbit tracking is not a constraint;
iv) to select satellite overpasses closer to synoptic hours (i.e., 0, 6, 12 and 18 GMT) so that to have a NWP analysis grid data set to be used for model input parameterization;
v) to have a sufficiently large spatial area in order to increase the probability to have as many as possible RA-2 passes over the area itself during Phase 2.

Note that criterion ii) for DMSP and TRMM platforms is difficult to be verified since TRMM covers only the equatorial and tropical areas, whilst DMSP's are quasi-polar platforms with fairly stable equatorial crossing. Considering these orbital configurations and the equatorial crossing of DMSP not close to that of ENVISAT, overlaps between ENVISAT and TRMM swaths are possible only between 35° S and 35° N latitudes, whilst good collocation of ENVISAT and DMSP data are possible only at high latitudes.

The result of this selection procedure is shown in the list below where the spatial box of *test calibration areas* is specified by the left upper and right bottom edge, expressed in degrees and by a geographic name. The rectangular boxes are evidenced in Fig. 2.5. Star symbols represent RAOB stations, while dash line stands for ERS-1 nadir orbit on Apr. 27, 1999 when RA was operated in listening mode. Red crosses over the ERS-1 orbit indicate the presence of collocated SSM/I data during that experiment.

Sahara desert :	31°30'00" N	6°30'00" W	left-upper edge
	16°30'00" N	29°30'00" E	right-bottom edge
Amazon forest:		3°30'00" N	74°30'00" W left-upper edge
	11°30'00" S	52°30'00" W	right-bottom edge
North Atlantic:	31°30'00" N	60°30'00" W	left-upper edge
	17°30'00" N	24°30'00" W	right-bottom edge

South Atlantic :	27°30'00" S	41°30'00" W	left-upper edge
(Gough Island)	38°30'00" S	11°30'00" W	right-bottom edge
Indian ocean:	2°30'00" S	60°30'00" E	left-upper edge
(Cocos Island)	17°30'00" S	95°30'00" E	right-bottom edge
Pacific Ocean:	21°30'00" N	158°30'00" W	left-upper edge
(Hawaii Island)	10°30'00" N	122°30'00" W	right-bottom edge
Greenland:	81°30'00" N	50°30'00" W	left-upper edge
	70°30'00" N	28°30'00" W	right-bottom edge
Antarctica:	73°30'00" S	18°30'00" E	left-upper edge
	84°30'00" S	72°30'00" E	right-bottom edge

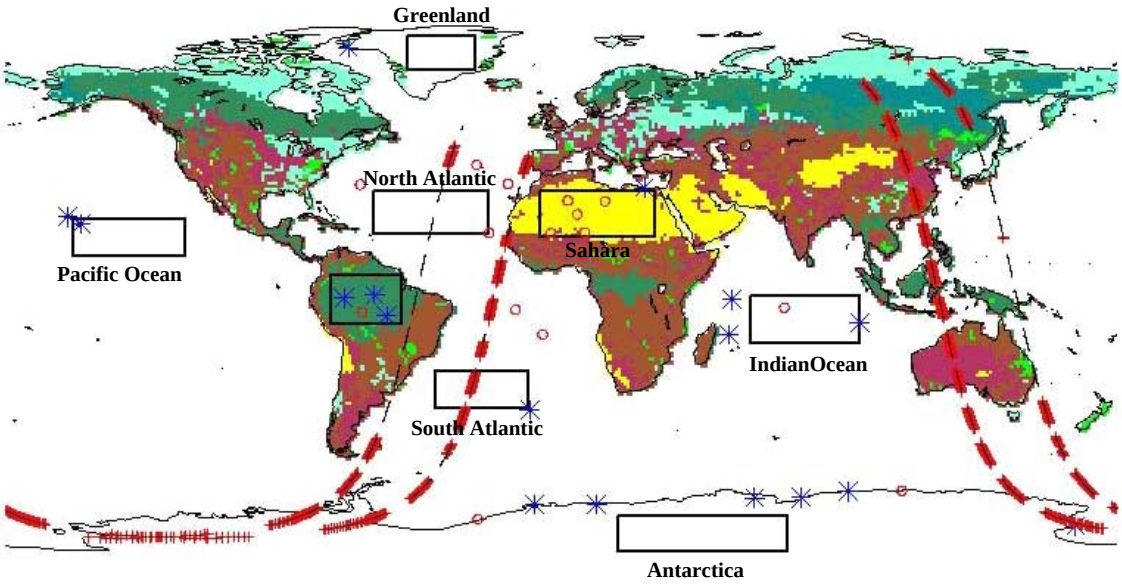

Fig. 2.5.: *Calibration test area for ENVISAT RA-2. Star symbols represent RAOB stations, while dash line stands for ERS-1 nadir orbit on Apr. 27, 1999 when RA was operated in its listening mode. Red crosses over the ERS-1 orbit indicate the presence of collocated SSM/I data.*

Superimposed and almost coincident data from SSM/I and TMI have been searched from the corresponding archive for the purpose of Phase-1 activity. A number of acquisitions have been selected for each site spanning different seasons and time of the day in order to collect ECMWF data and perform model evaluation. This is reported in APPENDIX A.1.

Note that during Phase 1 study, for seek of homogeneity, ECMWF data have been selected and simulations have been performed within the following *training calibration areas* graphically shown in Fig. 2.6. Coordinates are listed below.

ECMWF data boxes (dimensions: 10° x 10° or 10° x 20° or 20° x 20°)

Sahara desert :	27° N ,	4° E
	17 N ,	16°E
Amazon forest:	0° S ,	72 W
	10° S ,	52 W
Indian ocean:	7° S ,	87° E
(Cocos Island)	17° S ,	97° E
Pacific Ocean:	22° N ,	158° W
(Hawaii)	12° N ,	148° W
Antarctic:	68° S ,	56° E
	78° S ,	66° E
North Atlantic:	36° N ,	43° W
	16° N ,	23° W
South Atlantic :	18° S ,	31° W
(Gough Island)	38° S ,	11° W

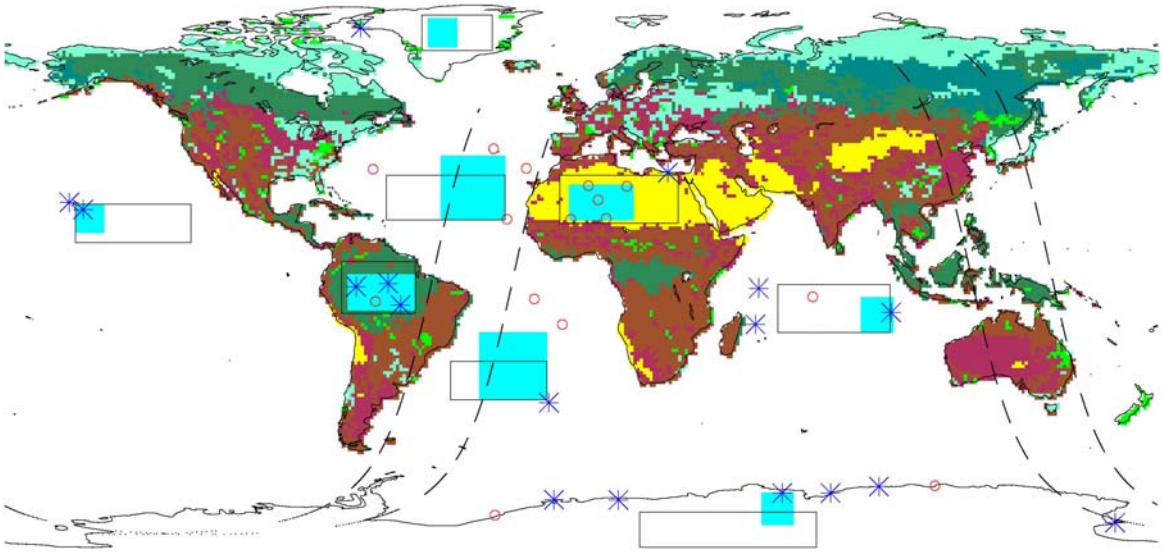

Fig. 2.6. *Calibration training areas, indicated by cyan rectangular boxes, where ECMWF data analysis were collected. Star symbols represent RAOB stations, while dash line stands for ERS-1 nadir orbit on Apr. 27, 1999 when RA was operated in its listening mode.*

3.0 Atmospheric Models

3.1 Introduction

The procedure described in this section is devoted to the analysis and modelling of the atmospheric contribution to the observations of RA-2, when operating in noise listening mode [Greco et al., 2002]. The main purpose of this procedure (named ATMO procedure) is to evaluate atmospheric propagation and radiative parameters, such as opacity τ and mean radiative temperature upwelling and downwelling (T_{mr_up} and T_{mr_dn}) [Ulaby, 1981, Wu, 1979] at the RA-2 frequencies of 3.2 and 13.575 GHz, and to produce a flag of possible presence of rain, over selected areas (portion of ENVISAT track, selected as test sites) and at specific times.

According to the framework of the project, also the ATMO procedure is organised in two phases.

Phase 1.

- The first objective of this phase is the determination of the range of expected values for the atmospheric opacity and upwelling and downwelling mean radiative temperature at the two RA-2 frequencies. The effect of uncertainties on the input data is also analysed.
- An inventory of possible sources of required input data to the algorithms for the computation of the mentioned atmospheric electromagnetic parameters is considered, with reference to the selected areas and times.
- The discussion on the algorithms is then presented, with separate description of direct models using conventional input data and ad hoc approaches based on remotely sensed input data.

Phase 2.

- This phase deals with the processing of actual data, acquired during the six-month "commissioning phase", using the algorithms previously developed. Atmospheric opacities, mean radiating temperatures and rain flags are produced, together with the expected relative accuracies, over the selected test sites at ENVISAT passes. The atmospheric electromagnetic parameters, output of the ATMO procedure, are exploited in the LAND and SEA procedures.

3.2 Range of expected values, and sensitivity to frequency and main input data

A simulation of atmospheric optical thickness (attenuation) τ and mean radiative temperature upwelling and downwelling T_{mr} for a non-scattering horizontally-stratified atmosphere has been performed, using as input data radiosounding observations (RAOB's), providing vertical profiles of atmospheric temperature, relative humidity and pressure. The simulated e.m. parameters have been computed at RA-2 frequencies and view angle (nadir), and also at TMI and SSM/I frequencies (10.6, 19.3, 21.2, 22.235, 37, 85.5 GHz) and view angle (51°) by means of a Radiative Transfer Model (RTM), as mentioned in section 3.4.

The simulation has been carried out from a carefully selected collection of RAOB's, from stations distributed worldwide during the years 2000 and 2001, representing therefore different climatic conditions for both maritime and continental regions at any latitudes. The simulated data set of τ and T_{mr} has been divided into three subsets: low latitudes (the area between the 30th parallels), middle latitudes (the areas between the 30th and 60th parallels in both hemispheres) and high latitudes (the areas north and south of the 60th parallels). Exploiting the availability of RAOB input data, also a data set of Integrated Precipitable Water Vapour (IPWV), Integrated Cloud Liquid (ICL) has been generated and complemented with surface values of temperature, pressure and relative humidity.

As results of a first analysis we show in the following figures the range of expected values for τ and T_{mr_up} at the two frequencies of the RA-2, at nadir and at a view angle of 51°, for the three areas.

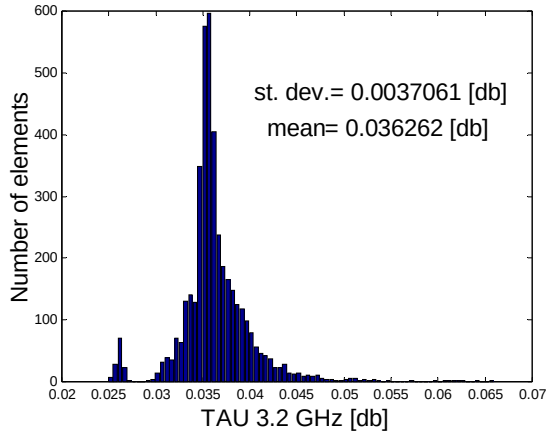

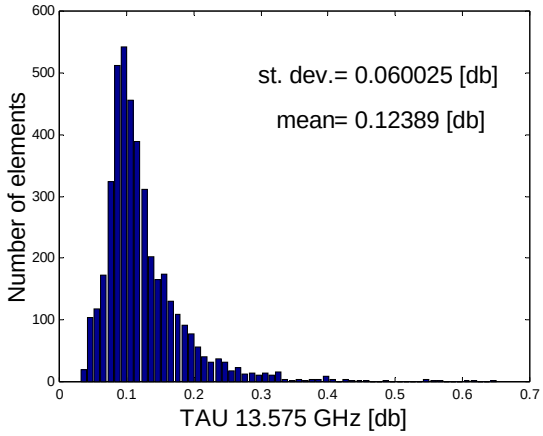

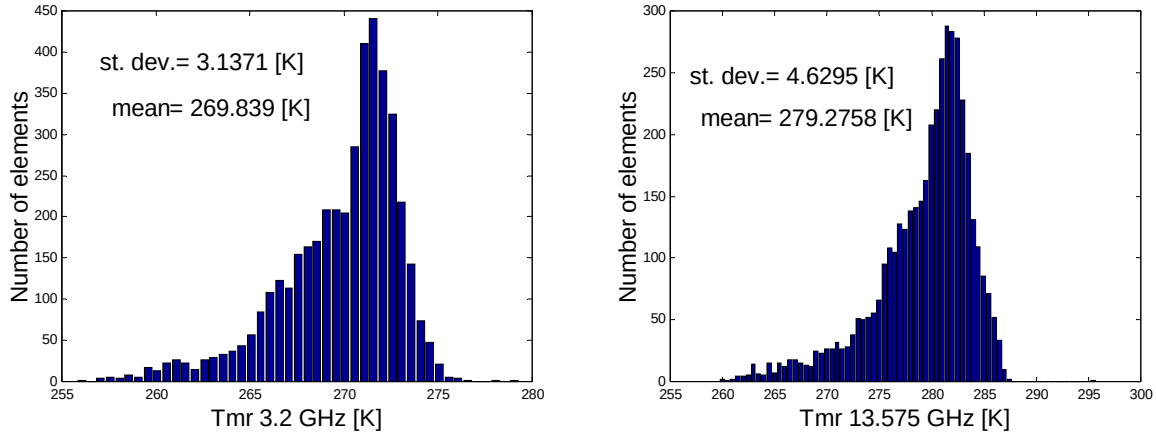

Fig. 3.2.1 Histograms of τ and T_{mr_up} at 3.2 and 13.575 GHz (RA-2 frequencies) and at nadir for low latitudes

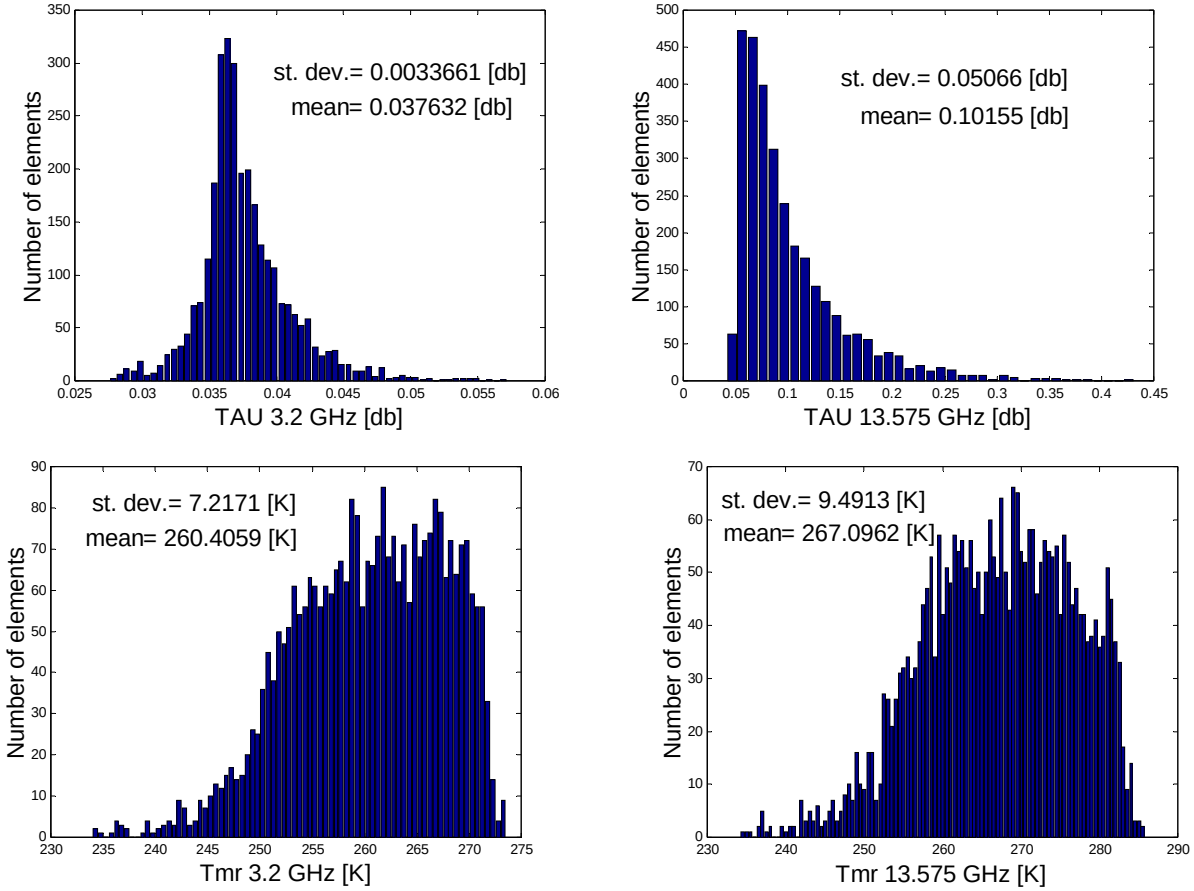

Fig. 3.2.2 Histograms of τ and T_{mr_up} at 3.2 and 13.575 GHz (RA-2 frequencies) and at nadir for middle latitudes

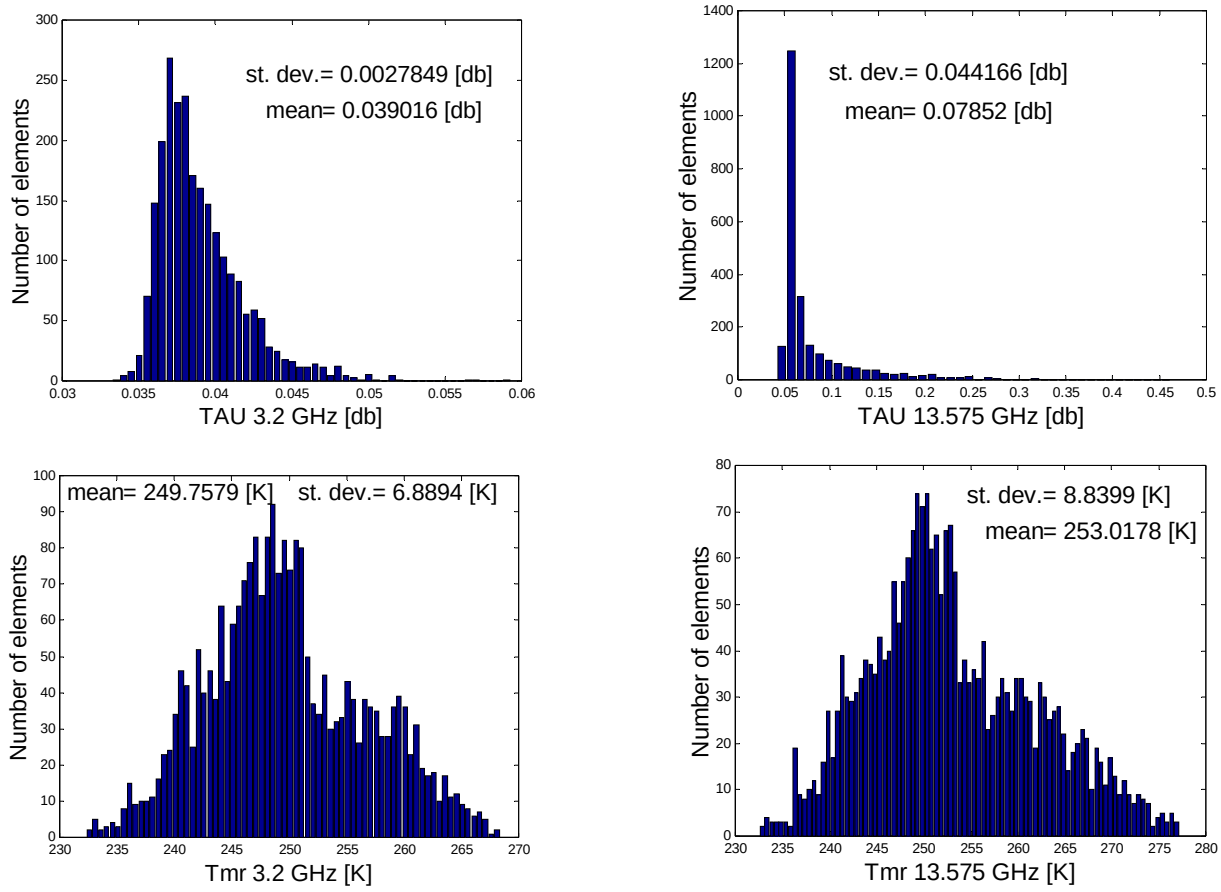

Fig. 3.2.3 Histograms of τ and T_{mr_up} at 3.2 and 13.575 GHz (RA-2 frequencies) and at nadir for high latitudes

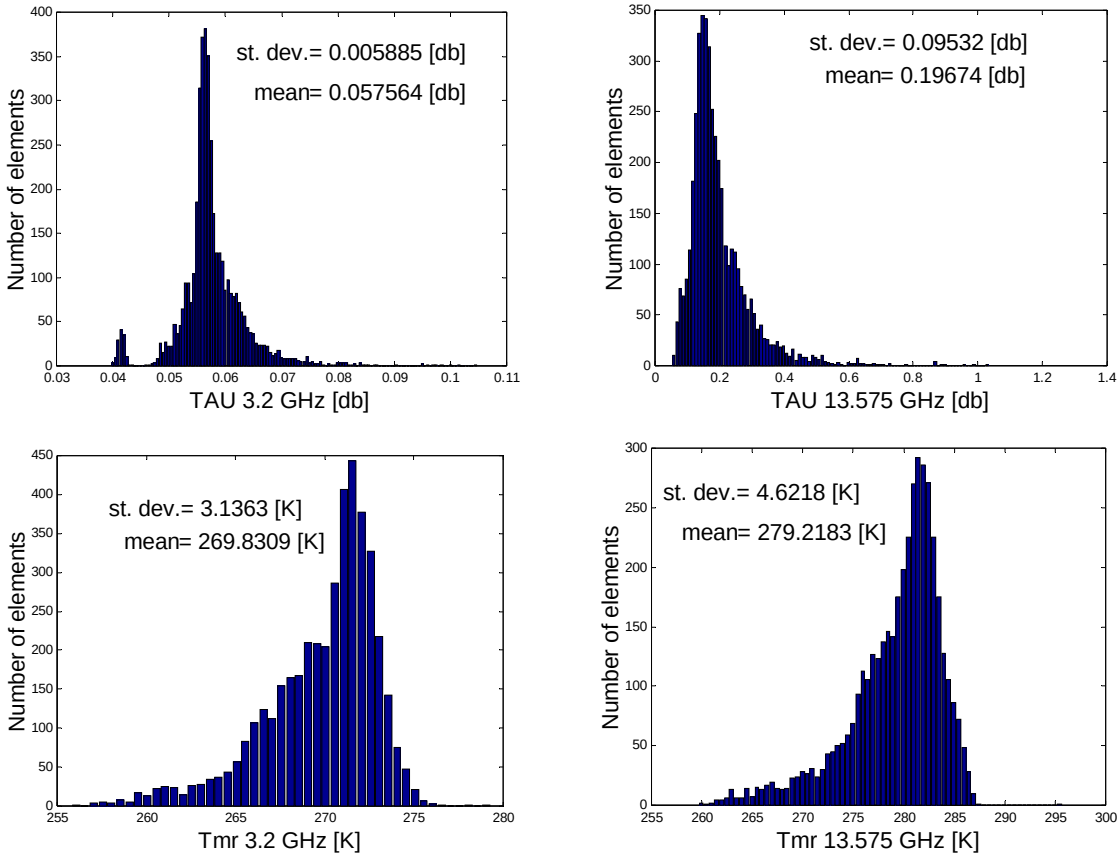

Fig. 3.2.4 Histograms of τ and T_{mr_up} at 3.2 and 13.575 GHz (RA-2 frequencies) and at a view angle of 51°, for low latitudes

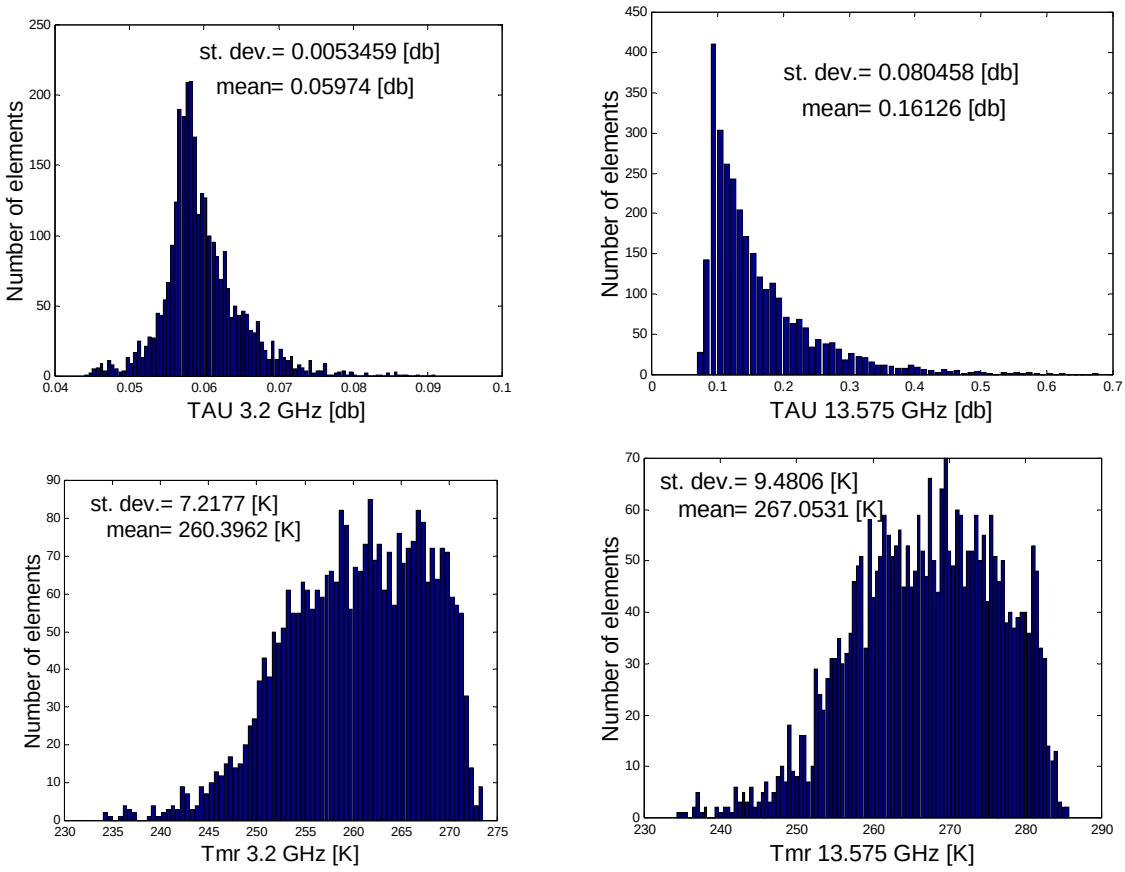

Fig. 3.2.5 Histograms of τ and T_{mr_up} at 3.2 and 13.575 GHz (RA-2 frequencies) and at a view angle of 51°, for middle latitudes

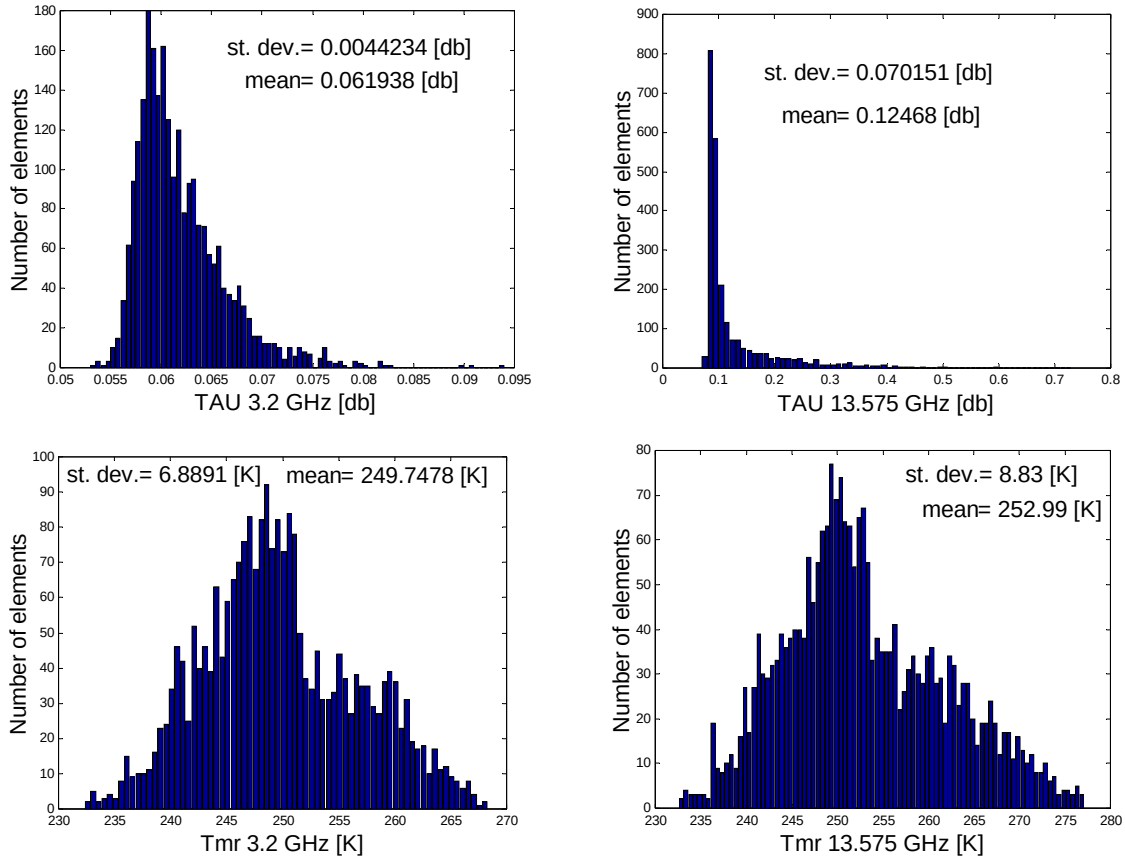

Fig. 3.2.6 Histograms of τ and T_{mr_up} at 3.2 and 13.575 GHz (RA-2 frequencies) and at a view angle of 51°, for high latitudes

The results of a more complete analysis regarding the mean radiative temperature variability for the frequencies of 3.2, 13.6, 10.6, 19.3, 21.2 and 37.0 GHz are reported in the following tables. Mean values and standard deviations of mean radiative temperature at the specified frequencies are reported considering vertical and slant (51°) observations, both for the satellite- (T_{mr_up}) and ground-based (T_{mr_dn}) cases and for the different latitudes.

TABLE 3.2.I MEAN RADIATIVE TEMPERATURE VARIABILITY

Low latitudes: satellite-based

Freq. [GHz]	3.2	13.6	10.6	19.3	21.2	37.0
Mean (nadir)	269.8390	279.2758	276.8968	283.3533	282.6727	279.7604
Std (nadir)	3.1371	4.6295	4.5720	3.9322	3.7589	4.7978
Mean (51°)	269.8309	279.2183	276.8601	283.1656	282.2791	279.4280
Std (51°)	3.1363	4.6218	4.5653	3.9228	3.7710	4.7817

Low latitudes: ground-based

Freq. [GHz]	3.2	13.6	10.6	19.3	21.2	37.0
Mean (zenith)	272.2149	281.1076	278.8379	285.3077	285.3259	282.3984
Std (zenith)	2.9981	4.4312	4.3653	3.8014	3.5828	4.6319
Mean (51°)	272.2683	281.1884	278.9051	285.4922	285.6834	282.7202
Std (51°)	2.9989	4.4347	4.3679	3.8152	3.6118	4.6561

Middle latitudes: satellite-based

Freq. [GHz]	3.2	13.6	10.6	19.3	21.2	37.0
Mean (nadir)	260.4059	267.0962	265.2792	271.0052	270.9092	267.6313
Std (nadir)	7.2171	9.4913	9.0052	9.6597	9.1546	9.6375
Mean (51°)	260.3962	267.0531	265.2499	270.8833	270.6714	267.3752
Std (51°)	7.2177	9.4806	8.9988	9.6194	9.0623	9.5848

Middle latitudes: ground-based

Freq. [GHz]	3.2	13.6	10.6	19.3	21.2	37.0
Mean (zenith)	262.3721	268.7247	266.9825	272.6558	272.9693	269.8791
Std (zenith)	7.3818	9.4925	9.0259	9.7523	9.4314	9.7482
Mean (51°)	262.4193	268.7917	267.0402	272.7835	273.1946	270.1339
Std (51°)	7.3865	9.5023	9.0331	9.7878	9.5148	9.7950

High latitudes: satellite-based

Freq. [GHz]	3.2	13.6	10.6	19.3	21.2	37.0
Mean (nadir)	249.7579	253.0178	252.0800	255.7872	256.2351	253.2998
Std (nadir)	6.8894	8.8399	8.3577	9.5182	9.2159	9.0735
Mean (51°)	249.7478	252.9900	252.0595	255.7230	256.1241	253.1317
Std (51°)	6.8891	8.8300	8.3515	9.4888	9.1555	9.0192

High latitudes: ground-based

Freq. [GHz]	3.2	13.6	10.6	19.3	21.2	37.0
Mean (zenith)	251.3387	254.4584	253.5513	257.2247	257.8555	255.1590
Std (zenith)	7.0411	8.8817	8.4166	9.6041	9.4192	9.2290
Mean (51°)	251.3756	254.5070	253.5946	257.3011	257.9707	255.3339
Std (51°)	7.0463	8.8919	8.4245	9.6300	9.4723	9.2767

An analysis of the sensitivity of atmospheric optical thickness τ and mean radiative temperature to errors affecting the input data was performed considering the effects of random perturbations on RAOB profiles. Starting from a representative profile for each of the three latitude regions, a random generation of one hundred profiles was performed by adding uncorrelated perturbations of zero mean and a standard deviation of 1 hPa, 1.5 K and a 5%, respectively for

each level of pressure, temperature and humidity profiles. The results of the analysis in terms of standard deviations of the computed τ and T_{mr_up} are depicted in the following figures, where mean values are also reported:

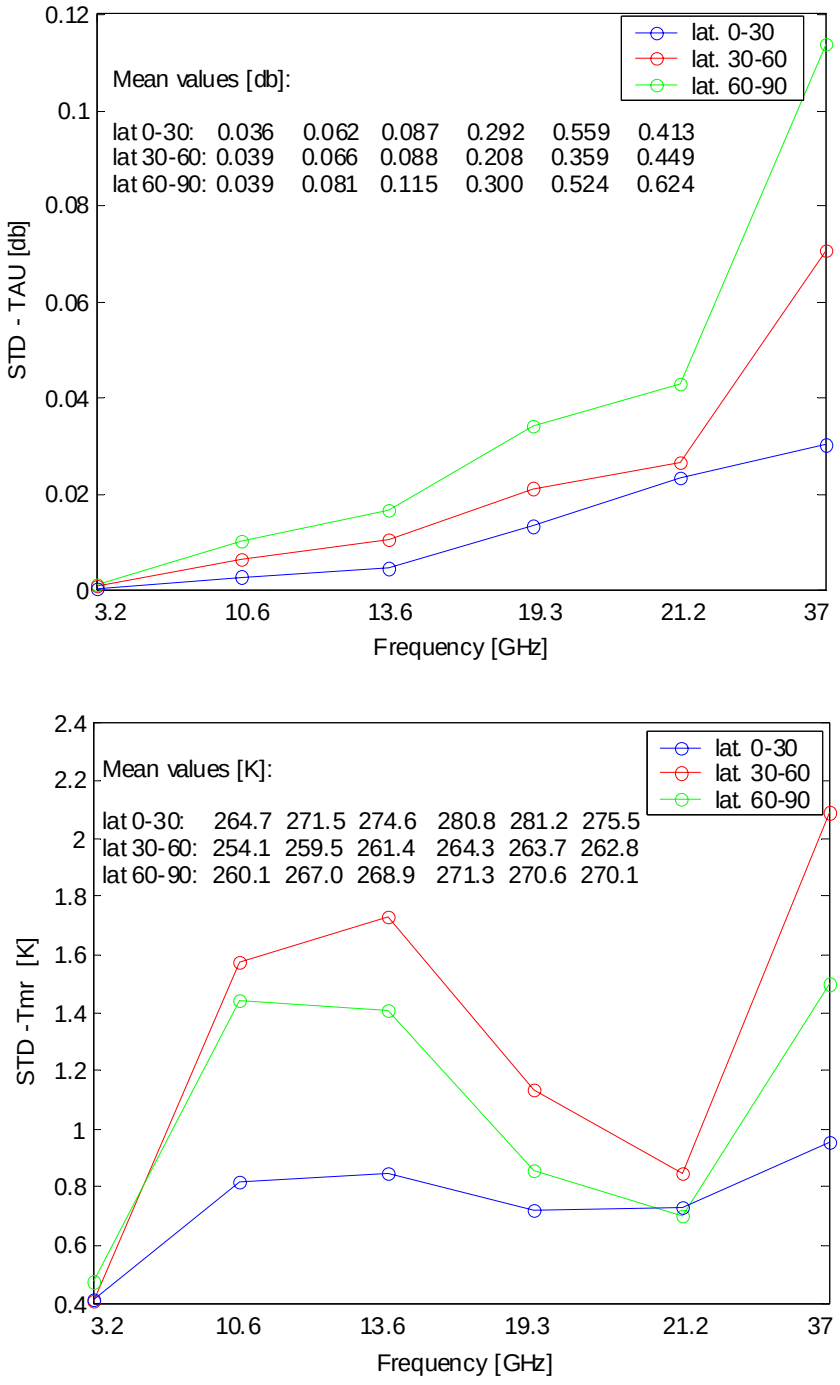

Fig. 3.2.7 Sensitivity of τ and T_{mr_up} to errors affecting the input data (RAOB profiles) at 3.2, 10.6, 13.6, 19.3, 21.2 and 37.0 GHz and at nadir

Also, an evaluation of the climatological sensitivity of T_{BTOA} (i.e. brightness temperatures at the top of the atmosphere) was performed. For this sensitivity analysis, the derivatives of T_{BTOA} versus τ and T_{mr} have been considered, starting from the following simplified relationship:

$$T_{BTOA} = e_s\, T_s\, e^{-\tau} + T_{mr\_up}(1-e^{-\tau}) + T_{mr\_dn}(1-e^{-\tau})(1-e_s)e^{-\tau} \qquad (3.2.1)$$

where T_s is the surface temperature and e_s is the surface emissivity; the evaluation of T_{BTOA} sensitivity with respect to τ and T_{mr} yields:

$$\frac{dT_{BTOA}}{d\tau} = -e_s T_s\, e^{-\tau} + T_{mr\_up} e^{-\tau} + T_{mr\_dn} e^{-\tau}(-1 + e_s + 2e^{-\tau} - 2e_s\, e^{-\tau}) \quad (3.2.2)$$

$$\frac{dT_{BTOA}}{dT_{mr}} = (1 - e^{-\tau}) + (1 - e^{-\tau})(1 - e_s)e^{-\tau} \quad (3.2.3)$$

where the dT_{BTOA}/ dT_{mr} was computed considering T_{mr_up} and T_{mr_dn} as a single variable, since the difference between them is nearly constant, as reported in table 3.2.I.
For the T_{BTOA} climatological variability characterisation the following formula has been applied:

$$\Delta T_{BTOA}{}^2 = \left(\frac{dT_{BTOA}}{d\tau}\right)^2\Bigg|_{\overline{T_{mr}}\,\overline{\tau}} \cdot \sigma_\tau^2 + \left(\frac{dT_{BTOA}}{dT_{mr}}\right)^2\Bigg|_{\overline{T_{mr}}\,\overline{\tau}} \cdot \sigma_{T_{mr}}^2 \quad (3.2.4)$$

where the derivatives, function of τ and T_{mr} (and function also of emissivity and temperature at the surface), are calculated assigning to τ e T_{mr} their mean values, for the different latitudes and at RA-2 frequencies.
Considering the little variation of the derivatives with T_s, we have used a mean value of 283.13 K for T_s. A summary of T_{BTOA} climatological variability is reported in the following table, for two typical (sea and land) emissivity values, at the RA-2 frequencies and for the three latitude zones.

TABLE 3.2.II T_{BTOA} CLIMATOLOGICAL VARIABILITY

3.2 GHz

	SEA	LAND
	ΔT_{BTOA} [K] SEA (emissivity e_s =0.4)	ΔT_{BTOA} [K] LAND (emissivity e_s =0.9)
Low latitude	1.1158	0.1890
Middle latitude	1.0386	0.3078
High latitude	0.8475	0.2930

13.575 GHz

	SEA	LAND
	ΔT_{BTOA} [K] (emissivity e_s =0.4)	ΔT_{BTOA} [K] (emissivity e_s =0.9)
Low latitude	15.6856	2.5091
Middle latitude	13.0717	1.8472
High latitude	11.0486	1.0885

Concerning the different values of atmospheric optical thickness τ and mean radiative temperature T_{mr} assuming clear sky or cloudy conditions during the simulations, a more complete analysis regarding the variability of τ and T_{mr} for the different latitudes and at RA-2 frequencies was performed. We have carried out a sensitivity analysis considering separately incorrect presence of cloud for clear sky conditions and incorrect clear sky conditions for cloud occurrence. Figures 3.2.8 and 3.2.9 show, respectively, τ and T_{mr_up} differences considering incorrect clear sky conditions.

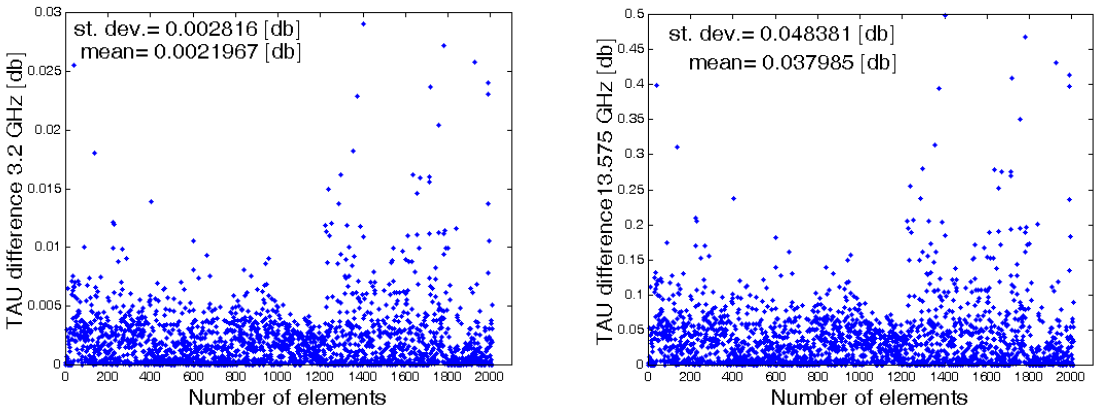

(a)

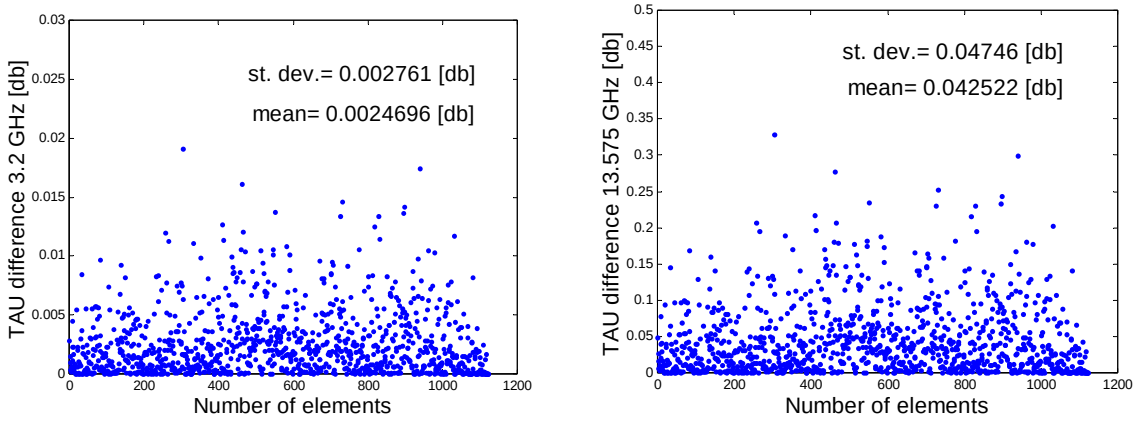

(b)

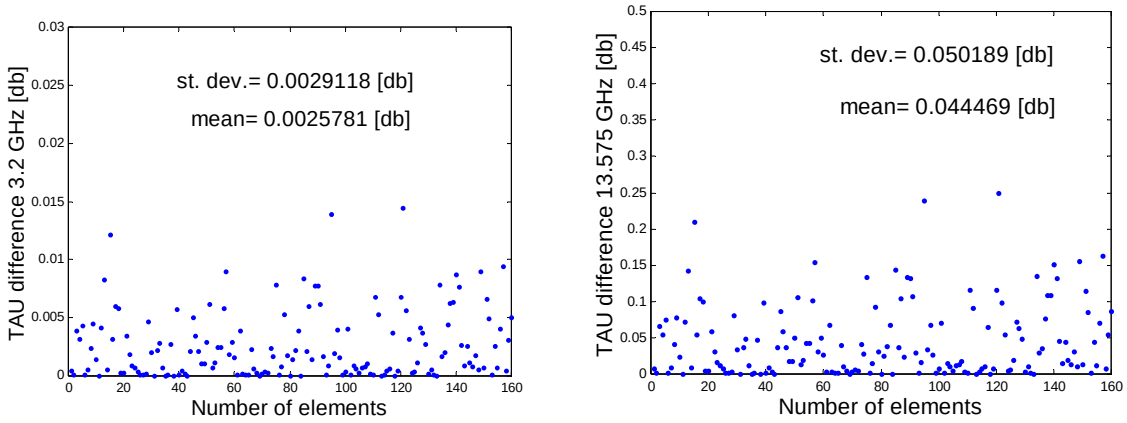

(c)

Fig. 3.2.8 τ differences considering incorrect clear sky conditions (τ_{cloudy}-$\tau_{clearsky}$) for low (figure a), middle (figure b), high latitudes (figure c) and for 3.2 GHz (left panels) and 13.575 GHz (right panels)

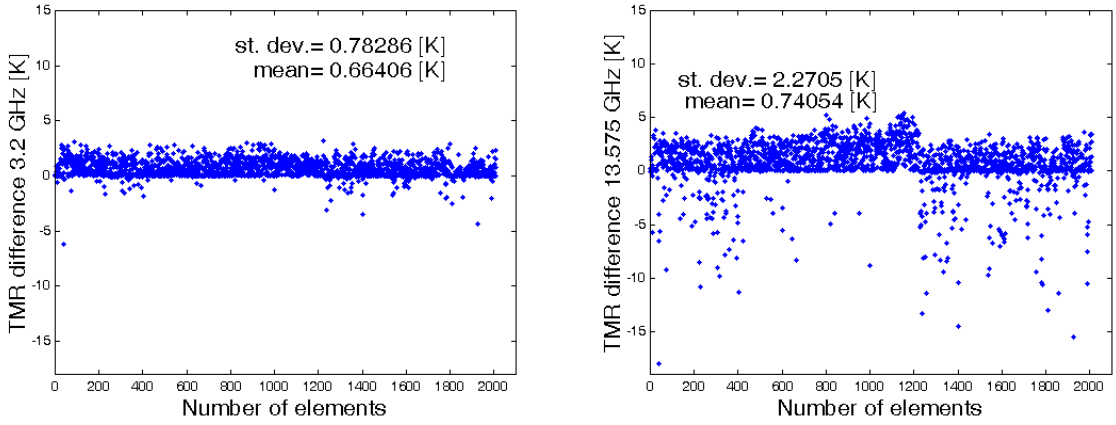

(a)

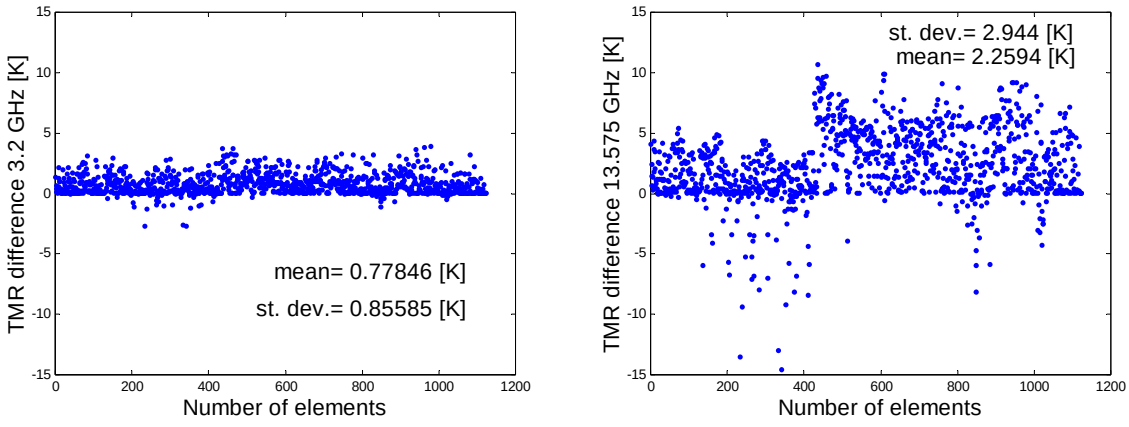

(b)

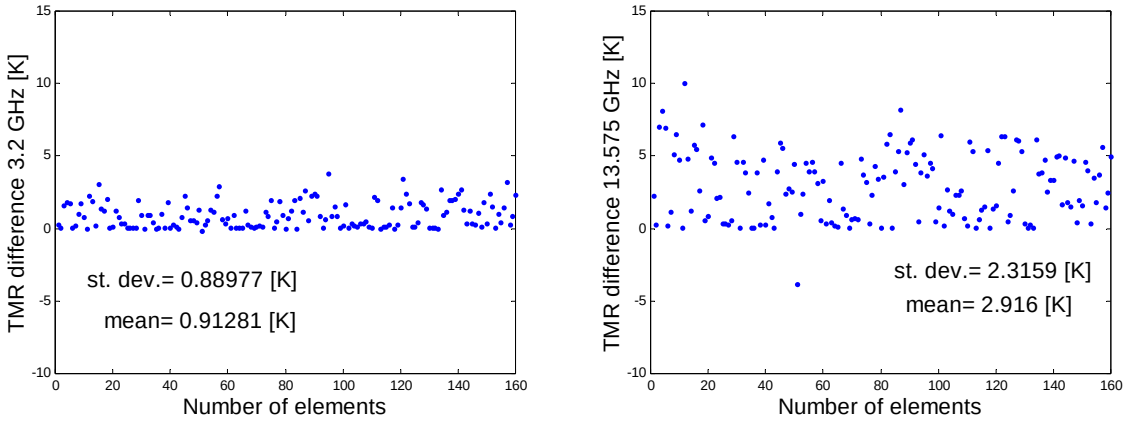

(c)

Fig. 3.2.9 Tmr_up differences considering incorrect clear sky conditions (Tmr_up_{cloudy}-$Tmr\_up_{clearsky}$) for low (figure a), middle (figure b) high latitudes (figure c) and for 3.2GHz (left panels) and 13.575 GHz (right panels)

As described previously, a T_{BTOA} sensitivity analysis (T_{BTOA} derivatives versus τ and T_{mr}) was performed for incorrect clear sky or cloudy conditions assumption, considering again a mean value for T_s of 283.13 K and the two sea and land emissivity values, respectively of 0.4 and 0.9. A summary of sensitivities is reported in tables 3.2.III and 3.2.IV:

TABLE 3.2.III T_{BTOA} ERROR: INCORRECT ASSUMPTION OF PRESENCE OF CLOUD IN CASE OF CLEAR SKY

3.2 GHz

	ΔT_{BTOA} [K] (e_s =0.4)	ΔT_{BTOA} [K] (e_s =0.9)
Low latitude	0.8397	0.1321
Middle latitude	0.7826	0.0870
High latitude	0.8102	0.0822

13.575 GHz

	ΔT_{BTOA} [K] (e_s =0.4)	ΔT_{BTOA} [K] (e_s =0.9)
Low latitude	13.0856	2.0797
Middle latitude	12.6664	1.5330
High latitude	13.3698	1.4212

TABLE 3.2.IV T_{BTOA} ERROR: INCORRECT ASSUMPTION OF CLEAR SKY IN THE PRESENCE OF CLOUDS

3.2 GHz

	ΔT_{BTOA} [K] (e_s =0.4)	ΔT_{BTOA} [K] (e_s =0.9)
Low latitude	0.8390	0.1342
Middle latitude	0.7821	0.0894
High latitude	0.8102	0.0852

13.575 GHz

	ΔT_{BTOA} [K] (e_s =0.4)	ΔT_{BTOA} [K] (e_s=0.9)
Low latitude	14.4435	2.3180
Middle latitude	11.7660	1.5118
High latitude	12.4098	1.4210

3.3 On-line input data

Different sources of input data for the atmospheric models are considered, namely:

- atmospheric profiles of pressure, temperature and humidity from radiosounding observations (RAOB), available only on specific stations at synoptic hours (two or four times per day);
- same kind of profiles at 16 to 18 predefined levels, plus additional information on the atmosphere status (rain, clouds, columnar liquid content), obtained from general circulation models operated by numerical weather prediction centres, such as ECMWF or NCEP on a regular grid (with spacing ranging from 40 to 100 km) at selected times (every 3 hours for forecasts or 6 hours for analyses);
- standard satellite products such as columnar vapour and liquid, mainly obtainable over oceans at passes of currently available satellites carrying on board microwave radiometers (SSM/I, TMI).

More details on input data are reported in section 2.2.5.

3.4 Algorithms for τ, Tmr (up and down) and rain flag

The purpose of this section is to give a brief description of the algorithms that we used for the computation of atmospheric opacity τ and mean radiative temperature T_{mr} (up and down) from the input data mentioned in the previous section, considering both the case of conventional data (atmospheric profiles) and the case of remotely sensed data (standard satellite products). In addition, the production of a flag indicating the presence of rain is considered.

3.4.1 Using conventional data

Profiles of atmospheric thermodynamic variables available from radiosounding observations or from numerical models, are used to compute atmospheric opacity τ and mean radiative temperature T_{mr}. The theory of radiative transfer for a non-scattering horizontally stratified atmosphere in local thermodynamic equilibrium at microwave frequencies can be applied. In our computations the *Liebe* [1985] water vapour and oxygen absorption model and the *Decker* [1978] cloud model, exploiting a relationship between cloud thickness and cloud water density, have been used. In particular, these algorithms are valid for frequencies below 100 GHz in the absence of precipitating hydrometeors. The T_{mr} is evaluated both for upward-looking and downward-looking cases.

The simulation of τ and T_{mr} using the above algorithms has been performed using as input data vertical profiles of atmospheric temperature, relative humidity and pressure to completely define the composition of the atmosphere, at the sites of interest. To better approximate a continuous atmosphere, profiles have been extrapolated to 0.1 hPa and interpolated between available levels with atmospheric models.

At the zenith, τ in neper, depending on frequency *f*, is defined as follows:

$$\tau(f) = \int_0^\infty \alpha(f,z)dz \tag{3.4.1}$$

where $\alpha(f,z)$ is the atmospheric volume absorption coefficient (Np km^{-1}) and *z* is the spatial position of the emitting air volume (km); when considering observations along slant paths, the simple secant mapping function can be used.

T_{mr} in Kelvin, also depending on frequency *f*, is defined as follows:

$$T_{mr}(f) = \frac{\int_0^\infty T(z)\alpha(f,z)e^{-\tau_f(0,z)}dz}{\int_0^\infty \alpha(f,z)e^{-\tau_f(o,z)}dz} \tag{3.4.2}$$

where $T(z)$ is the absolute physical air temperature (K), *z* is the spatial position of the emitting air volume (km) and $\tau_f(0,z)$ (Np) is the optical depth of the atmospheric layer between (0,*z*). For T_{mr} the dependence on the viewing angle is very weak, as shown in section 3.2.

As far as the rain flag is concerned, the possible presence of rain is predicted by numerical models, while there is a lack of information about rainy conditions when considering RAOB's.

3.4.2 Using remotely sensed data

An alternative approach for the computation of atmospheric opacity τ and mean radiative temperature T_{mr} at RA-2 frequencies has been developed, starting from the availability of microwave measurements from remote sensing satellites, such as DMSP and TRMM over the selected sites. The procedure basically implement a frequency scaling approach to derive parameters at S and Ku bands from radiometric measurements at different frequency bands and it envisages two successive steps:

- retrieval of IPWV and ICL from satellite measurements using literature algorithms;
- determination of a statistical relationship among available predictors (IPWV, ICL and ancillary surface atmospheric parameters as pressure, temperature and humidity) and the sought e.m. variables (τ and T_{mr}).

For the first step we refer in the following to the case of SSM/I measurements processed using the *Gerard and Eymard* [1998] algorithm. The algorithm, developed to infer Integrated Cloud Liquid and Integrated Precipitable Water Vapour over oceans from the SSM/I channels, is given by:

$$\begin{aligned} IPWV &= 236.552 - 14.419\ln(280 - T_{19v}) - 24.667\ln(280 - T_{19h}) \\ &\quad - 26.995\ln(280 - T_{22v}) - 8.057\ln(280 - T_{37v}) + 24.339\ln(280 - T_{37h}) \end{aligned} \tag{3.4.3}$$

$$\begin{aligned} ICL &= 1.245096 - 0.066106\ln(280 - T_{19v}) + 1.121951\ln(280 - T_{19h}) \\ &\quad + 0.098642\ln(280 - T_{22v}) - 0.395627\ln(280 - T_{37v}) - 1.094893\ln(280 - T_{37h}) \end{aligned}$$

These relationships were obtained from simulated observations computed by a microwave radiative transfer model (*Liebe* [93], to compute water vapour absorption) applied to a set of about 10,000 atmospheric profiles (between 60°S and 60°N, in August 1992) from the ECMWF forecast model. Liquid water content profiles were computed from a prognostic cloud scheme implemented in the operational ECMWF forecast model in 1998. On the database composed of the simulated brightness temperatures T_B and of ICL and IPWV computed from the corresponding atmospheric profiles, *Gerard and Eymard* applied a linear multiple regression to derive the algorithm coefficients. The algorithm was than applied to the simulated brightness temperatures from their own database and compared with the database values. The retrieval accuracy (including instrumental noise) resulted in 1.42 mm and 0.0257mm for IPWV and ICL respectively.

For the second step, we considered both linear and polynomial multiple regression approaches according to the following expressions:

$$\begin{aligned} \tau &= a_0 + a_1 IPWV + a_2 ICL + [a_3 T_s + a_4 P_s + a_5 RH_s] + [a_6 (IPWV)^2 + a_7 (ICL)^2 + a_8 (IPWV)^3 + a_9 (ICL)^3] \\ T_{mr\_up} &= b_0 + b_1 IPWV + b_2 ICL + [b_3 T_s + b_4 P_s + b_5 RH_s] + [b_6 (IPWV)^2 + b_7 (ICL)^2 + b_8 (IPWV)^3 + b_9 (ICL)^3] \\ T_{mr\_dn} &= c_0 + c_1 IPWV + c_2 ICL + [c_3 T_s + c_4 P_s + c_5 RH_s] + [c_6 (IPWV)^2 + c_7 (ICL)^2 + c_8 (IPWV)^3 + c_9 (ICL)^3] \end{aligned} \tag{3.4.4}$$

where terms in square brackets represent optional predictors including powers (up to the third order) of IPWV and ICL, and/or ancillary measurements. The retrieval coefficients a_i, b_i and c_i of the above relationships were determined using the RAOB database for the three latitude zones as described in section 3.2, considering the models mentioned in section 3.4.1 for the computation of τ and T_{mr} at RA-2 frequencies.

In the following figures we show an example (for middle latitudes) of the performances of the regression approaches using different set of predictors, considering linear and polynomial cases, in terms of scatterplots of retrieved values versus true values of the e.m. parameters, together with correlation coefficients, a-priori variability within the database and retrieval r.m.s. errors.

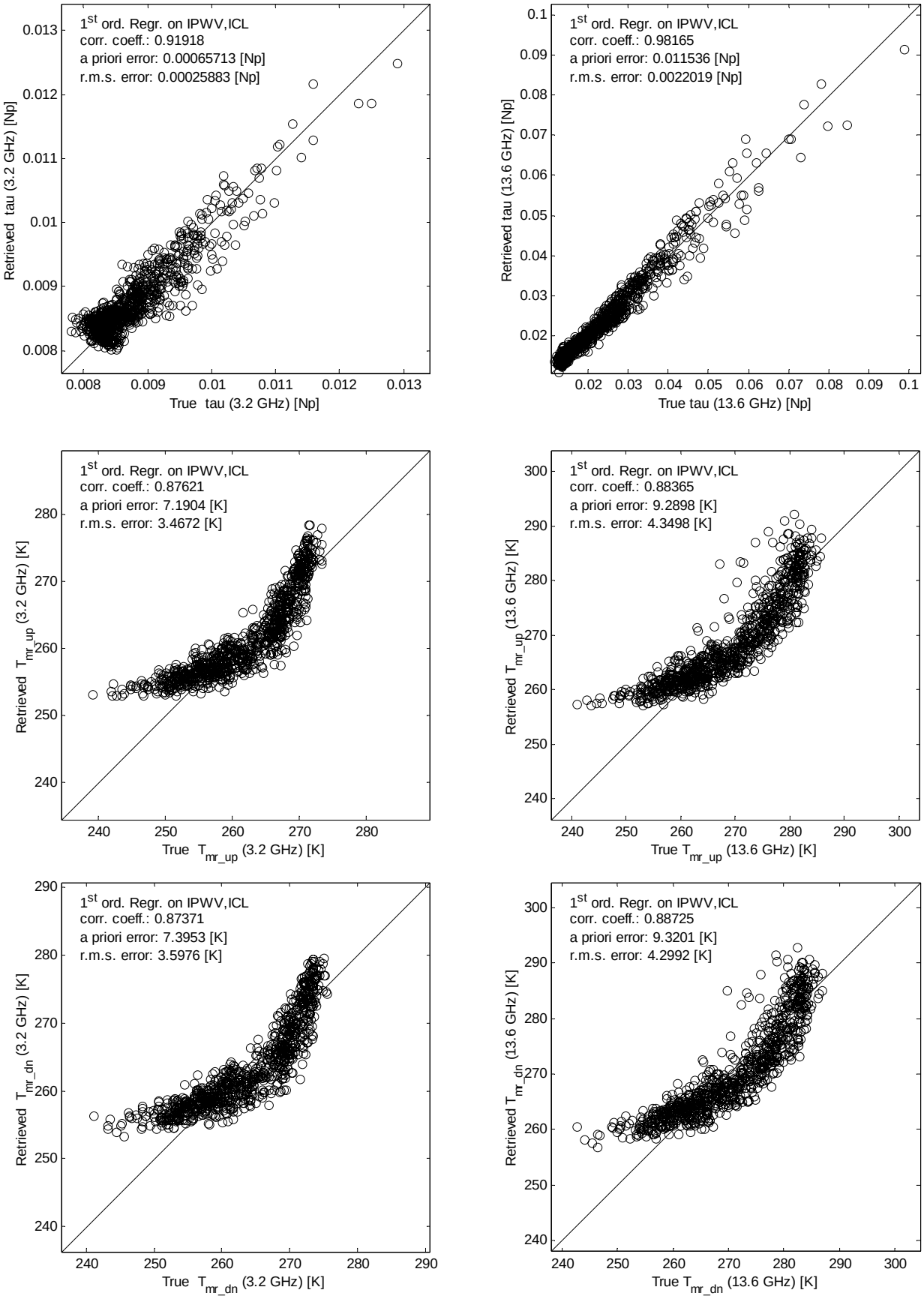

Fig. 3.4.1 Linear regression based on IPWV and ICL: scatterplots of retrieved values versus true values of tau (top panels), T_{mr_up} (middle panels) and T_{mr_dn} (bottom panels), at 3.2 (left panels) and 13.575 GHz (right panels), for middle latitudes.

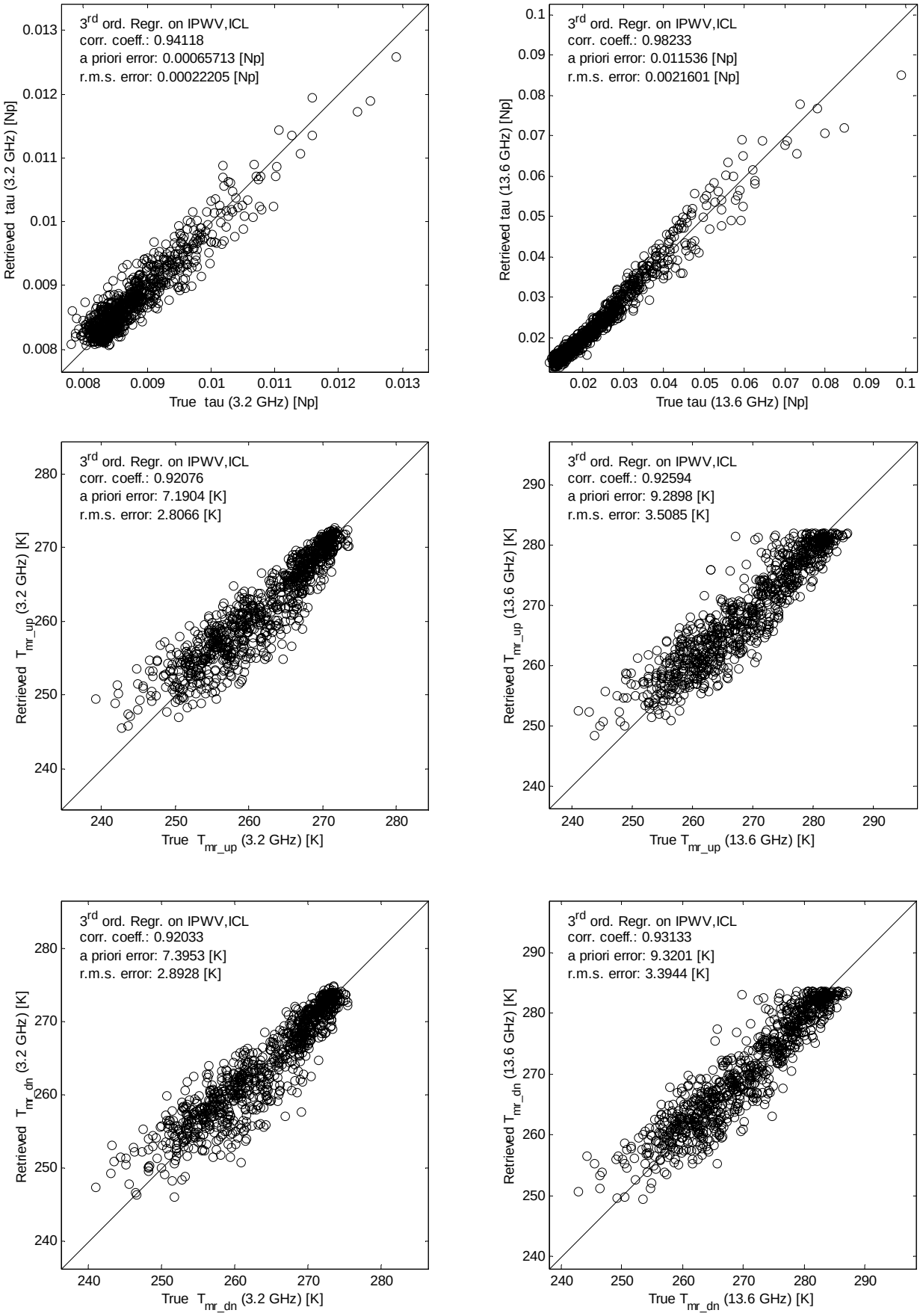

Fig. 3.4.2 3rd order polynomial regression based on IPWV and ICL: scatterplots of retrieved values versus true values of tau (top panels), T_{mr_up} (middle panels) and T_{mr_dn} (bottom panels), at 3.2 (left panels) and 13.575 GHz (right panels), for middle latitudes.

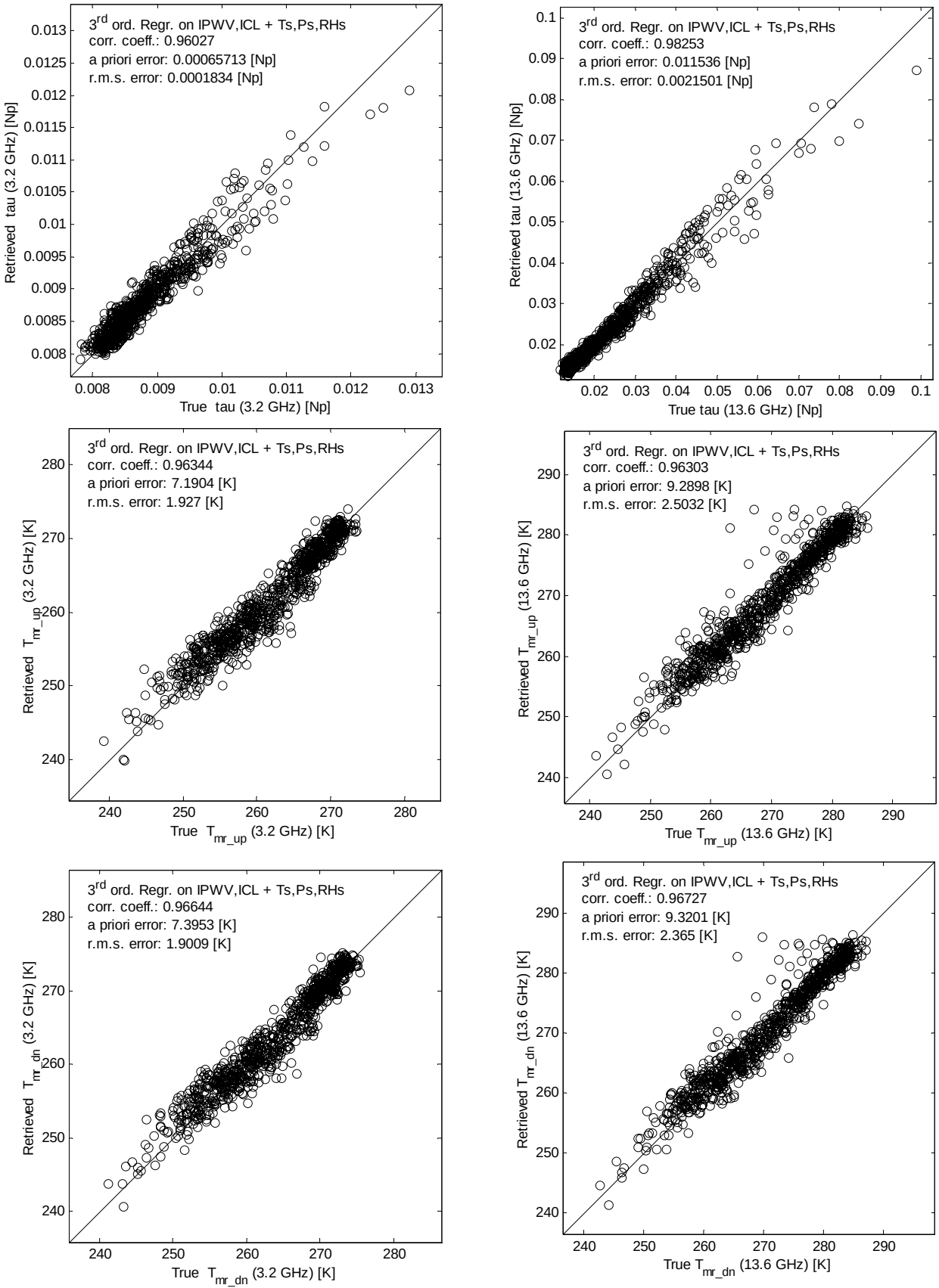

Fig. 3.4.3 3rd order polynomial regression based on IPWV and ICL, plus T_S, P_S and RH_S: scatterplots of retrieved values versus true values of tau (top panels), T_{mr_up} (middle panels) and T_{mr_dn} (bottom panels), at 3.2 (left panels) and 13.575 GHz (right panels), for middle latitudes.

In the following tables we report the retrieval coefficients a_i, b_i and c_i (tables A), and the statistical parameters describing the accuracy (tables B) of the regression approaches using different set of predictors, considering linear and polynomial cases, for the three latitude zones.

TABLE 3.4.I LINEAR REGRESSION BASED ON IPWV AND ICL, FOR LOW LATITUDES: (A) RETRIEVAL COEFFICIENTS FOR TAU, T_{mr_up} AND T_{mr_dn}; (B) A PRIORI ERROR, RETRIEVAL RMS ERROR, AND CORRELATION COEFFICIENTS

(A)

tau	**a_0**	**a_1**	**a_2**
3.2 GHz	7.775e-3	9.844e-5	1.737e-2
13.6 GHz	1.021e-2	3.612e-3	2.972e-1
T_{mr_up}	**b_0**	**b_1**	**b_2**
3.2 GHz	2.645e+2	1.596e+0	-3.942e+0
13.6 GHz	2.730e+2	2.052e+0	-1.860e+1
T_{mr_dn}	**c_0**	**c_1**	**c_2**
3.2 GHz	2.673e+2	1.472e+0	-3.963e+0
13.6 GHz	2.750e+2	1.978e+0	-1.733e+1

(B)

tau	**a priori error**	**rms error**	**correlation coeff.**
3.2 GHz	7.001e-4	2.186e-4	0.950
13.6 GHz	1.310e-2	2.090e-3	0.987
T_{mr_up}	**a priori error**	**rms error**	**correlation coeff.**
3.2 GHz	2.633e+0	1.816e+0	0.724
13.6 GHz	3.715e+0	2.937e+0	0.612
T_{mr_dn}	**a priori error**	**rms error**	**correlation coeff.**
3.2 GHz	2.463e+0	1.719e+0	0.715
13.6 GHz	3.553e+0	2.764e+0	0.628

TABLE 3.4.II 3^{RD} ORDER POLYNOMIAL REGRESSION BASED ON IPWV AND ICL, FOR LOW LATITUDES: (A) RETRIEVAL COEFFICIENTS FOR TAU, T_{mr_up} AND T_{mr_dn}; (B) A PRIORI ERROR, RETRIEVAL RMS ERROR, AND CORRELATION COEFFICIENTS

(A)

tau	**a_0**	**a_1**	**a_2**	**a_6**	**a_7**	**a_8**	**a_9**
3.2 GHz	7.089e-3	7.044e-4	1.384e-2	-1.556e-4	3.448e-2	1.240e-5	-4.633e-2
13.6 GHz	1.019e-2	3.779e-3	2.500e-1	-1.002e-5	3.422e-1	2.980e-7	-7.861e-2
T_{mr_up}	**b_0**	**b_1**	**b_2**	**b_6**	**b_7**	**b_8**	**b_9**
3.2 GHz	2.661e+2	-7.039e-1	-3.807e+0	8.667e-1	9.043e+1	-9.389e-2	-3.205e+2
13.6 GHz	2.662e+2	5.740e+0	5.427e+1	-4.002e-1	-6.886e+2	-2.112e-2	1.354e+3
T_{mr_dn}	**c_0**	**c_1**	**c_2**	**c_6**	**c_7**	**c_8**	**c_9**
3.2 GHz	2.663e+2	1.611e+0	-8.499e-1	1.788e-1	4.645e+1	-3.388e-2	-2.124e+2
13.6 GHz	2.663e+2	7.503e+0	4.721e+1	-9.283e-1	-5.971e+2	2.613e-2	1.177e+3

(B)

tau	**a priori error**	**rms error**	**correlation coeff.**
3.2 GHz	7.001e-4	2.061e-4	0.956
13.6 GHz	1.310e-2	1.926e-3	0.989
T_{mr_up}	**a priori error**	**rms error**	**correlation coeff.**
3.2 GHz	2.633e+0	1.786e+0	0.735
13.6 GHz	3.715e+0	2.563e+0	0.724
T_{mr_dn}	**a priori error**	**rms error**	**correlation coeff.**
3.2 GHz	2.463e+0	1.688e+0	0.728
13.6 GHz	3.553e+0	2.456e+0	0.723

TABLE 3.4.III 3^{RD} ORDER POLYNOMIAL REGRESSION BASED ON IPWV AND ICL WITH ADDITIONAL LINEAR PREDICTORS T_S, P_S, RH_S, FOR LOW LATITUDES: (A) RETRIEVAL COEFFICIENTS FOR TAU, T_{mr_up} AND T_{mr_dn}; (B) A PRIORI ERROR, RETRIEVAL RMS ERROR, AND CORRELATION COEFFICIENTS

(A)

tau	a_0	a_1	a_2	a_3	a_4	a_5	a_6	a_7	a_8	a_9
3.2 GHz	-2.497e-3	3.426e-5	1.513e-2	-2.034e-5	1.631e-5	-5.987e-5	1.887e-5	1.124e-2	-1.373e-6	1.976e-2
13.6 GHz	-2.122e-2	1.915e-3	2.577e-1	2.289e-5	2.545e-5	1.512e-3	4.849e-4	2.475e-1	-4.329e-5	1.856e-1
T_{mr_up}	b_0	b_1	b_2	b_3	b_4	b_5	b_6	b_7	b_8	b_9
3.2 GHz	1.861e+2	-7.541e-2	1.582e+1	4.118e-1	-4.339e-2	2.987e+0	3.821e-1	-1.820e+1	-4.477e-2	-1.354e+2
13.6 GHz	1.295e+2	4.978e+0	7.329e+1	5.945e-1	-4.284e-2	8.972e+0	-6.964e-1	-7.822e+2	1.708e-2	1.501e+3
T_{mr_dn}	c_0	c_1	c_2	c_3	c_4	c_5	c_6	c_7	c_8	c_9
3.2 GHz	1.699e+2	6.125e-1	1.839e+1	4.320e-1	-3.116e-2	3.059e+0	1.017e-1	-4.914e+1	-1.774e-2	-5.156e+1
13.6 GHz	1.212e+2	4.930e+0	6.430e+1	5.982e-1	-3.288e-2	8.326e+0	-7.665e-1	-6.580e+2	2.814e-2	1.233e+3

(B)

tau	a priori error	rms error	correlation coeff.
3.2 GHz	7.001e-4	1.437e-4	0.979
13.6 GHz	1.310e-2	1.931e-3	0.989
T_{mr_up}	**a priori error**	**rms error**	**correlation coeff.**
3.2 GHz	2.633e+0	1.721e+0	0.762
13.6 GHz	3.715e+0	2.516e+0	0.743
T_{mr_dn}	**a priori error**	**rms error**	**correlation coeff.**
3.2 GHz	2.463e+0	1.614e+0	0.762
13.6 GHz	3.553e+0	2.420e+0	0.739

TABLE 3.4.IV LINEAR REGRESSION BASED ON IPWV AND ICL, FOR MIDDLE LATITUDES: (A) RETRIEVAL COEFFICIENTS FOR TAU, T_{mr_up} AND T_{mr_dn}; (B) A PRIORI ERROR, RETRIEVAL RMS ERROR, AND CORRELATION COEFFICIENTS

(A)

tau	a_0	a_1	a_2
3.2 GHz	8.626e-3	-1.160e-4	2.110e-2
13.6 GHz	1.229e-2	2.815e-3	3.426e-1
T_{mr_up}	b_0	b_1	b_2
3.2 GHz	2.520e+2	4.813e+0	-1.862e+1
13.6 GHz	2.557e+2	6.262e+0	-2.279e+0
T_{mr_dn}	c_0	c_1	c_2
3.2 GHz	2.536e+2	4.992e+0	-2.387e+1
13.6 GHz	2.571e+2	6.355e+0	-6.887e+0

(B)

tau	a priori error	rms error	correlation coeff.
3.2 GHz	6.571e-4	2.588e-4	0.919
13.6 GHz	1.154e-2	2.202e-3	0.982
T_{mr_up}	**a priori error**	**rms error**	**correlation coeff.**
3.2 GHz	7.190e+0	3.467e+0	0.876
13.6 GHz	9.290e+0	4.350e+0	0.884
T_{mr_dn}	**a priori error**	**rms error**	**correlation coeff.**
3.2 GHz	7.395e+0	3.598e+0	0.874
13.6 GHz	9.320e+0	4.2994e+0	0.887

TABLE 3.4.V 3^{RD} ORDER POLYNOMIAL REGRESSION BASED ON IPWV AND ICL, FOR MIDDLE LATITUDES: (A) RETRIEVAL COEFFICIENTS FOR TAU, T_{mr_up} AND T_{mr_dn}; (B) A PRIORI ERROR, RETRIEVAL RMS ERROR, AND CORRELATION COEFFICIENTS

(A)

tau	a_0	a_1	a_2	a_6	a_7	a_8	a_9
3.2 GHz	9.137e-3	-8.543e-4	2.215e-2	2.457e-4	-1.534e-2	-2.211e-5	7.169e-2
13.6 GHz	1.324e-2	1.396e-3	3.084e-1	5.249e-4	7.684e-1	-5.153e-5	-3.648e+0
T_{mr_up}	b_0	b_1	b_2	b_6	b_7	b_8	b_9
3.2 GHz	2.446e+2	1.442e+1	-5.117e+1	-2.762e+0	5.388e+2	1.975e-1	-1.820e+3
13.6 GHz	2.472e+2	1.586e+1	4.414e+1	-2.288e+0	-4.749e+2	9.354e-2	-3.637e+1
T_{mr_dn}	c_0	c_1	c_2	c_6	c_7	c_8	c_9

3.2 GHz	2.460e+2	1.515e+1	-5.482e+1	-2.993e+0	3.966e+2	2.217e-1	-6.928e+2
13.6 GHz	2.488e+2	1.598e+1	3.256e+1	-2.359e+0	-4.475e+2	1.052e-1	3.960e+2

(B)

tau	**a priori error**	**rms error**	**correlation coeff.**
3.2 GHz	6.571e-4	2.220e-4	0.941
13.6 GHz	1.154e-2	2.160e-3	0.982
T_{mr_up}	**a priori error**	**rms error**	**correlation coeff.**
3.2 GHz	7.190e+0	2.807e+0	0.921
13.6 GHz	9.290e+0	3.508e+0	0.926
T_{mr_dn}	**a priori error**	**rms error**	**correlation coeff.**
3.2 GHz	7.395e+0	2.893e+0	0.920
13.6 GHz	9.320e+0	3.394e+0	0.931

TABLE 3.4.VI 3RD ORDER POLYNOMIAL REGRESSION BASED ON IPWV AND ICL WITH ADDITIONAL LINEAR PREDICTORS T_S, P_S, RH_S, FOR MIDDLE LATITUDES; (A) RETRIEVAL COEFFICIENTS FOR TAU, T_{mr_up} AND T_{mr_dn}; (B) A PRIORI ERROR, RETRIEVAL RMS ERROR, AND CORRELATION COEFFICIENTS

(A)

tau	**a_0**	**a_1**	**a_2**	**a_3**	**a_4**	**a_5**	**a_6**	**a_7**	**a_8**	**a_9**
3.2 GHz	9.718e-3	-3.968e-4	1.811e-2	-3.196e-5	8.122e-6	-2.122e-4	1.639e-4	3.787e-2	-1.596e-5	-1.817e-1
13.6 GHz	2.575e-2	4.607e-4	3.109e-1	1.490e-5	-1.675e-5	1.183e-3	8.542e-4	6.381e-1	-8.690e-5	-2.883e+0
T_{mr_up}	**b_0**	**b_1**	**b_2**	**b_3**	**b_4**	**b_5**	**b_6**	**b_7**	**b_8**	**b_9**
3.2 GHz	-4.573e+0	7.133e+0	8.421e+0	5.487e-1	9.831e-2	4.176e+0	-2.002e+0	2.492e+2	1.781e-1	-1.391e+3
13.6 GHz	-4.594e+1	6.316e+0	9.579e+1	7.174e-1	9.259e-2	1.013e+1	-1.196e+0	-6.071e+2	5.189e-2	-2.585e+2
T_{mr_dn}	**c_0**	**c_1**	**c_2**	**c_3**	**c_4**	**c_5**	**c_6**	**c_7**	**c_8**	**c_9**
3.2 GHz	-1.705e+1	7.417e+0	1.183e+1	5.716e-1	1.058e-1	4.363e+0	-2.104e+0	9.388e+1	1.878e-1	-6.999e+2
13.6 GHz	-5.517e+1	5.964e+0	8.912e+1	7.488e-1	9.463e-2	1.044e+1	-1.119e+0	-5.458e+2	4.494e-2	-5.302e+2

(B)

tau	**a priori error**	**rms error**	**correlation coeff.**
3.2 GHz	6.571e-4	1.834e-4	0.960
13.6 GHz	1.154e-2	2.150e-3	0.983
T_{mr_up}	**a priori error**	**rms error**	**correlation coeff.**
3.2 GHz	7.190e+0	1.927e+0	0.963
13.6 GHz	9.290e+0	2.503e+0	0.963
T_{mr_dn}	**a priori error**	**rms error**	**correlation coeff.**
3.2 GHz	7.395e+0	1.901e+0	0.966
13.6 GHz	9.320e+0	2.365e+0	0.967

TABLE 3.4.VII LINEAR REGRESSION BASED ON IPWV AND ICL, FOR HIGH LATITUDES: (A) RETRIEVAL COEFFICIENTS FOR TAU, T_{mr_up} AND T_{mr_dn}; (B) A PRIORI ERROR, RETRIEVAL RMS ERROR, AND CORRELATION COEFFICIENTS

(A)

tau	**a_0**	**a_1**	**a_2**
3.2 GHz	8.861e-3	-3.397e-4	2.292e-2
13.6 GHz	1.345e-2	1.184e-3	3.672e-1
T_{mr_up}	**b_0**	**b_1**	**b_2**
3.2 GHz	2.481e+2	6.816e+0	1.078e-1
13.6 GHz	2.515e+2	8.439e+0	3.010e+1
T_{mr_dn}	**c_0**	**c_1**	**c_2**
3.2 GHz	2.496e+2	6.753e+0	-4.900e+0
13.6 GHz	2.533e+2	8.082e+0	2.742e+1

(B)

tau	**a priori error**	**rms error**	**correlation coeff.**
3.2 GHz	6.814e-4	2.258e-4	0.945
13.6 GHz	1.317e-2	1.540e-3	0.993
T_{mr_up}	**a priori error**	**rms error**	**correlation coeff.**

3.2 GHz	4.811e+0	2.689e+0	0.831
13.6 GHz	6.244e+0	3.463e+0	0.840
T_{mr_dn}	**a priori error**	**rms error**	**correlation coeff.**
3.2 GHz	4.792e+0	2.570e+0	0.844
13.6 GHz	6.167e+0	3.389e+0	0.840

TABLE 3.4.VIII 3RD ORDER POLYNOMIAL REGRESSION BASED ON IPWV AND ICL FOR HIGH LATITUDES; (A) RETRIEVAL COEFFICIENTS FOR TAU, T_{mr_up} AND T_{mr_dn}; (B) A PRIORI ERROR, RETRIEVAL RMS ERROR, AND CORRELATION COEFFICIENTS

(A)

tau	**a_0**	**a_1**	**a_2**	**a_6**	**a_7**	**a_8**	**a_9**
3.2 GHz	9.043e-3	-7.461e-4	1.693e-2	2.871e-4	1.453e-1	-6.261e-5	-7.571e-1
13.6 GHz	1.171e-2	3.024e-3	2.988e-1	3.859e-4	1.717e+0	-3.806e-4	-9.574e+0
T_{mr_up}	**b_0**	**b_1**	**b_2**	**b_6**	**b_7**	**b_8**	**b_9**
3.2 GHz	2.456e+2	1.044e+1	-6.823e+0	-1.000e+0	4.655e+1	-2.440e-2	-2.740e+2
13.6 GHz	2.463e+2	1.572e+1	2.126e+2	-3.288e+0	-3.574e+3	3.751e-1	1.613e+4
T_{mr_dn}	**c_0**	**c_1**	**c_2**	**c_6**	**c_7**	**c_8**	**c_9**
3.2 GHz	2.431e+2	2.023e+1	5.361e+1	-7.954e+0	-1.703e+3	1.402e+0	1.048e+4
13.6 GHz	2.440e+2	2.624e+1	2.777e+2	-1.128e+1	-5.455e+3	2.058e+0	2.800e+4

(B)

tau	**a priori error**	**rms error**	**correlation coeff.**
3.2 GHz	6.814e-4	2.466e-4	0.934
13.6 GHz	1.317e-2	1.862e-3	0.990
T_{mr_up}	**a priori error**	**rms error**	**correlation coeff.**
3.2 GHz	4.811e+0	2.330e+0	0.875
13.6 GHz	6.244e+0	2.872e+0	0.893
T_{mr_dn}	**a priori error**	**rms error**	**correlation coeff.**
3.2 GHz	4.792e+0	2.799e+0	0.824
13.6 GHz	6.167e+0	3.871e+0	0.824

TABLE 3.4.IX 3RD ORDER POLYNOMIAL REGRESSION BASED ON IPWV AND ICL WITH ADDITIONAL LINEAR PREDICTORS T_S, P_S, RH_S, FOR HIGH LATITUDES: (A) RETRIEVAL COEFFICIENTS FOR TAU, T_{mr_up} AND T_{mr_dn}; (B) A PRIORI ERROR, RETRIEVAL RMS ERROR, AND CORRELATION COEFFICIENTS

(A)

tau	**a_0**	**a_1**	**a_2**	**a_3**	**a_4**	**a_5**	**a_6**	**a_7**	**a_8**	**a_9**
3.2 GHz	1.326e-2	-2.716e-6	1.559e-2	-5.305e-5	1.045e-5	-5.077e-4	1.301e-4	1.400e-1	-5.374e-5	-8.075e-1
13.6 GHz	5.941e-2	2.559e-3	2.950e-1	-1.953e-4	8.582e-6	-2.954e-3	2.006e-3	1.739e+0	-7.836e-4	-1.023e+1
T_{mr_up}	**b_0**	**b_1**	**b_2**	**b_3**	**b_4**	**b_5**	**b_6**	**b_7**	**b_8**	**b_9**
3.2 GHz	-8.053e+1	4.702e+0	7.906e+1	7.918e-1	1.056e-1	6.062e+0	-2.272e+0	-1.321e+3	5.266e-1	7.095e+3
13.6 GHz	-9.110e+1	7.944e+0	3.013e+2	9.130e-1	8.050e-2	1.182e+1	-4.646e+0	-5.002e+3	1.030e+0	2.444e+4
T_{mr_dn}	**c_0**	**c_1**	**c_2**	**c_3**	**c_4**	**c_5**	**c_6**	**c_7**	**c_8**	**c_9**
3.2 GHz	-5.853e+1	4.105e+0	6.054e+1	7.224e-1	1.026e-1	6.712e+0	-1.471e+0	-8.734e+2	3.411e-1	4.261e+3
13.6 GHz	-5.705e+1	8.236e+0	2.745e+2	8.088e-1	7.424e-2	1.293e+1	-4.062e+0	-4.411e+3	8.389e-1	2.093e+4

(B)

tau	**a priori error**	**rms error**	**correlation coeff.**
3.2 GHz	6.814e-4	1.792e-4	0.968
13.6 GHz	1.317e-2	2.034e-3	0.990
T_{mr_up}	**a priori error**	**rms error**	**correlation coeff.**
3.2 GHz	4.811e+0	2.028e+0	0.908
13.6 GHz	6.244e+0	3.027e+0	0.891
T_{mr_dn}	**a priori error**	**rms error**	**correlation coeff.**
3.2 GHz	4.792e+0	1.991e+0	0.911
13.6 GHz	6.167e+0	2.933e+0	0.899

The retrieval coefficients reported in the tables have been computed considering the following uncertainties on the predictors:

IPWV	ICL	T_S	P_S	RH_S
0.142 cm	0.00257 cm	0.5 K	1.0 hPa	2 %

and rms errors and correlation coefficients refer to test sets independent with respect to the training sets.

As far as the rain flag is concerned, the possible presence of rain can be predicted by the Scattering Index (SI) algorithms, based on vertically polarised brightness temperatures measured by the channels of SSM/I on board of DMSP. The following two expressions are considered for sea and land background respectively:

$$SI_{sea} = -174.38 + 0.7152 * T_{B19V} + 2.4387 * T_{B22V} - 0.00504 * (T_{B22V})^2 - T_{B85V} \quad (3.4.5)$$

$$SI_{land} = 451.88 - 0.44 * T_{B19V} - 1.775 * T_{B22V} + 0.00574 * (T_{B22V})^2 - T_{B85V}. \quad (3.4.6)$$

A threshold value of 5 K of SI has been adopted to flag possible rainy data.

Finally, we have evaluated the errors in the atmospheric contribution to T_B caused by the uncertainties on τ and T_{mr}; we have considered the maximum errors in the worst case (linear regression based on IPWV and ICL for middle latitudes) using the following expressions:

$$T_{B\_UP} = T_{mr\_up}(1 - e^{-\tau}) \cong T_{mr\_up}\,\tau \quad (3.4.7)$$

$$\Delta T_{B\_UP} = [(T_{mr\_up} * \Delta\tau)^2 + (\Delta T_{mr\_up} * \tau)^2]^{1/2} \quad (3.4.8)$$

obtaining for the retrieval errors: ΔT_{B_UP}(3.2 GHz) < 0.0825 K and ΔT_{B_UP}(13.6 GHz) < 0.7176 K.

3.5 Processed data and results

During the Phase 2 of the ATMO procedure, ECMWF data acquired during the six-month of "commissioning phase" have been processed to compute the T_B's at the top of the atmosphere, where the contribution of the atmosphere is accounted for by its opacity τ and mean radiative temperature upwelling and downwelling (T_{mr_up} and T_{mr_dn}).

Both τ and T_{mr} have been computed by solving the radiative transfer equation in the absence of atmospheric scattering using *on-line* profiles of meteorological parameters provided by ECMWF analysis and/or forecasts at synoptic hours. T_{mr_up} and T_{mr_dn} and τ at 3.2, 13.575, 10.6, 19.3, 21.2, 22.3, 23.8, and 37.0 GHz have been produced, together with the IPWV, ILC and the rain flag (if available from ECMWF header) over the selected test sites at ENVISAT passes, as reported in 2.3. A list of the ECMWF data processed is reported in the following:

<u>Sahara desert:</u>
3 October 2002 h.09
5 October 2002 h. 18, h.21
6 October 2002 h. 00
12 October 2002 h. 18, h.21
18 October 2002 h.18, h.21
19 October 2002 h.00
6 November 2002 h.18, h.21
7 November 2002 h.00, h.06, h.09, h.12.
9 November 2002 h.21
10 November 2002 h.09
17 November 2002 h. 06, h.09, h.12.
29 November 2002 h.09
2 December 2002 h.21

<u>South Atlantic</u>
5 October 2002 h.00
8 October 2002 h. 00, h.21
10 October 2002 h.12
11 October 2002 h. 12
12 October 2002 h. 00
13 October 2002 h. 12
15 October 2002 h. 00, h.12

<u>North Atlantic</u>
4 October 2002 h.00
5 October 2002 h.12
6 October 2002 h. 12
10 October 2002 h.12
11 October 2002 h. 12
19 October 2002 h.00
20 October 2002 h. 12
21 October 2002 h. 00
14 November 2002 h. 12
15 November 2002 h. 12

<u>Amazon forest</u>
7 November 2002 h. 00
10 November 2002 h. 00
12 November 2002 h. 12
21 November 2002 h. 12
1 December 2002 h. 12

<u>Indian Ocean</u>
21 November 2002 h. 06

<u>Greenland</u>
20 October 2002 h.12, h. 18

7 November 2002 h. 18
8 November 2002 h. 18
10 November 2002 h. 18

For a limited set of passive acquisitions over sea, we obtained products from MWR on board of Envisat generated by CLS. They consist in MWR brightness temperatures as well as atmospheric attenuations at RA-2 frequency bands, derived from MWR itself. This data were fairly valuable since they provided us with a reference both geometrically and temporally matching the RA-2, to be compared to our computations based either on ECMWF or SSM/I-TMI data that were generally not acquired at the time of RA-2 overpass. Figure 3.5.1 shows a comparison of atmospheric attenuations computed from ECMWF analysis with those estimated from the microwave radiometer (MWR) on board of Envisat. The available days are reported in bold in the previous list. In the figure, the high (and less correlated) attenuation values correspond to the presence of clouds.
This behaviour is shown in particular in Figure 3.5.2 for the atmospheric attenuation at the Ku band. The scatterplots show a comparison of τ from ECMWF versus τ from ENVISAT at 13.575 GHz when a limitation to light clouds (ICL<0.2 mm) is applied to ECMWF data only (left) or to ENVISAT data only (right). Red data represent attenuation data when a condition of clear sky (ICL = 0 mm) is considered for both attenuation values.

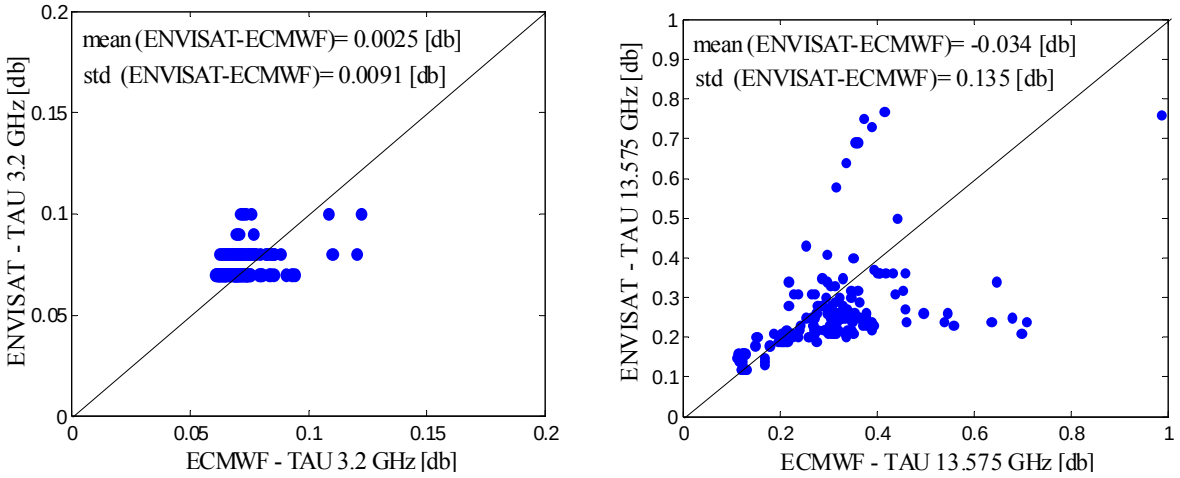

Figure 3.5.1. Comparison of atmospheric attenuations [db] from ECMWF and ENVISAT/MWR at S band (left) and at Ku band (right). MWR estimates have been kindly provided by CLS/Space Oceanography Division.

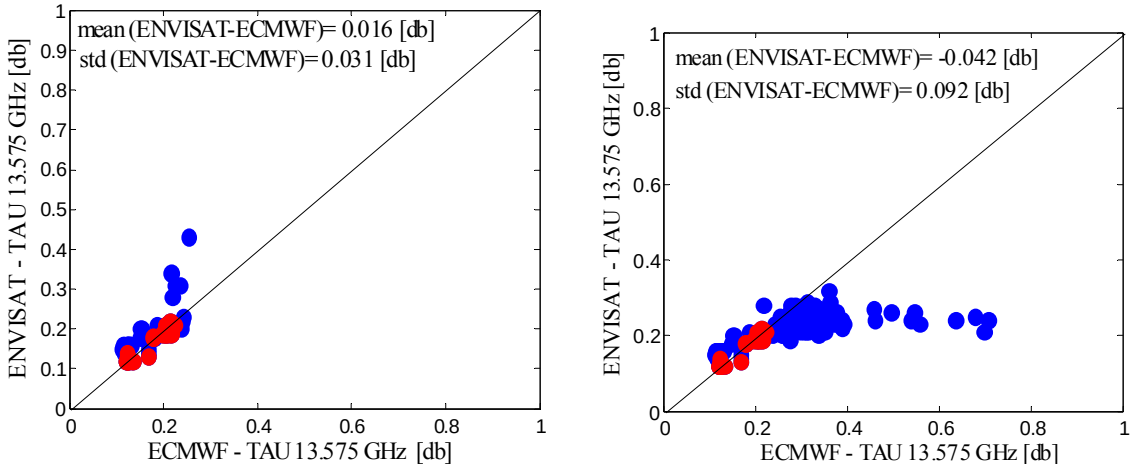

Figure 3.5.2 . TAU from ECMWF compared to TAU from ENVISAT/MWR at 13.575GHz when a light cloud condition (ICL<0.2 mm) is applied to ECMWF data only (left) or to ENVISAT data only (right). Red data correspond to a clear sky condition applied to both attenuation data.

This result is particularly useful for showing how an erroneous cloud occurrence detection, even in the case of light clouds, can lead to a relevant difference in the attenuation values.

3.6 Validation and product accuracy estimates

As a matter of fact a cross check of τ and T_{mr} values derived from ECMWF, RAOB's and from spaceborne radiometers exhibits the main differences in the presence of clouds, showing instead a good agreement in clear sky

conditions. For instance, Figure 3.6.1 shows the cross check of τ and T_{mr} values derived by the radiative transfer model from available ECMWF and co-located and contemporary RAOB's.

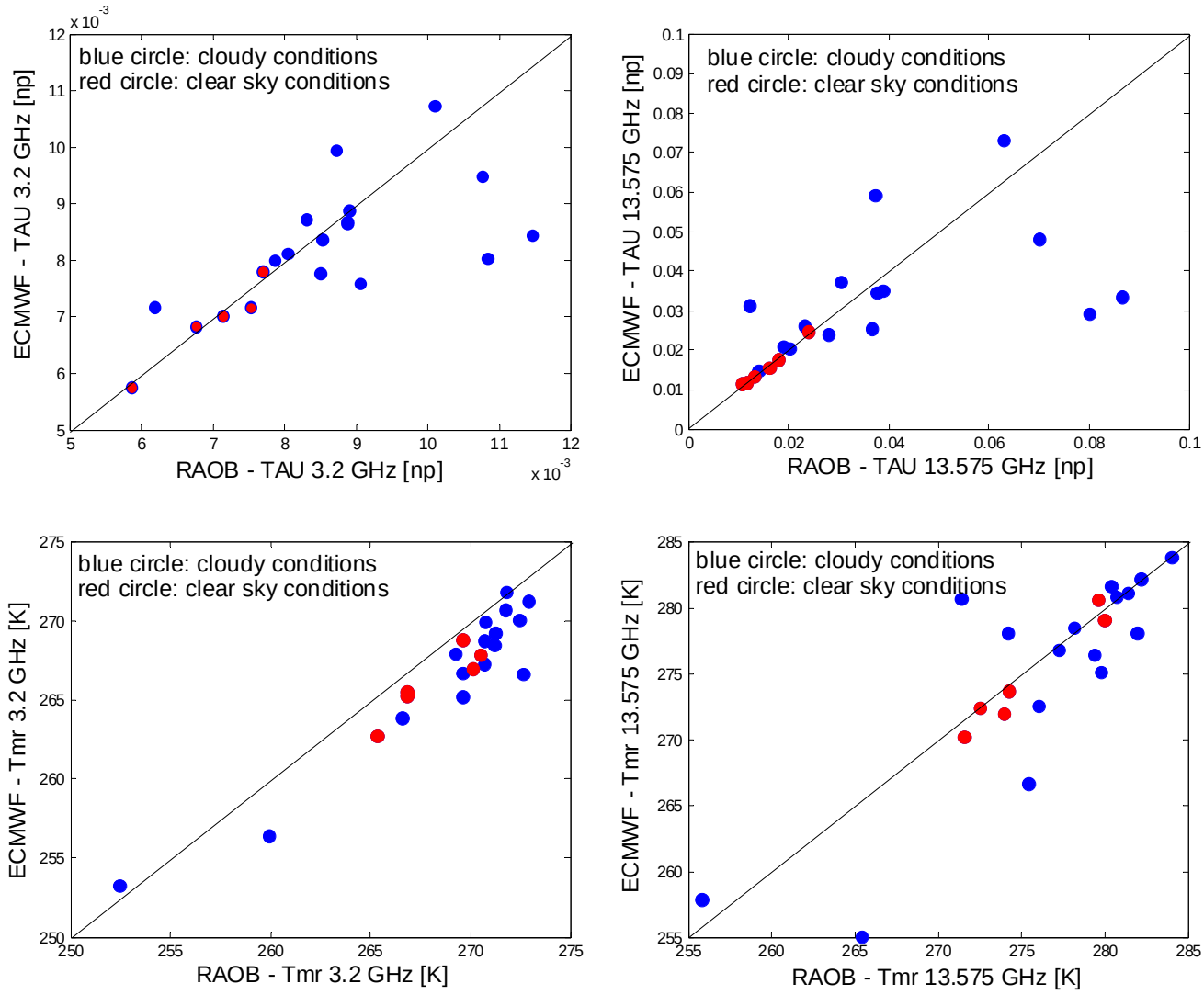

Figure 3.6.1. Cross check of of τ (top) and T_{mr} (bottom) values derived from available ECMWF and (co-located and contemporary) RAOB's, using the radiative transfer model.

Estimates of τ and T_{mr} at the RA-2 frequency bands can be also derived by co-located observations of other satellite-borne microwave radiometers (section 3.4.2). In the mentioned section, after retrieving IPWV and ICL from satellite measurements using SSM/I literature algorithms, we have developed a statistical relationship among available predictors (IPWV, ICL and ancillary surface atmospheric parameters) and the radiative variables (τ and T_{mr}).

Figure 3.6.2 compares τ as computed by solving the radiative transfer equation with τ as computed by using the statistical relationship employing SSM/I estimation of IPWV and ICL, discarding ECMWF and SSM/I data pertaining to cloudy conditions. Such selection has been performed cutting out ECMWF and SSM/I data with ICL>0.0 mm. As expected, SSM/I observations with zero cloud water content exhibit SI<5 K. The analogue comparison for T_{mr} (not shown here) produces an rms error lower than 2 K for both frequencies.

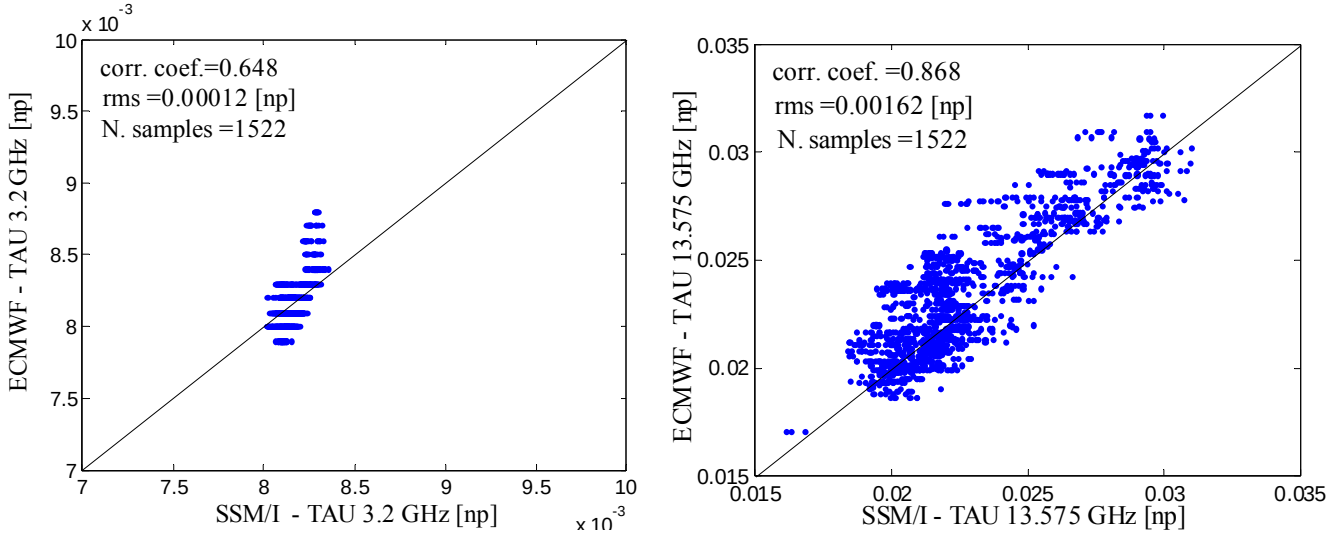

Figure 3.6.2. Comparison of atmospheric attenuations [np] using the radiative transfer model and using the statistical relationship derived from SSM/I data at S band (left panel) and at Ku band (right panel) during clear sky conditions.

It is worth mentioning that, when ECMWF data with ICL>0.0 mm or SSM/I data with ICL>0.0 mm are discarded separately, a tail of mismatched attenuation values is evident. Such tail can be ascribed to different cloud detection using the two approaches, due to several reasons, including the different characteristics in terms of spatial and temporal resolutions.

Figure 3.6.3 shows the comparison at Ku band when the cloud threshold is considered separately.

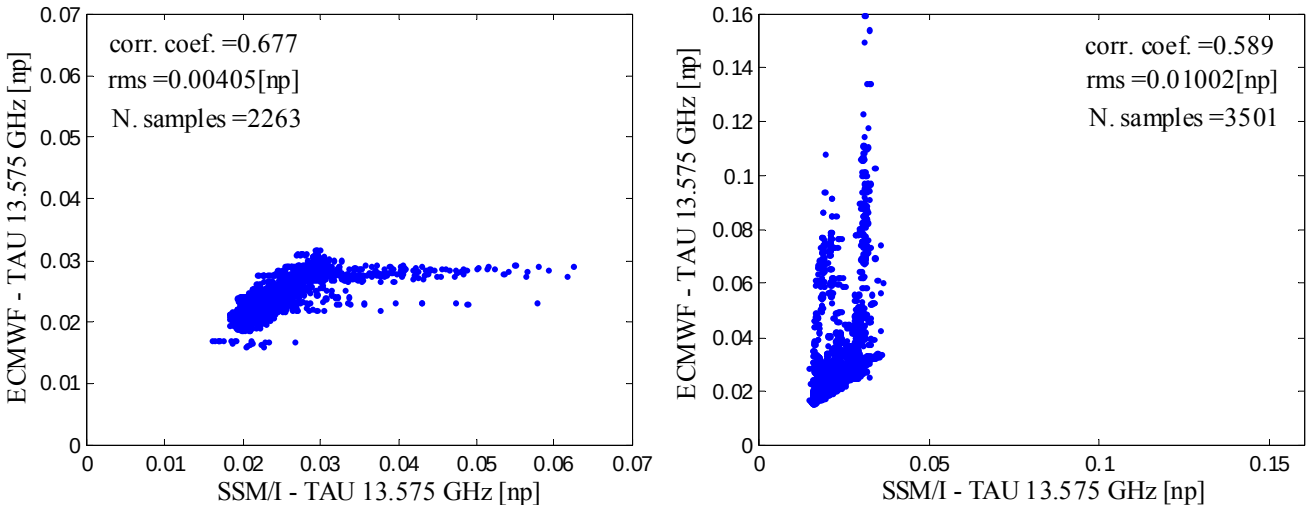

Figure 3.6.3. Comparison of atmospheric attenuations [np] using the radiative transfer model and using the statistical relationship derived from SSM/I data at Ku band, discarding ECMWF data with ICL>0.0 mm (left panel) or SSM/I data with ICL>0.0 mm (right panel).

The reduced accuracy in terms of rms error and correlation coefficient due to an erroneous cloud occurrence detection suggests the employment of RAOB's, ECMWF and SSM/I data with ICL=0.

As evinced from the figures above, the different values of atmospheric optical thickness τ due to the incorrect presence of cloud can lead to an error for the Ku band, in the worst case, of about 0.1 np, difference also confirmed by the results reported in section 3.2.

One of the main conclusion of this analysis is the recommendation to limit the simulations of T_{BTOA} to the cases of clear sky only, particularly at Ku band. Assuming this limitation, the contribution of the atmospheric module to the simulation error can be computed in Ku band by assuming an rms error on τ in the order of 0.003 np (0.013 dB) and an rms error on T_{mr} in the order of 1.6 K. This figures are basically originated by the analysis of variability shown in fig 3.2.7 and are conservative compared to the uncertainties derived using different computation approaches in fig. 3.6.2. We have used the simplified relationship (3.2.1) with $T_{mr\_up}=T_{mr\_dn}$ and we have generated samples of τ and T_{mr} varying randomly around their mean value with the above considered rms. Than the resulting standard deviation of T_{BTOA} has been computed for different geographical areas (mean values are taken from Fig. 3.2.4, 3.2.5 and 3.2.6) and background

emissivity (e=0.4 and 0.9) leading to the results of Table 3.4.X. No substantial errors (less than 1 K) are expected at S band, according to the amount of climatological variability depicted in Table 3.2.II.

TABLE 3.4.X KU BAND T_{BTOA} STANDARD DEVIATION ASSUMING AN RMS ERROR OF 0.003 FOR τ AND 1.6 FOR T_{mr}

	τ [np] at Θ=51°	T_{mr}	ΔT_{BTOA} [K] (e_s =0.4)	ΔT_{BTOA} [K] (e_s =0.9)
Low latitude	0.045	279	0.93	0.16
Middle latitude	0.037	267	0.88	0.13
High latitude	0.029	253	0.83	0.08

4 SEA MODEL

4.1 Introduction

The development of a microwave model of sea surface can either support the implementation of algorithms to retrieve sea and atmospheric parameters (e.g., salinity, surface wind speed and temperature), or, as in this work, be useful for the calibration of new sensors. The microwave emission from the ocean depends on surface roughness. A calm sea surface is characterized by highly polarized emission (Tsang et al., 1985; Ulaby and Elachi, 1992; Yueh and Kwok, 1993). When the surface becomes rough, the emission increases and becomes less polarized (Dzura et al., 1994; Yueh et al., 1995). This emission increasing is mainly due to:

i) polarization mixing caused by tilting of the local incidence angle associated to surface waves having wavelengths long compared to the observation microwave frequency (large-scale roughness, i.e. gravity sea waves) whose parameterization is done in terms of root mean square (rms) slope;
ii) sea foam made by mixture of air and saline water, increasing both polarization components of emission (foam coverage) whose parameterization is done in terms of fractional foam coverage;
iii) diffraction of microwaves by surface waves that are small compared to the observation wavelength, generated basically by moderate winds (small-scales waves, i.e. capillary sea waves) whose parameterization is done in terms of rms height slope.

In the last decade, several investigators have demonstrated the suitability of microwave radiometry for ocean remote sensing. In particular, surface wind speed estimations have been successfully performed by using the polarization diversity of the Special Sensor Microwave Imager (SSM/I) aboard the Defense Meteorological Space Program (DMSP) near-polar orbiting platforms. It has been shown that microwave radiometric measurements are sensitive to wind direction too (Veysoglou et al., 1991; Yueh et al., 1988; Johnson et al., 1993). Airborne campaigns and analyses of SSM/I measurements have indicated that ocean brightness temperatures can vary over azimuth angles relative to the wind direction by a few degrees Kelvin. These experimental evidences have led to the development of various models of polarimetric emission from the ocean surface, based on different approximations: from the simplified one-dimensional periodic case to the more realistic random two-dimensional model based on the small perturbation approach (Yueh et al., 1994a,b; Johnson et al., 1994).

In this work, we have selected the two-scale model which accounts for both emission and scattering from an anisotropic surface in a fairly accurate way (Yueh et al., 1994; Yueh, 1997; Lemaire et al., 1999). It includes also the effect of the foam and it requires, as inputs, the surface wind speed and the water temperature (together with the sea salinity for predicting emission below 5 GHz). Such data can be obtained from meteorological analyses as well as from satellite sensors (infrared radiometers, wind scatterometers) and climatological studies. A version of this model, which considers also the atmospheric effects, has been developed within a previous ESA contract (Pampaloni et al., 1996; Pierdicca et al., 2000).

In the beginning of this section, the characteristics two scale model are described. Then, a sensitivity analysis to the main sea parameters is illustrated. Since the software which implements the whole forward model (e.g., sea plus atmosphere) requires a lot of computation time, a crucial point of this work have consisted of developing a set of model function able to reproduce, with sufficient accuracy, the behaviour of the two scale model. The procedure followed in order to derive these functions is shown in the central part of this section. Finally, a validation of the proposed approach is described, considering both the results obtained during phase 1 and those achieved in phase 2.

4.2 Description of the "two scale model" for sea emission

The two scale polarimetric model accounts for both small scale and large scale sea surface roughness. The wave number that separates the two roughness scales is function of the electromagnetic wavelength. If an electromagnetic wave incident upon the sea surface is considered, the reflected radiation is produced by the large scale component, whereas scattering is due to the small scale one. In other words, the large waves can be confused with plane patches whose dimensions extend as far as several electromagnetic wavelengths and the electromagnetic scattering is caused by the small scale capillary waves superimposed to every patch, since, in the microwaves band, the latter kind of waves verify the Bragg condition.

In the present paragraph, the polarimetric notation, in which every brightness temperature vector is proportional to the corresponding Stokes vector, has been adopted. The brightness temperature vector at the sea surface $\mathbf{TB}^{BOA}$ (BOA: Bottom Of Atmosphere) is given by the brightness temperature $\mathbf{TB}^{SEA}$ emerging from each patch, averaged over the probability density function (p.d.f.) $P(S_x,S_y)$ of the slopes of the patches (assuming a Gaussian p.d.f.), that is over the distribution of slopes S_x and S_y of the large waves:

$$\mathbf{TB}^{\mathrm{BOA}}(\theta,\varphi;0) = \int_{-\infty}^{+\infty} \mathrm{dS_y} \int_{-\infty}^{+\cot\theta} \mathbf{TB}^{\mathrm{SEA}}(1-\mathrm{S_x}\tan\theta)\mathrm{P}(\mathrm{S_x},\mathrm{S_y})\mathrm{dS_x} \tag{4.1}$$

In equation (4.1), Sx and Sy represent the slopes in the x (parallel to the surface wind) and y (normal to the wind) directions, while (θ,φ) indicates the observing direction.

$\mathbf{TB}^{\mathrm{SEA}}$ is determined by the small scale roughness induced by the wind stress, but it is influenced also by the formation of the foam, which tends to increase the emissivity. If F represents the fraction of the sea covered by foam (which depends on wind speed and frequency), $\mathbf{TB}^{\mathrm{SEA}}$ is expressed by:

$$\mathbf{TB}^{SEA}(\theta,\varphi) = (1-F)\mathbf{TB}^{ROUGH}(\theta,\varphi) + Fe_f T_s \begin{bmatrix}1\\1\\0\\0\end{bmatrix} + F(1-e_f)[T_{DN}(\theta,\varphi) + T_{COS}e^{-\tau}] \begin{bmatrix}1\\1\\0\\0\end{bmatrix} \tag{4.2}$$

where $\mathbf{TB}^{\mathrm{ROUGH}}$ is due to the rough surface without foam, T_S indicates the sea surface temperature, T_{DN} is the downwelling atmospheric brightness temperature, T_{COS} the cosmic contribution, τ the optical thickness and e_f represents the foam emissivity, assumed having a specular behaviour. Therefore the second term of the second member of equation (4.2) accounts for the foam emission, whereas the third term is due to T_{DN} reflected by the foam covered surface. In its turn $\mathbf{TB}^{\mathrm{ROUGH}}$ has a component which accounts for the surface emission and another one due to the brightness temperature T_{DN} scattered by the rough surface. Both the emitted and the scattered components of $\mathbf{TB}^{\mathrm{ROUGH}}$ are derived by integrating the bistatic scattering coefficients due to the small scale roughness and furnished by a second order perturbation theory which ensures energy conservation. In fact, the first order perturbation theory describes the energy which is scattered by roughness in non-specular direction. Since coherent reflection, described by the well-known Fresnel coefficients, does not account for scattering, the second order solution gives the correction that has to be subtracted to the coherent component to respect the energy conservation law. The backscattering coefficients are given by:

$$\gamma_{\alpha\beta\mu\nu}(\theta,\varphi;\theta_i,\varphi_i) = R\delta(\theta-\theta_i;\varphi-\varphi_i-\pi) + \gamma^{inc}_{\alpha\beta\mu\nu}(\theta,\varphi;\theta_i,\varphi_i) \tag{4.3}$$

In (4.3), R represents the coherent contribution corrected by the second order solution and γ^{inc} denotes the incoherent component furnished by the first order one. The subscripts α, β, μ, ν represent the polarization, while i denotes the incidence direction.

As for the Ocean wave spectrum, which is included both in the first and second order coefficients and in the variance of the p.d.f. of the slopes, we have used the expression given by Yueh et al. (1994b):

$$W(k,\varphi) = \frac{1}{2\pi k} S(k)\left[1 + c(1-e^{-sk^2})\cos 2\varphi\right] \tag{4.4}$$

where:

$$S(k) = a_0 k^{-3}\left(\frac{bku_*^2}{g+xk^2}\right)^{a\log_{10}(k/k_j)} \tag{4.5}$$

In (4.4) and (4.5) s, a_0, a, b, x are constants, u_* is the wind friction, g is gravity, k_j is a function of g and wind speed, and c is a function of wind speed and $S(k)$. The expressions of the these parameters can be found in Yueh et al. (1994b).

As mentioned, the incoherent component of the bistatic scattering coefficients, is a function of the spectrum W:

$$\gamma^{inc}_{\alpha\beta\mu\nu} = 4\pi k_0^2 \cos\theta k_{zi}^2 \left|k_1^2 - k_0^2\right|^2 F_{\alpha\beta}F^*_{\mu\nu}W(k_x - k_{xi}, k_y - k_{yi}) \tag{4.6}$$

k_0 and k_1 are the propagation constants of air and sea water, respectively, k_x, k_y e k_z are the components of the propagation vector of the scattered wave and k_{xi}, k_{yi} e k_{zi} are the components of the propagation vector of the incident wave. $F_{\alpha\beta}$ are the elements of the scattering matrix.

$\mathbf{TB}^{\mathrm{ROUGH}}$ can be written in the following manner:

$$\mathbf{TB}^{ROUGH}(\theta,\varphi) = \mathbf{e}_S(\theta,\varphi)T_S + \mathbf{TB}^S(\theta,\varphi) \tag{4.7}$$

where $\mathbf{e}_s$ is the emission polarimetric vector and $\mathbf{TB}^s$ represents the brightness temperature scattered by the rough surface. As for the former vector, according to the polarimetric Kirchoff law (Yueh and Kwok, 1993), it is expressed by:

$$\mathbf{e}_S(\theta,\varphi)T_S = T_S\left\{\begin{bmatrix}1\\1\\0\\0\end{bmatrix} - \frac{1}{4\pi}\int_0^{\pi/2}\sin\theta_i d\theta_i \int_0^{2\pi} d\varphi_i \begin{bmatrix}\gamma_{vvvv}(\theta,\varphi;\theta_i,\varphi_i)+\gamma_{vhvh}(\theta,\varphi;\theta_i,\varphi_i)\\ \gamma_{hhhh}(\theta,\varphi;\theta_i,\varphi_i)+\gamma_{hvhv}(\theta,\varphi;\theta_i,\varphi_i)\\ 2\,\mathrm{Re}[\gamma_{vhhh}(\theta,\varphi;\theta_i,\varphi_i)+\gamma_{vvhv}(\theta,\varphi;\theta_i,\varphi_i)]\\ 2\,\mathrm{Im}[\gamma_{vhhh}(\theta,\varphi;\theta_i,\varphi_i)+\gamma_{vvhv}(\theta,\varphi;\theta_i,\varphi_i)]\end{bmatrix}\right\} \tag{4.8}$$

$\mathbf{TB}^s$ is given by:

$$\mathbf{TB}^S(\theta,\varphi) = \int_0^{\pi/2}\frac{1}{4\pi}\sin\theta_i d\theta_i \int_0^{2\pi} d\varphi_i \left[T_{DN}(\theta,\varphi) + T_{COS}e^{-\tau}\right] \cdot \begin{bmatrix}\gamma_{vvvv}(\theta,\varphi;\theta_i,\varphi_i)+\gamma_{vhvh}(\theta,\varphi;\theta_i,\varphi_i)\\ \gamma_{hhhh}(\theta,\varphi;\theta_i,\varphi_i)+\gamma_{hvhv}(\theta,\varphi;\theta_i,\varphi_i)\\ 2\,\mathrm{Re}[\gamma_{vhhh}(\theta,\varphi;\theta_i,\varphi_i)+\gamma_{vvhv}(\theta,\varphi;\theta_i,\varphi_i)]\\ 2\,\mathrm{Im}[\gamma_{vhhh}(\theta,\varphi;\theta_i,\varphi_i)+\gamma_{vvhv}(\theta,\varphi;\theta_i,\varphi_i)]\end{bmatrix} \tag{4.9}$$

4.3 Sensitivity to main input and model parameters

As previously mentioned, the considered sea emissivity model needs, as inputs, different data concerning the sea state. Some of them (wind speed, sea surface temperature) have been obtained from meteorological analyses, other ones have been inferred either by adopting simple models derived from empirical studies (foam), or by acquiring information from climatological studies (salinity). In this section a sensitivity analysis to such parameters is illustrated. In the following, we will not use the polarimetric representation anymore, since, for our purposes, the first two components of the Stokes polarimetric vector (i.e., the brightness temperatures in vertical and horizontal polarization) are needed.

4.3.1 Sea water salinity

The sea water dielectric constant ε_{sea}, is strongly influenced by salinity and surface temperature. Different relationships between these parameters are available in the literature, generally of polynomial kind. In this work we have adopted that given by Klein and Swift (1977), even though the one proposed by Ellison et al. (1996) has been also tested, as will be shown in Par. 4.3. We have performed a sensitivity analysis of the TB^{BOA} furnished by the model, by taking into consideration the two RA-2 frequencies. Such analysis is shown in Fig. 4.1.

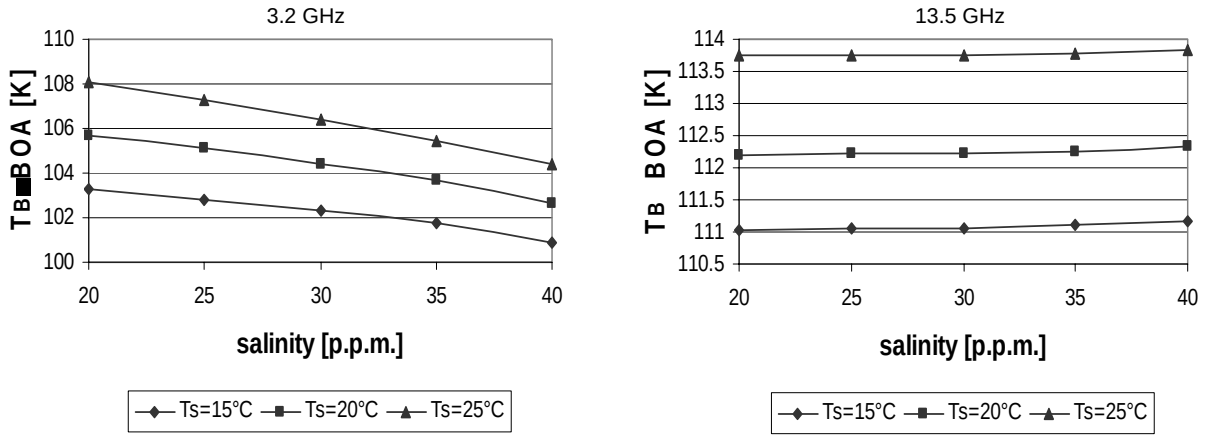

Fig. 4.1: Brightness temperature above the sea surface (TB^{BOA}) at 3 GHz (left panel) and 13 GHz (right panel) at nadir with respect to ocean salinity for the two scale model.

As apparent from previous figures, at 13.5 GHz the dependence on salinity is negligible (less than 0.5 K), while at 3.2 GHz the TB^{BOA} decreases of about 2 K when salinity decreases from 25 to 40 p.p.m..
For sake of simplicity we have decided to use a constant value for salinity and, in order to choose a reliable one, we have considered the climatological analysis reported in Fig. 4.2. It emerges that a value equal to 35 p.p.m. is suitable to represent the characteristics of salinity of the Oceanic areas.

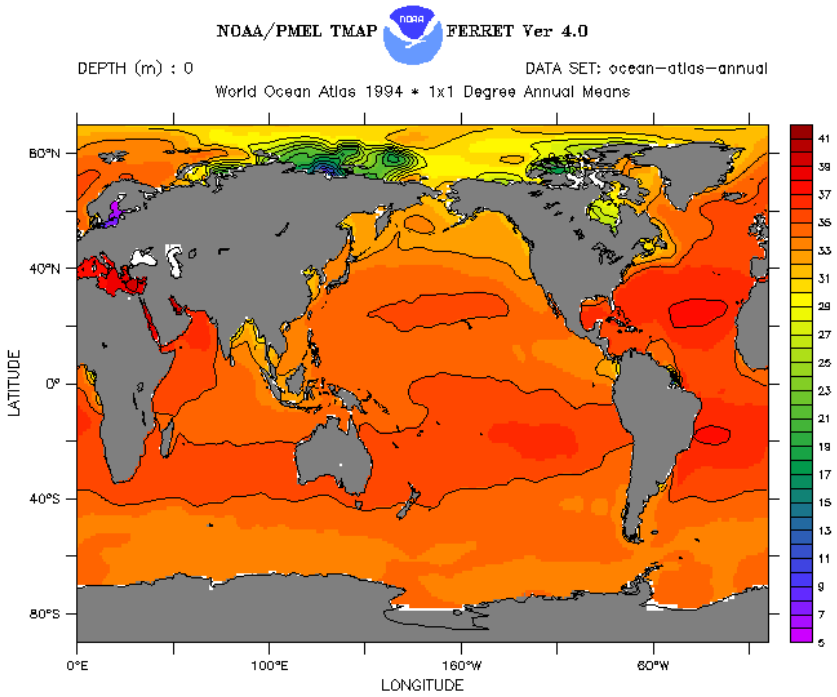

Fig. 4.2: Climatology of ocean salinity: annual mean values (year 1994).

4.3.2 Foam modeling impact

The contribution of foam to the sea emissivity has been studied, in the past, by various investigators. In this work, we have considered two models: the first one developed by Pandey and Kakar (1982) and the other proposed by Wilheit (1979).

The Pandey-Kakar model is described by the following equations

$$F = x_0 + x_1 WS + x_2 WS^2 \tag{4.10}$$

$$\begin{cases} x_0 = 1.707 \cdot 10^{-2} + 8.56 \cdot 10^{-4} f + 1.12 \cdot 10^{-5} f^2 \\ x_1 = -1.501 \cdot 10^{-2} + 1.821 \cdot 10^{-3} f - 4.634 \cdot 10^{-5} f^2 \\ x_2 = 2.442 \cdot 10^{-4} - 2.282 \cdot 10^{-6} f + 4.194 \cdot 10^{-7} f^2 \end{cases} \tag{4.11}$$

$$\begin{aligned} \varepsilon_{fh} &= 0.005 f + \frac{208 + 1.29 f}{T_S}(1 - 1.748 \cdot 10^{-3}\theta - 7.336 \cdot 10^{-5}\theta^2 + 1.044 \cdot 10^{-7}\theta^3) \\ \varepsilon_{fv} &= 0.005 f + \frac{208 + 1.29 f}{T_S}(1 - 9.946 \cdot 10^{-4}\theta + 3.218 \cdot 10^{-5}\theta^2 - 1.187 \cdot 10^{-6}\theta^3 + +7.0 \cdot 10^{-20}\theta^{10}) \end{aligned} \tag{4.12}$$

where F is the foam fraction, WS represents wind speed at 19.5 m above sea surface, f denotes frequency in GHz, θ is the observation angle and ε_{fh} and ε_{fv} are the emissivities in horizontal and vertical polarization, respectively. Fig. 4.3 illustrates the variation of F as a function of WS for various frequencies. It can be noticed that, for low frequencies, F becomes negative and that, at 3 GHz, F decreases with the increase of WS.

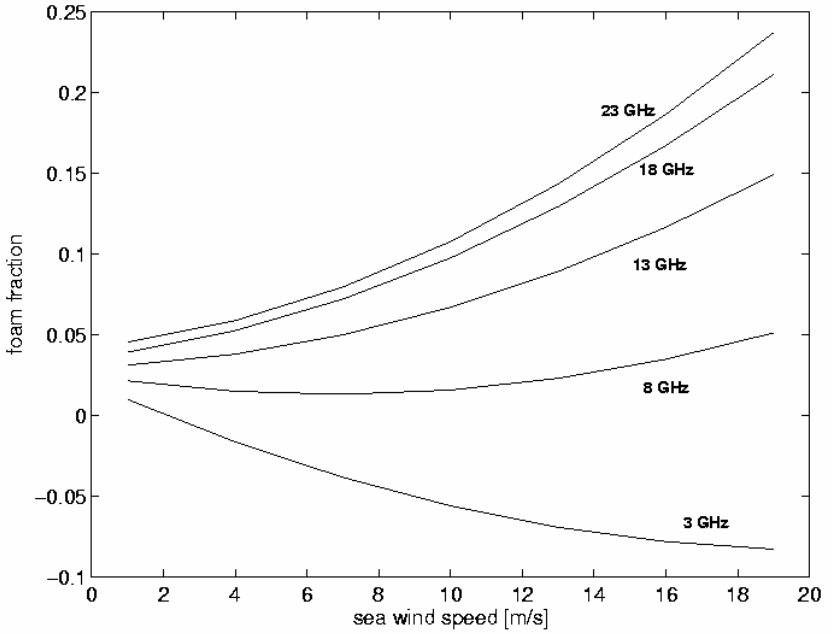

Fig. 4.3: Foam fraction as a function of wind speed according the model of Pandey and Kakar.

The anomalous behaviour shown in Fig. 4.3 has led us to consider the model developed by Wilheit in which F increases in a linear way with WS if the latter is greater than 7 m/s, otherwise F is equal to zero. The relationship that describes the Wilheit model is:

$$F = \begin{cases} 0.006 \cdot (1 - \exp(-f/7.5)) \cdot (WS - 7.) & \text{for } WS > 7 \text{ m/s} \\ 0 & \text{for } WS \le 7 \text{ m/s} \end{cases} \tag{4.13}$$

Foam fraction as a function of wind speed for the same frequencies considered in Fig. 4.3, according to the Wilheit model is reported in Fig. 4.4.

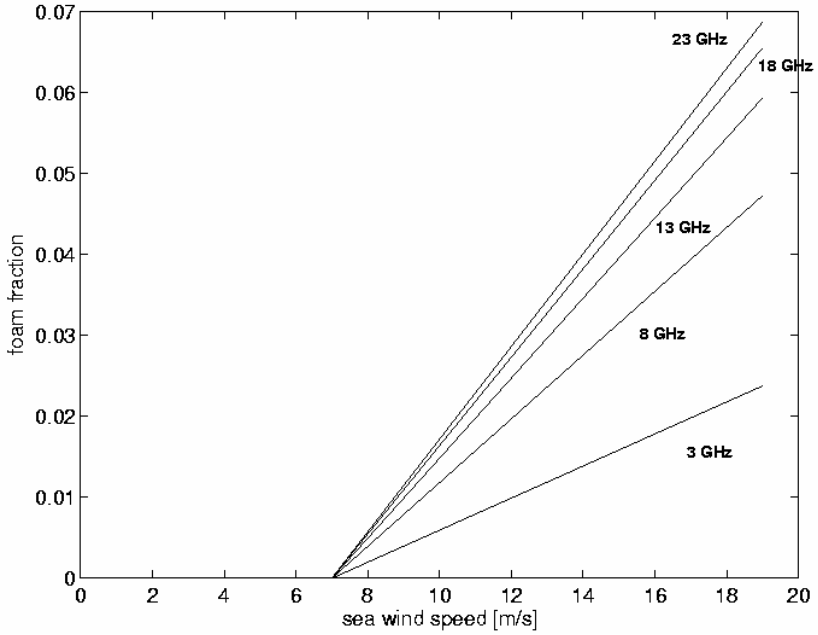

Fig. 4.4: Foam fraction as a function of wind speed according the model of Wilheit.

As for the emissivity, Wilheit assumes that the foam behaves as a black body. An emissivity which does not depend on neither polarization nor observation angle appears a too simple approximation. Therefore we have chosen to adopt a sort of mixed model for foam characterized the Wilheit expression for F and by the Pandey-Kakar one for emissivity.

Fig. 4.5 and Fig 4.6 compare the variation of the sea emissivities with wind speed, furnished by the two scale model, by considering the Pandey-Kakar relationships for both foam fraction and emissivity with those obtained by the Wilheit one for F. The former figure concerns Ku band with observation at nadir and a surface temperature equal to 15 °C. The latter one is referred to 19 GHz at horizontal polarization, observation angle of 53.1° and a surface temperature equal to 15 °C. It can be observed that the use of Wilheit foam fraction implies the decrease of the emissivity.

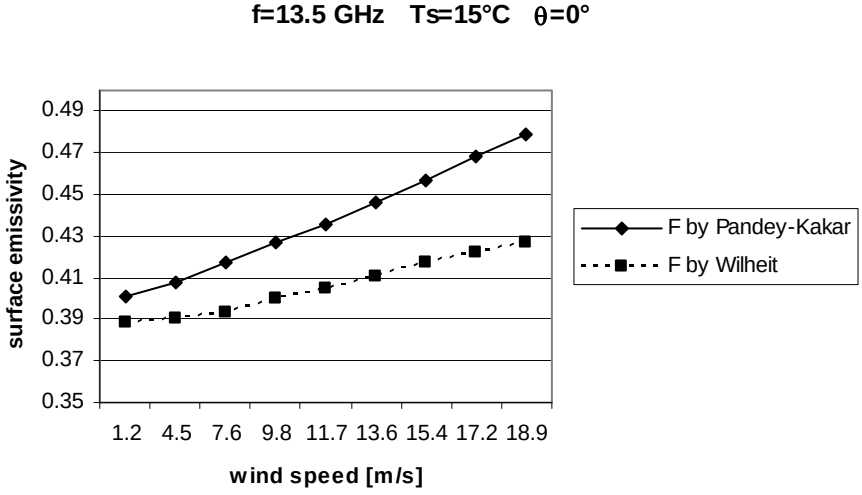

Fig. 4.5: Comparison between surface emissivities obtained by using Pandey-Kakar and Wilheit foam fraction, for 13.5 GHz and at nadir.

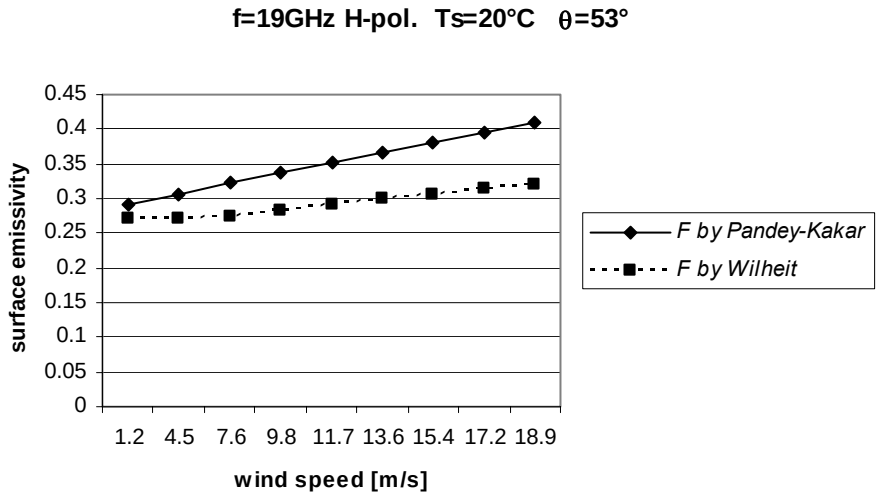

Fig. 4.6: Comparison between surface emissivities obtained by using Pandey-Kakar and Wilheit foam fraction, for 19 GHz, horizontal polarization and a observation angle of 53°.

4.3.3 ECMWF sea surface data

The information about the meteorological condition of the surface and of the atmosphere has been obtained from the ECMWF analyses described in section 2. In particular, for the purpose of simulating the brightness temperature observed by a spaceborne radiometer over a sea surface, the radiative parameters, derived from ECMWF data as it has been described in section 3 and the data concerning wind speed and surface temperature have been used.

In order to infer the importance of a correct evaluation of the surface parameters to achieve accurate simulations, a sensitivity analysis to wind speed (WS) and sea surface temperature (T_S) is presented. Fig. 4.7 illustrates the sensitivity to WS for two values of T_S and for the RA-2 bands. Fig. 4.8 and Fig. 4.9 show the same analysis for 10, 19 and 37 GHz for vertical and horizontal polarization, respectively. In the first case an observation angle of 0° have been assumed, whilst, in Fig. 4.8 and Fig. 4.9, θ is equal to 53° (the SSM/I observation angle).

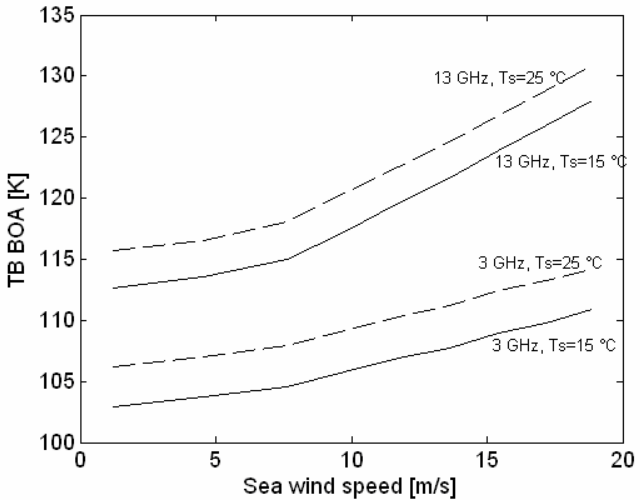

Fig. 4.7: Brightness temperature above the sea surface (TB^{BOA}) versus sea wind speed for S and Ku bands and at nadir. Sea surface temperatures equal to 15 °C (solid lines) and 25 °C (dashed lines) are considered.

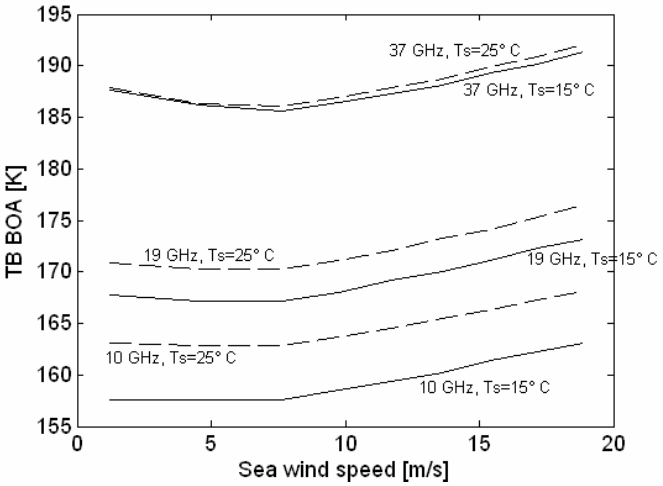

Fig. 4.8: Brightness temperature above the sea surface (TB^{BOA}) versus sea wind speed for 10, 19 and 37 GHz in vertical polarization and with an observation angle equal to 53°. Sea surface temperatures equal to 15 °C (solid lines) and 25 °C (dashed lines) are considered.

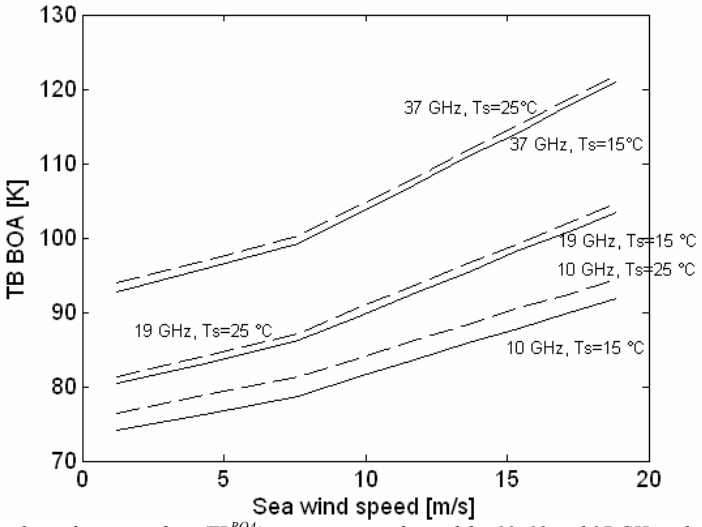

Fig. 4.9: Brightness temperature above the sea surface (TB^{BOA}) versus sea wind speed for 10, 19 and 37 GHz in horizontal polarization and with an observation angle equal to 53°. Sea surface temperatures equal to 15 °C (solid lines) and 25 °C (dashed lines) are considered..

For all the cases considered in the previous figures, the sensitivity to wind speed is very high and the increase, above the threshold of 7 m/s implied in the Wilheit model of foam is evident, thus confirming the effect of the latter on the sea surface emissivity. Moreover, for an observation at 53°, the influence of *WS* on the simulated TB^{BOA} is stronger at horizontal polarization.

As for the effect of the temperature, it becomes less important with the increase of the frequency. Nevertheless, at RA-2 bands, its correct estimate is fundamental. This is confirmed by the sensitivity analysis reported in Fig. 4.10, in which two values of wind speed are considered.

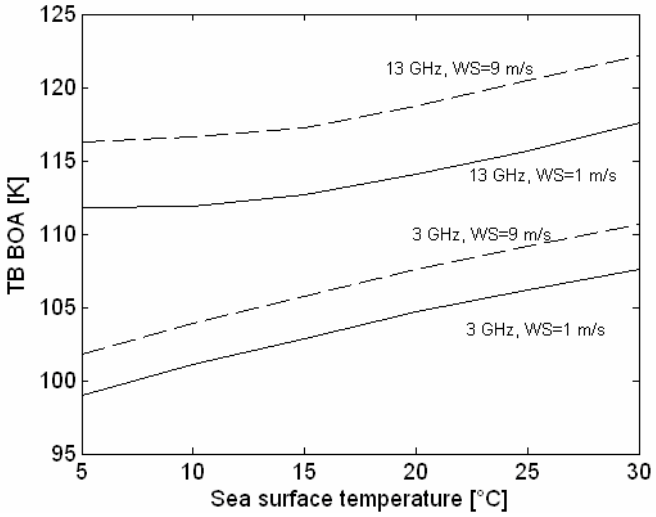

Fig. 4.10: Brightness temperature above the sea surface (TB^{BOA}) versus sea surface temperature for S and Ku band and at nadir. Sea wind speeds equal to 1 m/s (solid lines) and 9 m/s (dashed lines) are considered.

4.4 Development of microwave sea emissivity model functions

As opposed to semi-empirical models, which are calibrated for a specific instrument, the polarimetric (two-scale) one can be adopted for different frequencies and observation angles. Moreover, it is based on a rigorous theoretical treatment of the problem of the scattering from rough surfaces. Such rigorous approach implies, as a drawback, that the software which implements the model, developed, as previously mentioned, within a previous ESA contract (Pampaloni et al., 1996; Pierdicca et al., 2000), requires a large computation time (e.g., 20 minutes/run with a 1.4 GHz processor). In order to overcome this problem, we can resort to a "Model Function (MF)" approach. That is, from the sensitivity analyses of the polarimetric model, we can derive a model function of the emissivity (e_S), for a fixed frequency f_0, polarization p_0 and observation angle θ_0, as a function of sea surface temperature and wind speed:

$$e_S = \mathrm{MF}\ (T_S,\ WS;\ f=f_0,\ \theta=\theta_0,\ p=p_0,\ \varphi=45°) \tag{4.14}$$

For seek of simplicity, the azimuth angle φ has been assumed constant and equal to 45°, since the dependence of the brightness temperature to this angle is very weak, as it can be deduced by observing Tab. 4.1, in which all the outputs of the polarimetric model (the four Stokes parameters) with different values of φ are reported. In such table, S band is considered with θ equal to 0°.

Azimut angle [deg]	T_h [K]	T_v [K]	U [K]	V [K]
0	106.21	106.56	0	0
30	106.3	106.47	-0.3	0
45	106.38	106.38	-0.35	0
60	106.47	106.3	-0.3	0
90	106.56	106.21	0	0

Tab. 4.1: Outputs of the two scale polarimetric model for azimuth angle varying from 0° to 90°.

We have considered SSM/I, TMI, Topex/Poseidon TMR and RA-2 frequencies, with observation angles θ_0 equal to 53° for both SSM/I and TMI and 0° for RA-2 and TMR.

The model functions consist of 2nd order polynomial regressions on wind velocity WS and surface temperature T_S. They have the following general form:

$$e_S = a_0 + a_1\, WS + a_2\, WS^2 + a_3 Ts + a_4 T_S^2 \tag{4.15}$$

For the RA-2 bands we have obtained the following values:

3.2 GHz: $a_0 = 0.357487$; $a_1 = 0.00299100$; $a_2 = 0.000112769$; $a_3 = 0.000150439$; $a_4 = -3.87873 \cdot 10^{-7}$

13.5 GHz: $a_0 = 0.419011$; $a_1 = 0.00102212$; $a_2 = 0.000178503$; $a_3 = -0.00152531$; $a_4 = 2.0149510^{-5}$

In Fig. 4.11, for the purpose of assessing the validity of the model function approach, a comparison between the variation with sea wind speed of the emissivity computed with the two scale model and with the model function (MF) approach is presented, for 19 GHz in vertical polarization. A very good agreement can be observed.

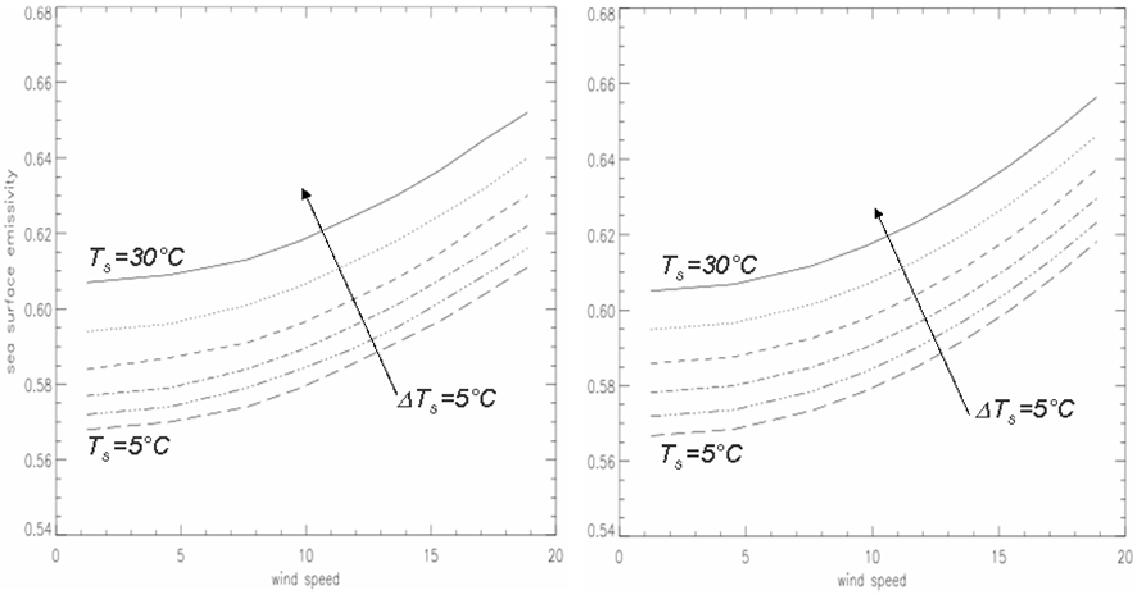

Fig. 4.11: Variation of sea surface emissivity with wind speed for the two scale model (right panel) and the model function approach (left panel) at 19 GHz, in vertical polarization and at 53°.

In our procedure of development of the model functions (MF's), the spectrum cut-off wave-number k_d , which separates the two roughness scales, has been parameterized with respect to the frequency, obtaining the values reported in Tab. 4.2:

Frequency [GHz]	k_d **[m^{-1}]**
3.2	26.5
10.6	60.0
13.5	71.5
19.3	96.0
22.3	120.0
37.0	270.0

Tab. 4.2: Spectrum cut-off wave-number for different frequencies.

In order to simulate the brightness temperature at the top of the atmosphere, given a value of e_S, we have assumed a simplified context, in which atmospheric scattering processes are negligible. With such assumption the TB^{TOA}, for a fixed frequency, polarization, and observation angle is given by:

$$TB^{TOA}(f=f_0, \theta=\theta_0, p=p_0) = e_S T_S e^{-\tau} + T_{mrDN}(1-e^{-\tau})(1-e_S) e^{-\tau} + T_{mrUP}(1-e^{-\tau}) \quad (4.16)$$

where τ is the optical thickness and T_{mrDN} and T_{mrUP} represent the mean radiative temperatures downwelling and upwelling, respectively.

4.5 Comparison with literature models

Many literature models of sea surface are calibrated against experimental results for a large set of satellite measurements. Therefore, a comparison of the behaviour of the two scale model with that presented by the empirical

ones can represent a first step of the validation of our approach. Moreover, for the S band, experimental data are not available, so that the comparison with an empirical model is the only way to test our procedure.

4.5.1 S band model

The considered S band model has been developed by Trokhimovski et al. (1995). It is based on a set of measurements collected throughout the period 1985-1989 by a radiometer operating at 3.76 GHz on board of an aircraft, which flied over the Pacific Ocean and the Barents Sea at an altitude of 200 m. The aircraft carried a wind scatterometer as well. The expression proposed by the authors gives the brightness temperature above the sea surface as a function of wind velocity at 19.5 m and of the azimuth angle:

$$T_B^{BOA} = \begin{cases} T_{B0} + 0.67 \cdot WS^{0.84}(1 + 0.0023\cos 2\varphi) & WS < 12 m/s \\ T_{B0} + 0.67 \cdot WS^{0.84} + (-2 + 0.18 \cdot WS) \cdot \cos 2\varphi & WS \geq 12 m/s \end{cases} \quad (4.17)$$

where T_{B0} is the T_B^{BOA} obtained by considering the sea as a smooth surface (i.e., in absence of wind). Equation (4.17) includes the effects of foam and both capillary and gravity waves.

A comparison between the sensitivity to wind speed presented by the T_B^{BOA} given by the Trokhimovski model and that furnished by the MF developed for 3.2 GHz is illustrated in Fig. 4.12 for an azimuth angle of 45° and a surface temperature of 20 °C. It can be observed that the two scale model is able to reproduce the behaviour of the empirical one with a maximum difference is less than 2 K. This can be considered a very encouraging result in the context of the passive calibration of the RA-2 instrument

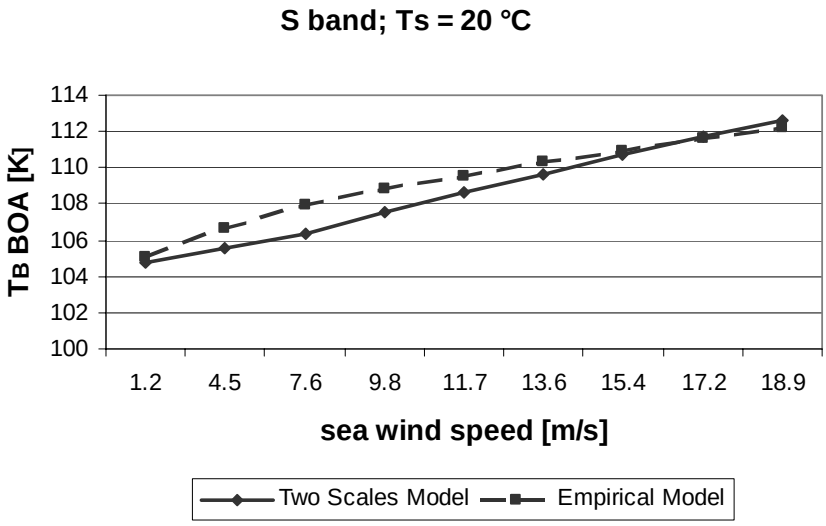

Fig. 4.12: Brightness temperature above the sea surface (T_B^{BOA}) against wind speed at S band for the polarimetric model and for that proposed by Trokhimovski et al., (1995).

4.5.2 Wentz model

Semi-empirical models developed for microwave scanning radiometers presently operating have been also taken into consideration. In the framework of the development of an algorithm for retrieving sea wind speed from SSM/I measurements, Wentz (1992) proposed the following formula for surface emissivity for the five low resolution SSM/I channels:

$$e_S = e_{Fresn} + \Delta E + \beta WS(\theta - 49°) \quad (4.18)$$

In equation (4.18) e_{Fresn} is the specular surface emissivity, ΔE is change due to sea-surface roughness and foam, i.e. the wind-induced emissivity (depending, at the end, on T_S and θ) and the third term models the incidence angle variation of ΔE with coefficient β given in the paper. The specular emissivity is given by:

$$e_{Fresn} = (s_0 + s_1 T_S + s_2 T_S^2 + s_3 T_S^3) / T_S \quad (4.19)$$

ΔE has the following expression:

$$\Delta E = m_1 WS \qquad WS \leq 7\text{m/s} \tag{4.20a}$$

$$\Delta E = m_1 WS + (m_2 - m_1)(WS^2 - 7) \qquad 7 \leq WS \leq 17\text{m/} \tag{4.20b}$$

$$\Delta E = m_2 WS + V_b(m_2 - m_1) \qquad WS > 17 \text{ m/s} \tag{4.20c}$$

$m_1, m_2, V_b, s_0, s_1, s_2, s_3$ are coefficients whose values are reported by Wentz (1992).

A regression technique, based on simple models and measured data, has been also developed for the Advanced Microwave Scanning Radiometer (AMSR) to estimate sea emissivity (Wentz and Meissner, 1999). This instrument operates also at 10.6 GHz as well as the spaceborne TRMM Microwave Imager (TMI), even though the ground resolution of TMI is almost half of AMSR one. The emissivity model resort the Geometrical Optics solution to compute the ocean reflectivity R_{geo} for varying angle and salinity. These numerical results are used to fit the modelled surface reflectivity (and the complementary emissivity), given by:

$$R_S = 1 - e_S = (1 - F)\, R_{clr} + F\, k \tag{4.21}$$

where F is the foam fraction and R_{clr} is the reflectivity of the rough surface clear of foam. The latter is related to R_{geo}:

$$R_{clr} = (1 - \beta)\, R_{geo} \tag{4.22}$$

By substituting (4.22) in (4.21), R_S can be expressed as:

$$R_S = (1 - \Phi_{reg})\, R_{geo} \tag{4.23}$$

The factor Φ_{reg} is calculated as:

$$\Phi_{\text{reg}} = F + \beta - F\beta - F\, k + F\, k\, \beta \tag{4.24}$$

In the model implementation Wentz and Meissner suggest to derive Φ_{reg} and R_{geo} from empirical data using regression model functions. The former is approximated by:

$$\Phi_{\text{reg}} = y_1\, WS \qquad \text{for } WS < WS_1 \tag{4.25a}$$

$$\Phi_{\text{reg}} = y_1\, WS + 0.5\,(y_2 - y_1)\,[WS - WS_1]^2 / (WS_2 - WS_1) \qquad \text{for } WS_1 < WS < WS_2 \tag{4.25b}$$

$$\Phi_{\text{reg}} = y_2\, WS + 0.5\,(y_2 - y_1)\,[WS_2 + WS_1] \qquad \text{for } WS > WS_2 \tag{4.25c}$$

being the regression coefficients available in Wentz and Meissner (1999) for AMSR channels. For the vertical polarization, WS_1 = 3 m/s and WS_2 = 12 m/s. For the horizontal polarization, WS_1 = 7 m/s and WS_2 = 12 m/s. The parameter R_{geo} can be derived from the following formula:

$$R_{geo} = R_O - [r_o + r_1\,(\theta - 53°) + r_1\,(T_S - 288) + r_1\,(\theta - 53°)\,(T_S - 288)]\, WS \tag{4.26}$$

Again, the regression coefficients are available in Wentz and Meissner (1999) for AMSR channels. The validity of (4.23) is limited to $0 < WS < 20$ m/s, $273 < T_S < 303$ K and $49° \leq \theta < 57°$.

The comparison between the emissivity obtained by adopting the Wentz approach and that furnished by our model functions is shown in Fig. 4.13. Such figure reveals that the polarimetric model tends to overestimate the results of the semi-empirical one at the lower frequencies, i.e. at 10 and 19 GHz, as the wind velocity increases. Moreover we have carried out a comparison between the two models for a case study: the SSM/I pass over Indian Ocean box (-17°–7° N, 87°-97° W) on April, 4 2000. The results are shown in Fig. 4.14, where it is reported a scatterplot of SSM/I measured TB's and simulated ones, obtained, by applying (4.16) to the emissivity values provided by the models. In this case the two behaviours are similar.

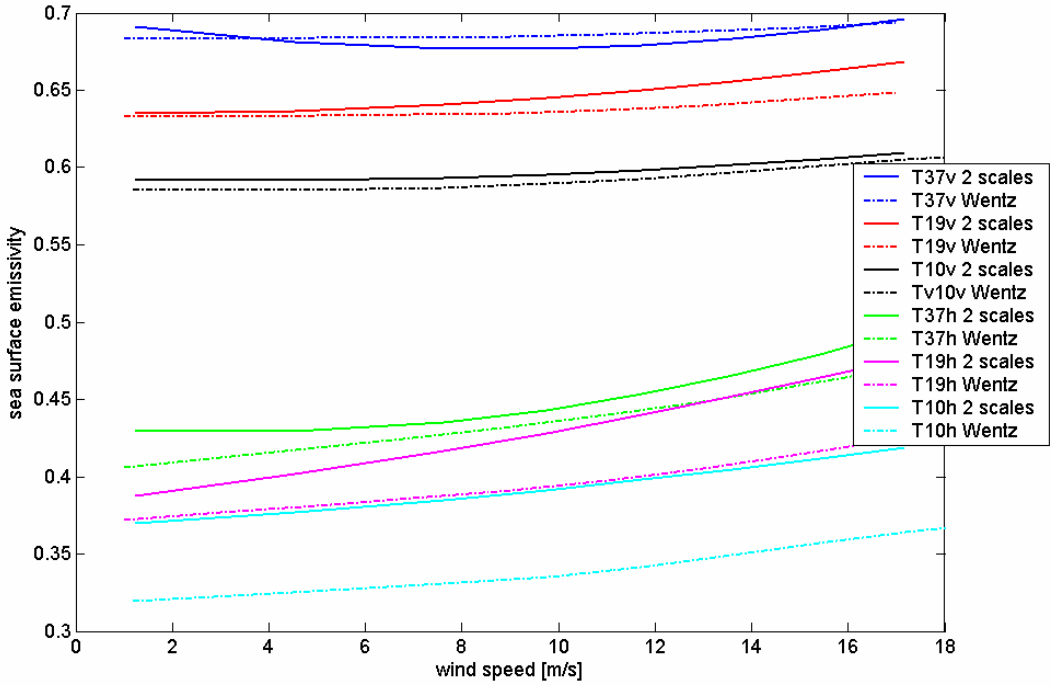

Fig. 4.13: emissivity at10, 19 and 37 GHz at 53° with respect to sea wind velocity for both two scale and Wentz models.

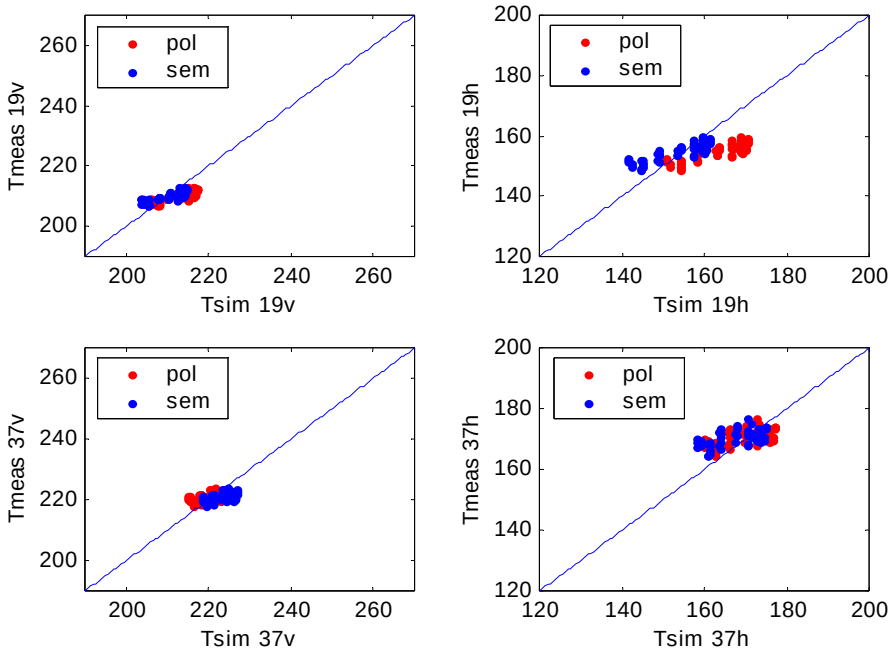

Fig. 4.14: Comparison between measured and simulated TB for both numerical (red points) and semi-empirical (blue points) model. All the values are in Kelvin

4.6 Validation and tuning

In order to assess the MF approach we have compared our simulations with the radiometric measurements belonging to a validation data set consisting of the SSM/I, TMI and TMR passes over the Oceanic calibration areas mentioned in section 2. In the following we will show results on a case study and on a statistical basis. Results achieved during phase 1 and phase 2 validation databases are considered separately.

4.6.1 Need of a clear-sky mask

Within the proposed procedure, the atmospheric parameters are derived from ECMWF vertical profiles using a radiative model, as depicted in section 3. An accurate estimation of these parameters, especially the optical thickness, is fundamental to obtain a fairly good estimate of the TB^{TOA}, as it can be seen in Fig. 4.15, which illustrates the sensitivity

of the simulated TB^{TOA} to the mean radiative temperature (assuming T_{mrDN} equal to T_{mrUP}) and to the optical thickness (indicated, in the figure, with tau). In this case we have considered Ku band, observation at nadir and a wind velocity equal to 8 m/s.

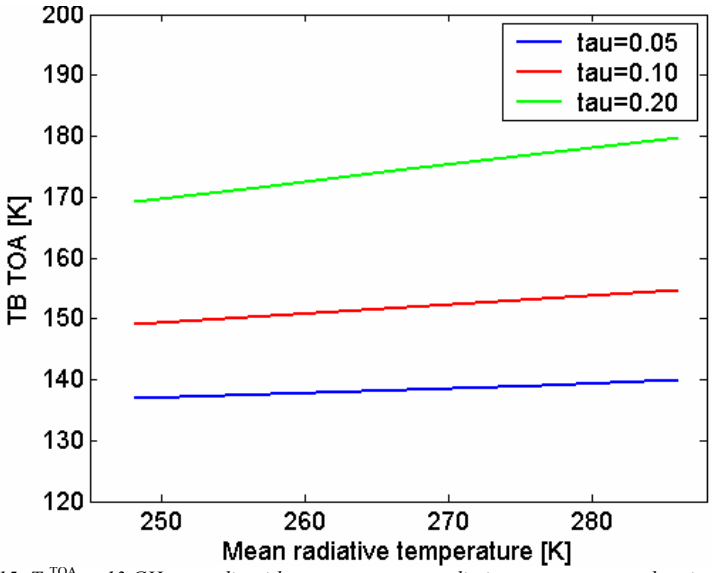

Fig.4.15: T_B^{TOA} at 13 GHz at nadir with respect to mean radiative temperature and optical thickness.

The high sensitivity, especially to the optical thickness, shown in Fig. 4.15, demonstrates that an accurate estimation of the radiative parameters is necessary to achieve simulations which reproduce accurately the radiometric measurements. In other words, if the state of the atmosphere foreseen by ECMWF is not the actual one when the satellite overpasses the selected geographical zone, discrepancies between simulated and real data may occur.

Fig. 4.16 presents a comparison between SSM/I measured and simulated TB's, for July 31, 2000, Indian Ocean box, using the model function (MF) approach for simulations. There are high values of TB's, measured by the radiometer, which are not matched by the simulations. This may indicate the presence of a cloud detected by the radiometers and not forecasted by ECMWF. To verify this hypothesis, in Fig. 4.17, a comparison between the SSM/I image (for the same case study) at 19 GHz in vertical polarization and the simulated one is illustrated. The optical thickness derived from ECMWF is also reported. It can be noticed that the simulated TB image reproduces the optical thickness one and that zones of measured high TB tend to be translated with respect to the areas of simulated high TB.

Fig.4.16: Comparison between SSM/I measured and MF simulated T_B for July 31, 2000, Indian Ocean box.

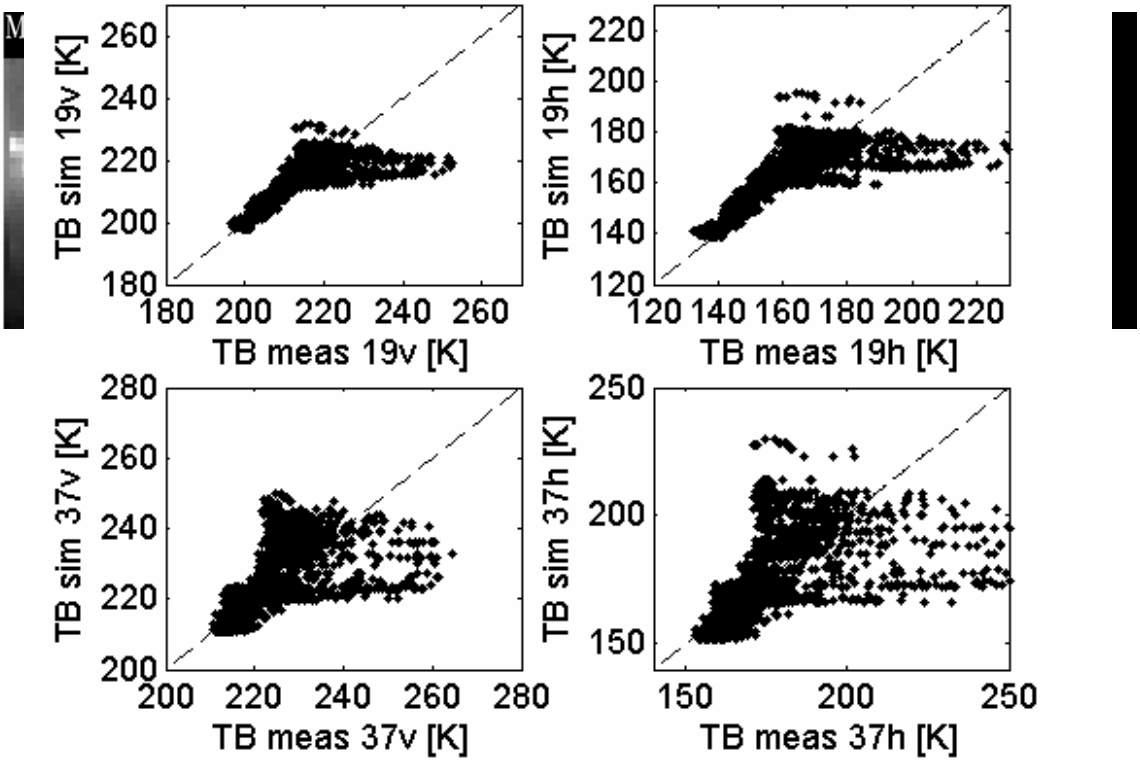

Fig.4. 17: Optical thickness (right panel), SSM/I measured (left panel) and simulated (central panel) T_B at 19 GHz in vertical polarization for July 31, 2000, Indian Ocean box.

For the purpose of avoiding cloud and rain atmospheric effects, we have imposed a clear-sky mask by using two thresholds: 0.003 cm on liquid water content and 5 K on the scattering index (Ferraro and Marks, 1995). In Fig. 4.18 it is shown the same scatterplot of Fig. 4.16, but with the application of the clear sky mask. The improvement of the correlation between TB measurements and simulations is evident.

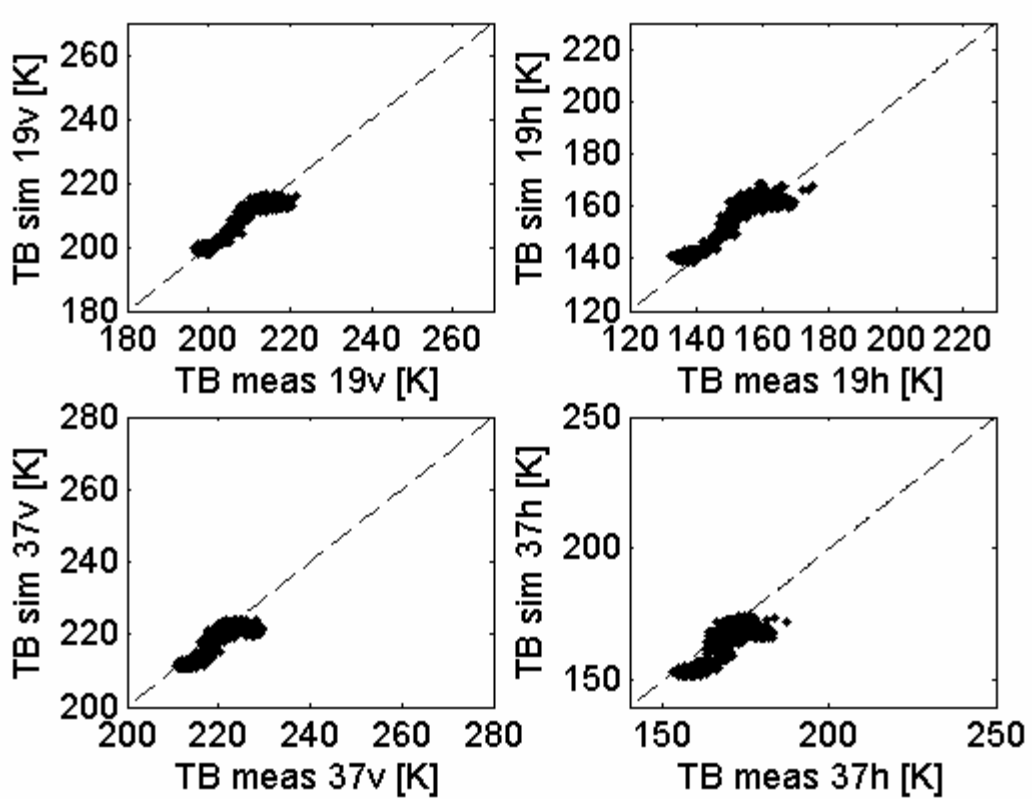

Fig.4.18: Comparison between SSM/I measured and MF simulated T_B at 19, 22 and 37 GHz for July 31, 2000, Indian Ocean box, with the application of the clear sky mask.

4.6.2 Phase 1 validation

The validation data set, considered throughout phase 1 consists of the SSM/I and TMI passes over

i) the Pacific Ocean box (July 23, 2000 and March 8, 2000);
ii) the passes over the North Atlantic box (March 7, 2000, April 5, 2000 and July 12, 2001);
iii) the South Atlantic pass on June 20, 2000;
iv) the passes over Indian Ocean box (April 11, 2000, June 21, 2000, July 31 2000 and August 23, 2000);

Moreover, the data provided by the TMR radiometer on board of Topex/Poseidon satellite have been also available over the North Atlantic box (March 7, 2000, April 5, 2000) and for the South Atlantic (June 20, 2000) and the Pacific (July 23, 2000) box.

As mentioned in section 4.3, the foam modeling can have an impact on results obtained from the physical polarimetric model. As a first step, we have compared the effect of the Pandey-Kakar and Wilheit foam fraction models on whole dataset. In Fig 4.19 it is illustrated the comparison between measured and simulated TB^{TOA} for the whole test data set, using the MF approach with Pandey-Kakar foam fraction model and applying the clear-sky mask. An overall fairly good correlation between measurements and simulation can be noted, but at 19 and 10 GHz in horizontal polarization there is an appreciable overestimation of measured brightness temperatures. Fig. 4.20 illustrates the same comparison between simulated and measured brightness temperatures for the whole test data set, but using the MF approach with the Wilheit foam fraction (and the clear-sky mask). It is apparent the improvement in the agreement between SSM/I and TMI data and simulations, for low frequencies. The results in terms of correlation coefficients, bias error (simulations minus measurements) and error standard deviation are described in Tab. 4.3 (Pandey-Kakar foam fraction) and Tab. 4.4 (Wilheit foam fraction).

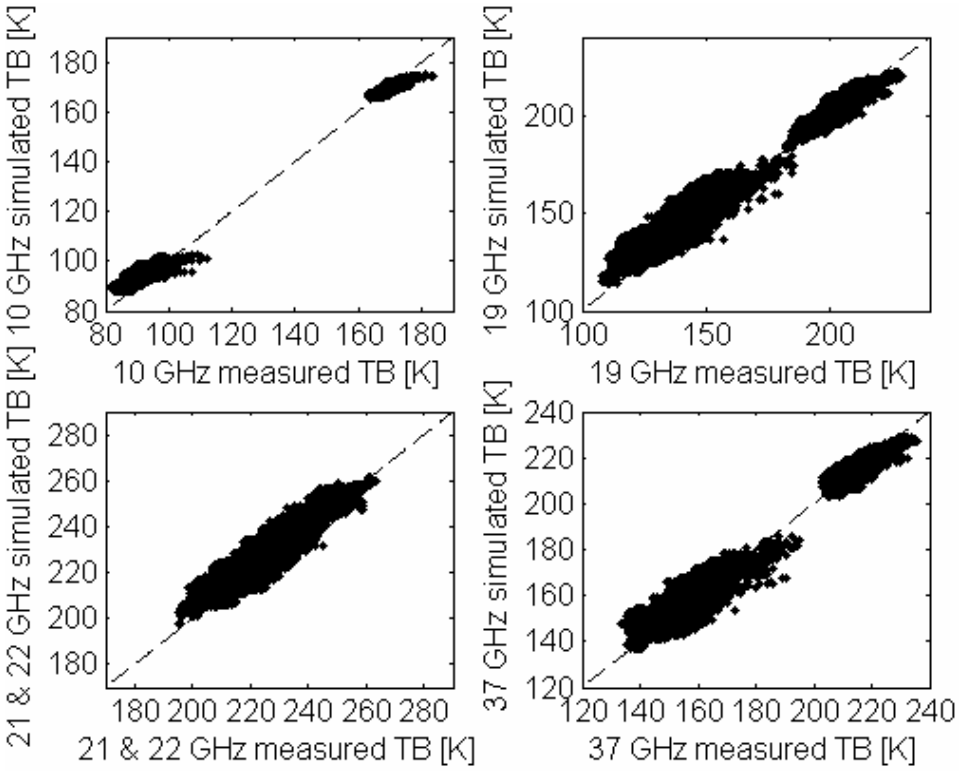

Fig.4.19: Comparison between measured and MF simulated T_B at 10, 19, 22 and 37 GHz for the phase 1 data set with the Pandey-Kakar foam fraction, using both SSM/I and TMI data belonging to the phase 1 validation set. A clear sky mask is applied. Horizontal and vertical polarizations are included in the same figure.

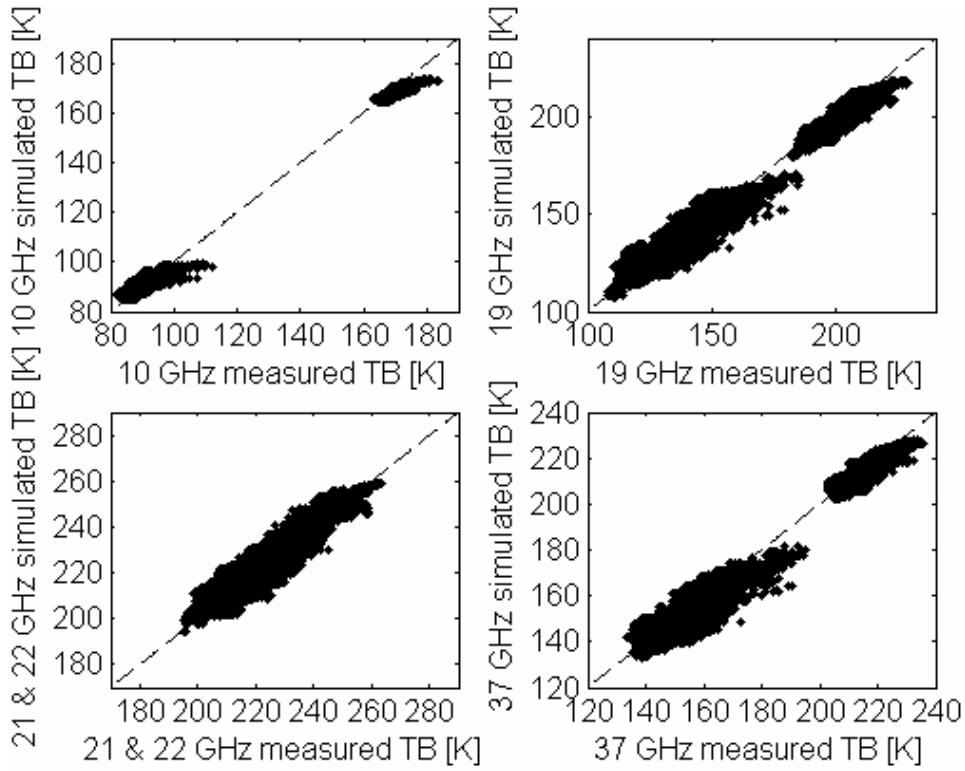

Fig.4.20: Comparison between measured and MF simulated T_B at 10, 19, 22 and 37 GHz for the phase 1 data set with the Wilheit foam fraction, using both SSM/I and TMI data belonging to the phase 1 validation set. A clear sky mask is applied. Horizontal and vertical polarizations are included in the same figure.

With respect to the comparison reported in Fig. 4.19, the one illustrated in Fig. 4.20 shows an evident decrease of the bias error for the 19 GHz in horizontal polarization channel and, especially, for the 10 GHz in horizontal polarization channel. Nevertheless, some points of mismatch between ECMWF atmospheric parameters and radiometric measurements are still present.

	TB 10 v	TB 10 h	TB 19 v	TB 19 h	TB 21/22 v	TB 37 v	TB 37 h
Correlation coefficient	0.930	0.843	0.915	0.899	0.931	0.852	0.873
Bias error [K]	0.480	4.366	2.239	7.643	3.942	1.234	2.516
Error standard deviation [K]	1.115	1.598	2.779	4.912	4.221	2.588	4.286

Tab. 4.3: Statistical analysis of the comparison between measurements and MF simulations with Pandey-Kakar foam fraction for the phase 1 dataset.

	TB 10 v	TB 10 h	TB 19 v	TB 19 h	TB 21/22 v	TB 37 v	TB 37 h
Correlation coefficient	0.956	0.905	0.941	0.934	0.954	0.898	0.911
Bias error [K]	-0.479	2.235	-0.929	0.898	1.294	0.383	-0.905
Error standard deviation [K]	1.073	1.352	2.708	4.551	4.042	2.562	4.154

Tab. 4.4: Statistical analysis of the comparison between measurements and MF simulations with Wilheit foam fraction for the phase 1 dataset.

The results of Tab. 4.4 can be compared with an alternative procedure, described in Par. 3.4, where the atmospheric radiation and opacity are estimated directly from remotely sensed data. The limitation of this technique is mainly due to the need of TB data collocated with those of the altimeter, as opposed to the procedure based on ECMWF data which is entirely based on 3-D output grid and radiative models. Fig. 4.21 shows the result of this alternative procedure, while Tab. 4.5 resumes the statistical analysis on the entire dataset. With respect to the comparison reported in Fig. 4.20, an appreciable increase of the correlation between measurements and simulations is noted, but as a drawback, the bias error increases. These aspects become evident by analyzing Tab. 4.5. Some correlations can reach values up to 99%. On the other hand, there is an increase of the bias error that cannot be neglected of the order of 2-3 K, much higher than that shown in Tab. 4.4. Since, for the calibration of RA-2 instrument, it is important to have as less bias as possible, the operational algorithm will be preferentially run by ingesting the atmospheric parameters derived from ECMWF vertical profiles.

	TB 10 v	TB 10 h	TB 19 v	TB 19 h	TB 21/22 v	TB 37 v	TB 37 h
Correlation coefficient	0.973	0.899	0.993	0.991	0.994	0.963	0.955
Bias error [K]	-3.639	-2.455	-3.119	-2.579	-0.946	-2.426	-6.394
Error standard deviation[K]	1.483	1.973	1.159	2.022	1.505	2.016	3.655

Tab. 4.5: Statistical analysis of the comparison between measurements and MF simulations (with Wilheit foam fraction) using TB data to estimate atmospheric radiation and opacity, instead of ECMWF ones.

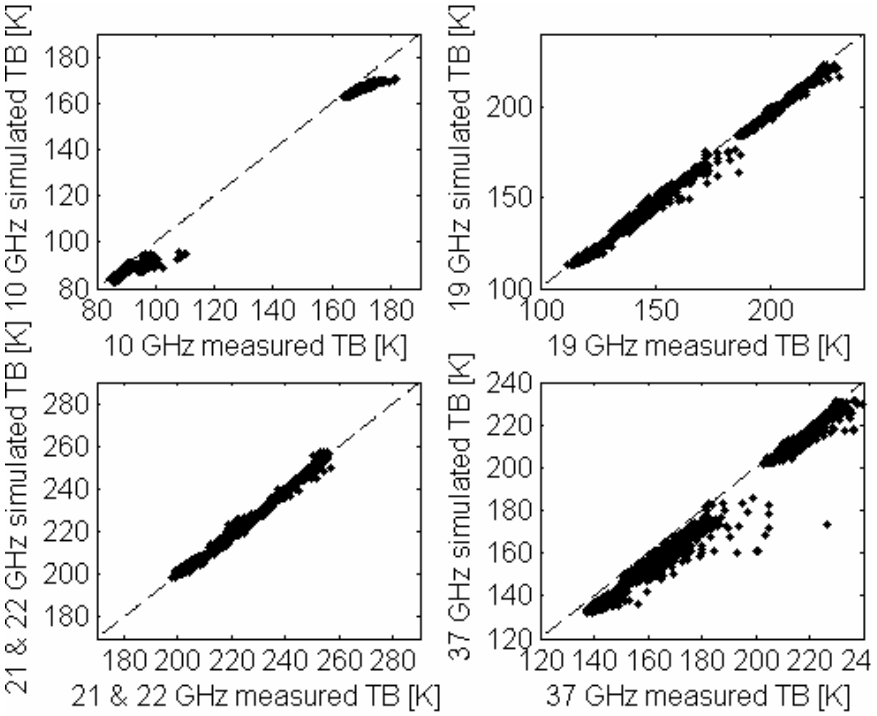

Fig.4.21: Comparison between measured and MF simulated T_B for the phase 1 dataset (with Wilheit foam fraction) and using T_B data to estimate atmospheric radiation and opacity, instead of ECMWF ones.

As a final application, we have considered radiometric data coming from the TMR radiometer mounted on the Topex/Poseidon platform. These measurements are useful since the radiometric observations are at nadir as well as the RA-2 instrument. The procedure followed is the same based on SSM/I and TMI data with the atmospheric parameters derived from ECMWF profiles.

As mentioned, we have only two sets of Topex/Poseidon radiometric observations for the North Atlantic box (March 7, 2000, April 5, 2000) and only one set both for the South Atlantic (June 20, 2000) and the Pacific (July 23, 2000) box. Moreover these sets consist of a limited number of usable data. We could not apply the scattering index due to the different frequency and viewing angle, so that the cloud mask has been implemented only using the liquid water content inferred from ECMWF data. The results of the comparison between measurements and simulations are shown in Fig. 4.22 and summarized in Tab. 4.6.

	TB 18	**TB 21**	**TB 37**
Correlation coefficient	0.875	0.925	0.725
Bias error [K]	-0.517	1.427	-2.216
Error standard deviation [K]	1.449	2.733	2.317

Tab. 4.6: Statistical analysis of the comparison between Topex/Poseidon measurements and MF simulations (with Wilheit foam fraction).

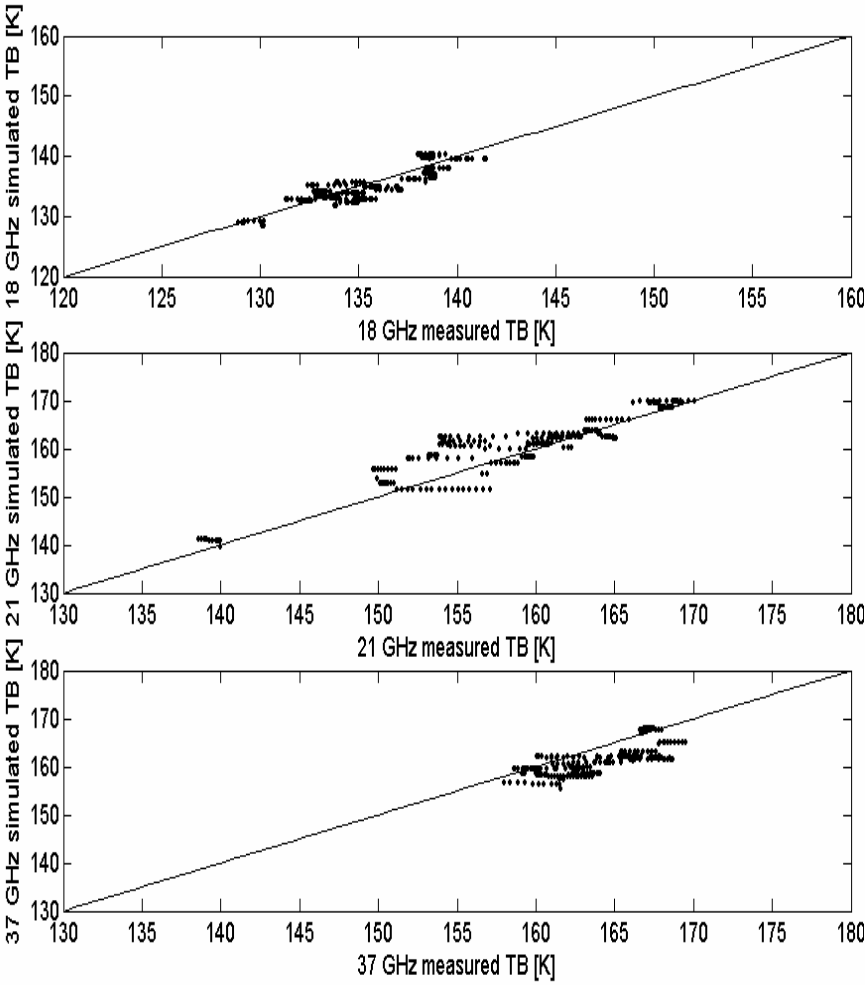

Fig.4.22: Comparison between Topex-Poseidon measured and MF simulated T_B.

Even though only few measurements were available, these results can be considered encouraging if compared with those obtained by other research groups (Obligis et al., 2001). At 18 GHz, which is the closest frequency to the RA-2 ones (3.2, 13.8 GHz), a sufficiently low bias and a reasonably good correlation can be observed. The bias error tends to increase with the increase of the frequency.

4.6.2 Phase 2 validation and final model setup

The validation set used in phase 2 consists of the SSM/I and TMI passes corresponding to RA-2 ones over the calibration areas. In particular, for each RA-2 overpass, the temporarily closest SSM/I and TMI images, as well as ECMWF analysis, have been identified. The considered overpasses are reported in Tab. 4.7. The comparison between measurements and the simulations carried out with the model function (MF) approach is shown in Fig. 4.23, while Tab. 4.8 illustrates the corresponding statistical analysis. The correlation sufficiently high for this test set, although it is less than 80% for the 37 GHz channels and for the 10 GHz one in horizontal polarization. This fact can be explained by taking into account that, since the available measurements are few, we have chosen to adopt a clear-sky mask less restrictive than the one used in phase 1. We have maintained the threshold of 5 K for the scattering index, but, for the seek of having a number of data large enough to derive statistics, the threshold for liquid water content has been fixed equal to 0.05 cm (instead of 0.003 cm). This explains also the remarkable increase of the error standard deviation for the higher frequencies.

The bias error is slightly greater than that obtained phase 1. It is worth noticing that in phase 1 we have selected SSM/I and TMI passes close in time to the meteorological analyses, whereas in phase 2 the temporal reference consists of the RA-2 acquisition times. Therefore remarkable temporal mismatches may occur between radiometric and ECMWF data. This is one of the causes of the bias increase with respect to phase 1.

North Atlantic		**South Atlantic**	**Indian Ocean**
Oct 02, 2002	Nov 15, 2002	Oct 05, 2002	Oct 17, 2002
Oct 04, 2002	Nov 23, 2002	Oct 07, 2002	Nov 21, 2002
Oct 06, 2002	Nov 25, 2002	Oct 10, 2002	Mar 06, 2003
Oct 10, 2002	Mar 09, 2003	Oct 11, 2002	
Oct 11, 2002		Oct 13, 2002	
Oct 19, 2002		Oct 14, 2002	
Oct 20, 2002		Oct 15, 2002	
Oct 21, 2002		Nov 11, 2002	
Nov 10, 2002		Mar 04, 2003	
Nov 14, 2002		Mar 18, 2003	

Tab. 4.7: Phase 2 validation data set.

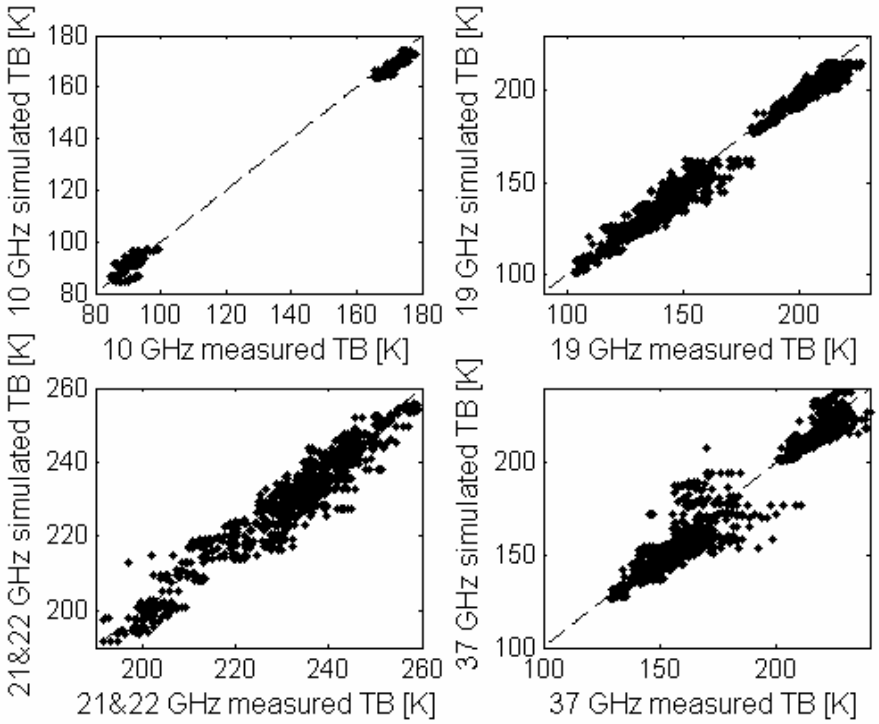

Fig.4.23: Comparison between measured and MF simulated T_B for the phase 2 dataset.

	TB 10 v	TB 10 h	TB 19 v	TB 19 h	TB 21/22 v	TB 37 v	TB 37 h
Correlation coefficient	0.887	0.723	0.949	0.938	0.966	0.795	0.773
Bias error [K]	-2.983	1.009	-3.593	-3.316	-1.809	-1.736	-2.841
Error standard deviation [K]	1.062	1.922	3.024	5.112	4.117	4.795	8.854

Tab. 4.8: Statistical analysis of the comparison between measurements and MF simulations for phase 2 test set.

As previously mentioned, we had included in the two scale model the expression developed by Klein and Swift (1977) for the sea water dielectric constant (ε_{sea}). In phase 2 we have tested the one proposed by Ellison et al (1996) for the purpose of verifying whether the adoption of a different model for ε_{sea} can improve the capability to reproduce the phase 2 satellite data. We have followed the same procedure described in the previous paragraphs (development of model functions) and the results obtained for the phase 2 validation set are reported in Tab. 4.9

	TB 10 v	TB 10 h	TB 19 v	TB 19 h	TB 21/22 v	TB 37 v	TB 37 h
Correlation coefficient	0.887	0.722	0.952	0.939	0.966	0.826	0.785
Bias error [K]	-1.342	2.094	-1.428	-1.889	-0.222	1.656	-0.411
Error standard deviation [K]	1.061	1.931	2.955	5.071	4.030	4.482	8.642

Tab. 4.9: Statistical analysis of the comparison between measurements and MF simulations, obtained by adopting the Ellison model for the sea water dielectric constant, for the phase 2 test set.

The correlation between measurements and simulations is substantially the same of Tab. 4.8, but the bias error has decreased (except for the 10 GH, horizontal polarization channel). Despite this achievement, if we use the Klein-Swift method for the phase 1 validation set, the results, reported in Tab. 4.10, are worse than those illustrated in Tab. 4.4. Moreover, the mean difference between the two groups of simulations, obtained by adopting the two different sea water permittivity models, for the RA-2 frequencies is less than 1 K at S band and less than 2 K in Ku band. Therefore we have decided to maintain the Klein-Swift expression in our final model.

	TB 10 v	TB 10 h	TB 19 v	TB 19 h	TB 21/22 v	TB 37 v	TB 37 h
Correlation coefficient	0.933	0.848	0.920	0.906	0.932	0.872	0.879
Bias error [K]	0.824	2.786	0.872	2.187	3.041	2.935	0.862
Error standard deviation [K]	1.076	1.569	2.684	4.710	4.185	2.392	4.197

Tab. 4.10: Statistical analysis of the comparison between measurements and MF simulations obtained by adopting the Ellison model for the sea water dielectric constant, for the phase 1 dataset.

For few of the RA-2 passes considered in phase 2, the data of the MWR radiometer aboard Envisat are available. Such sensor operates at 23.8 and 36.5 GHz with, 0° observation angle. Therefore we have developed two new model functions and the results of the comparison between the simulated TB^{TOA} and the MWR data are shown in Fig. 4.24 and statistically summarized in Tab. 4.11. The correlation is high, but at 36.5 GHz the error standard deviation is quite large (about 6 K). The bias is sufficiently low, and it is less at 23 GHz than at 36 GHz. This confirms the results that had emerged in the analysis performed when the Topex/Poseidon data had been considered: the ability of our model to reproduce radiometric data for a 0° viewing angle, increases with the decrease of frequency. This fact, assessed also by the comparison between our TB^{BOA} simulations and those provided by the empirical expression developed by Trokimovshy et al. (1995) for S band, allows us to conclude that, for the RA-2 frequencies, our sea surface microwave model is reliable and suitable for the passive calibration purposes.

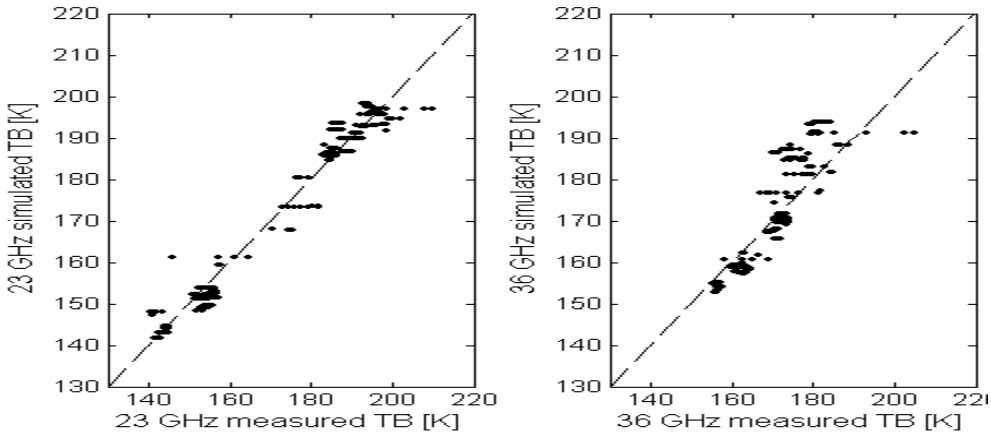

Fig.4.24: Comparison between Envisat MWR measured and MF simulated T_B for the phase 2 dataset..

	TB 23.8	**TB 36.5**
Correlation coefficient	0.984	0.911
Bias error [K]	-1.969	-2.105
Error standard deviation [K]	3.768	6.183

Tab. 4.11: Statistical analysis of the comparison between Topex/Poseidon measurements and MF simulations (with Wilheit foam fraction).

4.6.3 Estimate accuracy of simulated brightness at Ku and S band

In order to foresee an error budget for our simulations at the RA-2 frequencies and observation angle, we can fund our considerations on the results achieved for TMR and MWR (operating at nadir) and for the 10 GHz TMI. Moreover, such considerations are based on the worst performances among those obtained in the two validations phases for the mentioned radiometers, i.e. we have adopted a conservative point of view.

As previously mentioned, it has emerged that, if we analyze the range 18-37 GHZ, the accuracy of the nadir simulations increases with the decrease of the frequency, therefore we can neglect the performances at 36.5-37.0 GHz. The worst results have been obtained for the MWR 23.8 channel (~ -2 K of bias and ~ 3.8 K of standard deviation error). As for the bias for the 10 GHz TMI channels, the worst results have been obtained in phase 2 (~ -3 K in horizontal polarization and ~ 1 K in vertical polarization). Since the emission properties at nadir can be approximately considered intermediate between the two linear polarizations (the coefficient a_0 of the model functions at 37 GHz for an observation at 53° are 0.37 in horizontal polarization, 0.70 in vertical one and 0.52 at nadir), we can make a gross assumption of a bias of about 2 K at 10 GHz at nadir. Since the scatterplots representing the comparisons between measured and simulated TB^{BOA} for TMR and MWR are quite scattered, we can estimate an accuracy of +/- 3 K for Ku band.

As for S band, some further considerations are necessary, since we have compared our simulations with those furnished by an empirical model. The maximum difference between the TB^{BOA} furnished by the two models was less than 2 K. Since we have to account also for the errors of the Trokimovshy model and of the atmospheric one we can assume for the error budget at S band a value of +/- 4 K.

5.0 Land models

5.1 Selection of calibration areas

As stated in Section 2, some calibration areas have been selected and their multifrequency brightness temperatures have been simulated by means of theoretical and/or semiempirical models. Land calibration areas have been selected on the basis of three fundamental requirements:

i) previous experience in analyzing and simulating brightness data of the areas;
ii) availability of theoretical models and/or previous experimental data;
iii) availability of a good dynamic range of brightness temperature values.

According to these requirements three areas, i.e. Amazonia, Sahara and Antarctica, have been considered. In a previous global emission study, the brightness temperatures of these three areas were simulated and comparisons with SSM/I multifrequency measurements produced a quite good fit (Schiavon et al., 1998). Moreover, a good dynamic range is ensured by the acquisition over both "warm" areas, such as Sahara and Amazonia, and "cold" areas, such as Antarctica. For the first validation phase, based on TMI and SSM/I signatures collected in the year 2000, three square sub-areas have been selected as listed below.

Amazonia:	5°S , 60°W	upper-left corner	Sahara:	23°N, 10°E
	10°S, 55°W	bottom-right corner		18°N, 15°E
			Antarctica:	68°S, 56°E
				78°S, 66°E

In the final validation phase, simulated brightness temperatures have been compared against TMI and SSM/I signatures collected in correspondence with RA-2 overpasses. In this case, signatures have been taken within strips internal to wide areas, within the limits indicated below.

Amazonia:	2°S , 60°W	upper-left corner	Sahara:	27°N, 9°E
	14°S, 54°W	bottom-right corner		15°N, 13°E
			Antarctica:	75°S, 57°E
				80°S, 78°E

5.2 Models description

This Section describes the models adopted for the three areas listed in Section 5.1, and shows the results of a basic parametric study. The emissivity has been simulated as a function of frequency using the theoretical and semiempirical models which will be described below. The simulated emissivity gives the ratio between brightness temperature and surface temperature. The results shown in this Section do not include atmospheric effects, which will be considered in Section 5.3. For each frequency, simulations have been performed for three configurations: i) nadir; ii) 52.5°, vertical (V) polarization; iii) 52.5°, horizontal (H) polarization. The first configuration is important for the objectives of this study, while the other ones allow us to compare model outputs with SSM/I and TMI data.

For each calibration area, inputs to the models have been given by considering an environmental context typical of the area and possible variations due to seasonal and/or local effects.

5.2.1 Forest

In order to simulate emission from Amazonia, a physical model, based on the radiative transfer theory and developed at Tor Vergata University, has been used. We briefly summarize here the main features of the model, as it has been used in this work.

The simulations concerned deciduous forests, which were divided into the following layers:

- The crown layer, made up of leaves and branches, represented as dielectric discs and cylinders whose absortion and bistatic scattering cross sections have been modeled by the Physical Optics (Le Vine et al., 1983) and the "infinite cylinder" approximation (Karam and Fung, 1988) , respectively;
- The trunk layer, modeled by means of dielectric cylinders whose electromagnetic properties have been described by the "infinite cylinder" approximation;

- The soil, whose bistatic scattering cross section has been simulated by using the Integral Equation Model (Fung, 1994) or the Geometrical Optics Model (Ulaby et al., 1986) at the higher frequencies.

Some details about electromagnetic characterization of the three forest components and combination of contributions are given below. Finally, information is given about specific aspects of model use to simulate emission from Amazonian forest.

5.2.1.1 Electromagnetic characterization of crown

The crown layer, filled with scatterers of different kinds, is subdivided into N thin elementary sublayers (Figure 11 in Ferrazzoli and Guerriero, 1996a). The structure is assumed to be symmetrical in azimuth. For each sublayer, both the upper and the lower half-spaces are subdivided into discrete intervals of incidence and scattering off-normal angles ϑ and ϑs, respectively.

The incidence and scattering azimuth angles are denoted by ϕ and ϕs, respectively. Due to azimuthal symmetry assumption, the scattering depends on the difference $\phi s - \phi$. The sublayer behaviour is characterized by the scatter matrices **S** and the transmission matrices **T**. Each element of an **S** (or **T**) matrix represents the ratio *Is/I* (or *It/I*) between the specific intensity *Is* (or *It*) scattered into an upper (lower) angular interval of ϑs and the specific intensity *I* incoming from an upper angular interval of ϑ. The dependence on $\phi s - \phi$ is expressed in Fourier series, so that the number of **S** and **T** matrices is equal to the number of the series terms. Since the emissivity has to be simulated, computation of the 0-th order matrices is sufficient, as demonstrated in Chapter 8 of Fung, 1994. The elements of the 0-th order **S** and **T** matrices can be computed by using formulas (2) and (3), respectively, of Ferrazzoli and Guerriero, 1996a.

In order to correctly include both the attenuation and the scattering effects, the downward scattered power, expressed by the 0-th order **T** matrix, must be added to the fraction of undisturbed power. This is accomplished by adding to the diagonal elements of the matrix a quantity equal to one minus the fraction of power traveling within each angular interval at each polarization which undergoes extinction in the considered sub-layer. This term may be computed by using formula (4) of Ferrazzoli and Guerriero, 1996a.

The contributions of two adjacent thin sublayers are then combined through the matrix ``doubling" algorithm (Chapter 8 of Fung, 1994), leading to formulas (5) and (6) of Ferrazzoli and Guerriero, 1996a. By reiterating this procedure, the N sub-layers are successively combined, and the scattering and transmission matrices of the whole crown are computed. The number N (power of two) of elementary layers into which the crown is subdivided is selected as the minimum value beyond which the finally computed emissivity does not vary by more than a given limit (e.g. 0.1 %).

5.2.1.2 Electromagnetic characterization of soil

The scattering properties of the soil are expressed by the dimensionless bistatic scattering coefficient , which depends on the permittivity and on the roughness of the surface. It may be computed by using the Integral Equation Model (Fung, 1994) or the Geometrical Optics Model (Ulaby et al., 1986) at the higher frequencies.
The models of scattering from rough soil surfaces require as input data the volumetric soil moisture, and the height standard deviation and correlation length of the surface. The computed bistatic scattering coefficient is then employed to obtain a 0-th order **Sg** matrix, which may be defined similarly to the 0-th order **S** matrix of the crown elementary layer. The elements of the **Sg** matrix can be computed by using formula (7) of Ferrazzoli and Guerriero, 1996a.

5.2.1.3 Electromagnetic characterization of trunk

Trunks are assumed to be near-vertical large cylinders, located between the crown and the soil. For these elements, most of the extincted power is either absorbed or scattered towards directions close to forward direction. It follows that trunk effect on the overall emissivity may be approximated to that of simple absorbers. The absorption cross-section has been analitically derived solving the volume integral of the cylinder inner field given by Karam and Fung, 1988. The accuracy of the absorption cross section formula has been verified by Ferrazzoli and Guerriero, 1996b, by means of the Forward Scattering Theorem, which ensures energy conservation to be satisfied. Trunk absorption is described by a transmission matrix **Tt** whose diagonal elements are given by formula (8) of Ferrazzoli and Guerriero, 1996a.

5.2.1.4 Computation of the emissivity

Crown, soil and trunk contributions are combined through the matrix operations given by formulas (9) and (10) of Ferrazzoli and Guerriero, 1996a. In this way the scatter matrix describing the upper half-space scattering of the whole forest medium is obtained. The polarized emissivity may be related to the bistatic scattering coefficient of the whole medium by the energy conservation law. Its discretized version, which is suitable to our numerical approach, is given by formula (12) of of Ferrazzoli and Guerriero, 1996a.

5.2.1.5 Selection of input variables for Amazonian forest

The model requires the following data as inputs: trunk density, trunk dimensions, branch density, branch dimensions distribution, branch orientation distribution, leaf dimensions distribution, leaf orientation distribution, soil moisture, soil roughness parameters. Of course, such detailed data sets are not available at large scale. Therefore, some inputs have been assigned on the basis of reasonable assumptions. As far as density and dimensions of woody elements (trunks, branches) is concerned, we have used the values typical of dense forests, on the basis of data available in the literature. Branch orientation has been assumed to be uniformly distributed between 25° and 65°, in order to represent a mixed forest. For Leaf Area Index, a high value equal to 5 has been assumed. Leaf thickness has been set equal to 0.2 mm. To account for shape irregularities, each leaf has been subdivided into several discs, corresponding to different phase centers, as suggested by Fung (1994). Increasing irregularities produces an increase of absorption/emission effects. Simulations have been performed under the assumption of discs with 1 cm diameter and orientation distribution with a maximum for a disc axis oriented at 67.5° from the vertical. The gravimetric moisture has been set equal to 70% for leaves, 50% for trunks and branches. These values are typical for forests. The dielectric constants of soil and vegetation elements has been connected to their moisture content using semi-empirical formulas available in the literature (El-Rayes and Ulaby, 1987).

The obtained trends of emissivity vs. frequency are shown in Figure 5.1. For each sensor configuration, simulations have been performed for a wet soil with 30% moisture (lower emissivity values) and for a dry soil with 10% moisture (higher emissivity values). The trends are generally flat, with limited variations vs. frequency. The emissivity values are higher than 0.87 in all cases. The uncertainty associated to soil moisture is about 0.03 emissivity units, corresponding to about 9K, for the worst case of S band at nadir. This case, among the considered ones, corresponds to the lowest crown attenuation. As expected, a lower sensitivity to soil moisture variations is observed at high frequencies and/or high angles

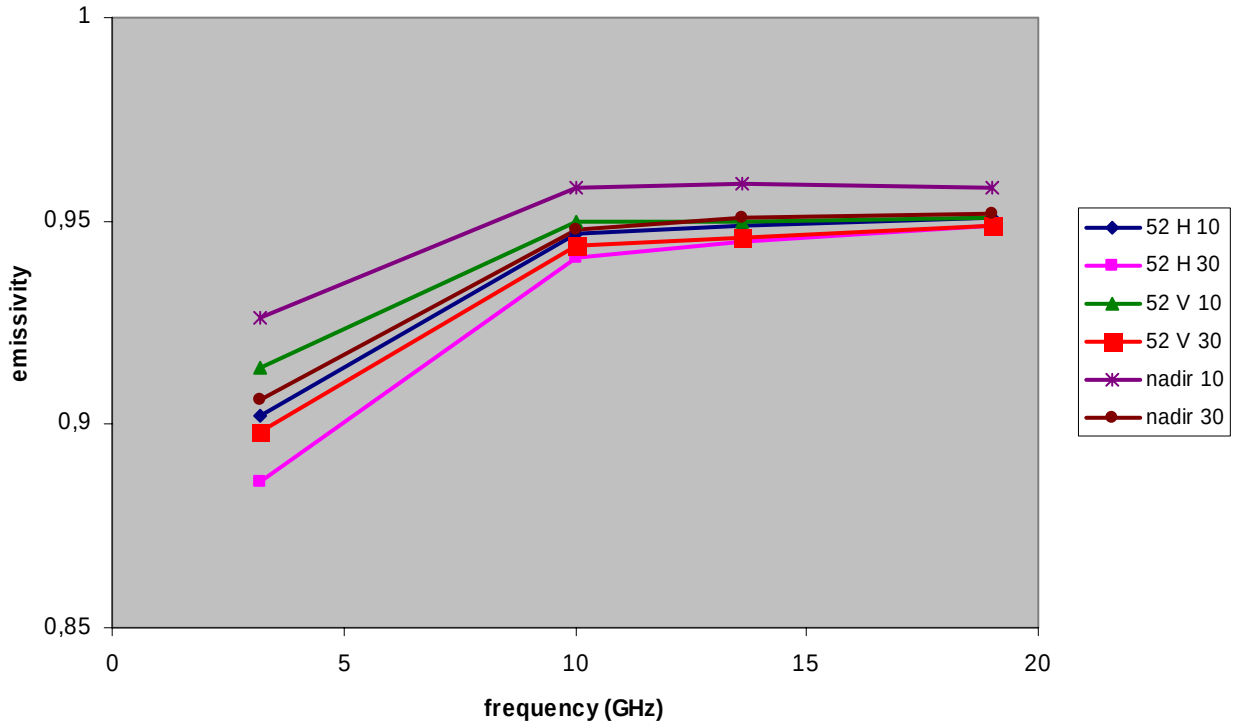

Figure 5.1 *Simulated emissivity vs. frequency for Amazonian forest. Soil moisture equal to 10% and 30%.*

5.2.2 Desert

The emission of Sahara desert has been simulated by using the Geometrical Optics surface model (Ulaby et al., 1982) for frequencies higher than 5 GHz and the Integral Equation surface model (Fung, 1994) for frequencies up to 5 GHz. Both models have been used in in their bistatic version. The emissivity has been computed using the energy conservation law, after evaluating the reflectivity as the integral of the bistatic scattering coefficient in the upper half-space (Ulaby et al., 1982).

For Sahara desert, the trends of emissivity vs. frequency are shown in Figure 5.2. The Figure has been obtained for a slope (as defined by Ulaby et al., 1982) of 0.15 and two different soil moistures, i.e. 1% and 5%. Although the difference between the two soil moisture is moderate (both of them correspond to dry soils), the difference between emissivity values is appreciable, especially at nadir and at H polarization. All trends are flat in the 10-20 GHz range.

More significant variations are observed when the frequency lowers below 10 GHz. Differently from the forest case, polarization effects are appreciable for desert.

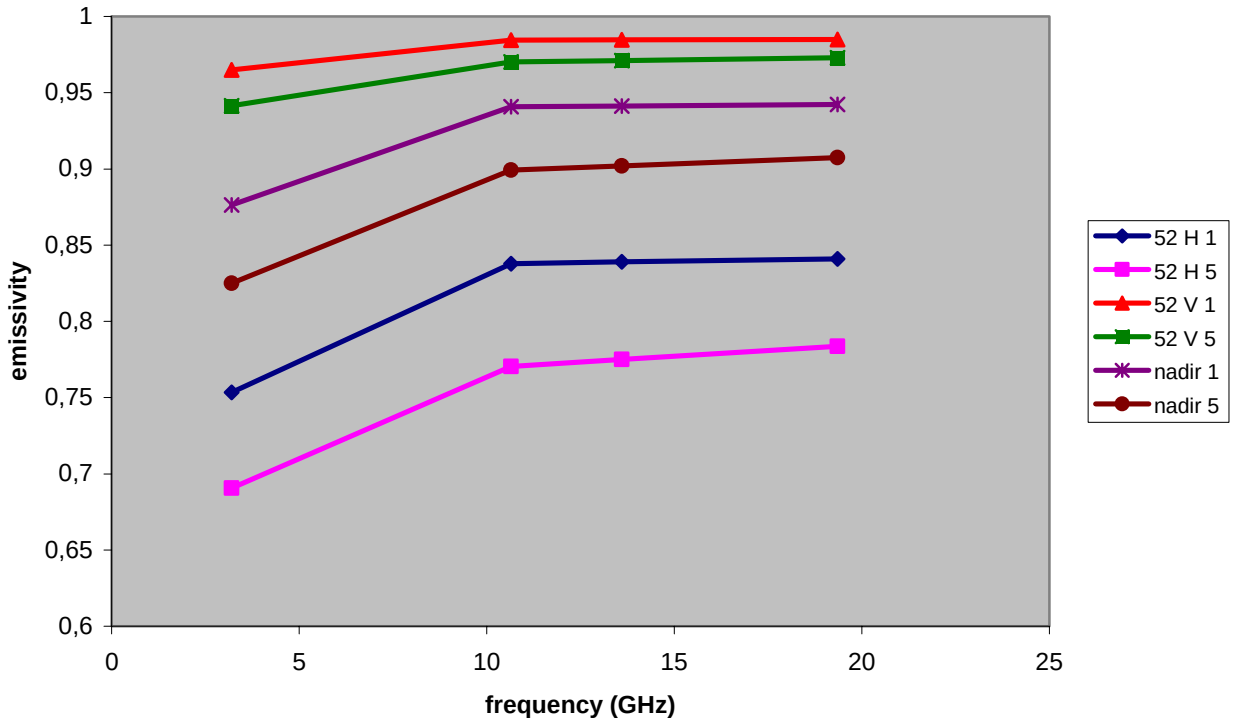

Figure 5.2. *Simulated emissivity vs. frequency for desert. Surface slope equal to 0.15. Soil moisture content equal to 1% and 5%.*

5.2.3 Continental ice

Antarctica continental ice has been simulated as a half space with flat interface characterized by an "equivalent" uniform permittivity. Nadir emissivity values have been assigned by fitting 3 years of experimental data collected over Antarctica by SMMR radiometer, published by Rott (1989).

Figure 5.3 shows the trends of emissivity vs. frequency for Antarctica continental ice. The definition of emissivity is not straightforward, in this case, since the penetration depth is of the order of some meters and increases with decreasing frequency. In Figure 5.3, which is based on experimental data published by Rott (1989), the emissivity has been estimated as the ratio between the brightness temperature and the snow temperature at 10 m depth, which corresponds to the long term mean annual temperature. Results are shown for the extreme seasonal conditions, corresponding to February and August months. At the lower frequencies, the emission is more stable with time, since it is mostly produced at low depths, which are scarcely influenced by seasonal variations. The effect of polarization is remarkable.

5.3 Validation and tuning

5.3.1 Approach

As previously stated, simulation outputs have been compared with brightness data collected by SSM/I and TMI over pixels belonging to the three areas indicated in Section 5.1. To this aim, information available in ECMWF files has been considered.

In order to simulate the top-of-atmosphere brightness temperature, the following information is needed:

1 Surface emissivity, which has been computed using models described in previous Section;
2 Surface temperature;

3 Mean radiative temperature and optical thickness of the atmosphere.

For Amazonian forest, the surface temperature has been set equal to the skin temperature, available in the ECMWF files. This assumption is realistic, and produced the best fit to experimental data. Moreover, a soil moisture content equal to 20% has been taken. Several pixels have been discarded within the boxes indicated in Section 5.1, since they were partially filled by large Amazonian rivers. The latter produced strong emissivity decrease. Only pixels completely dominated by forest have been considered.

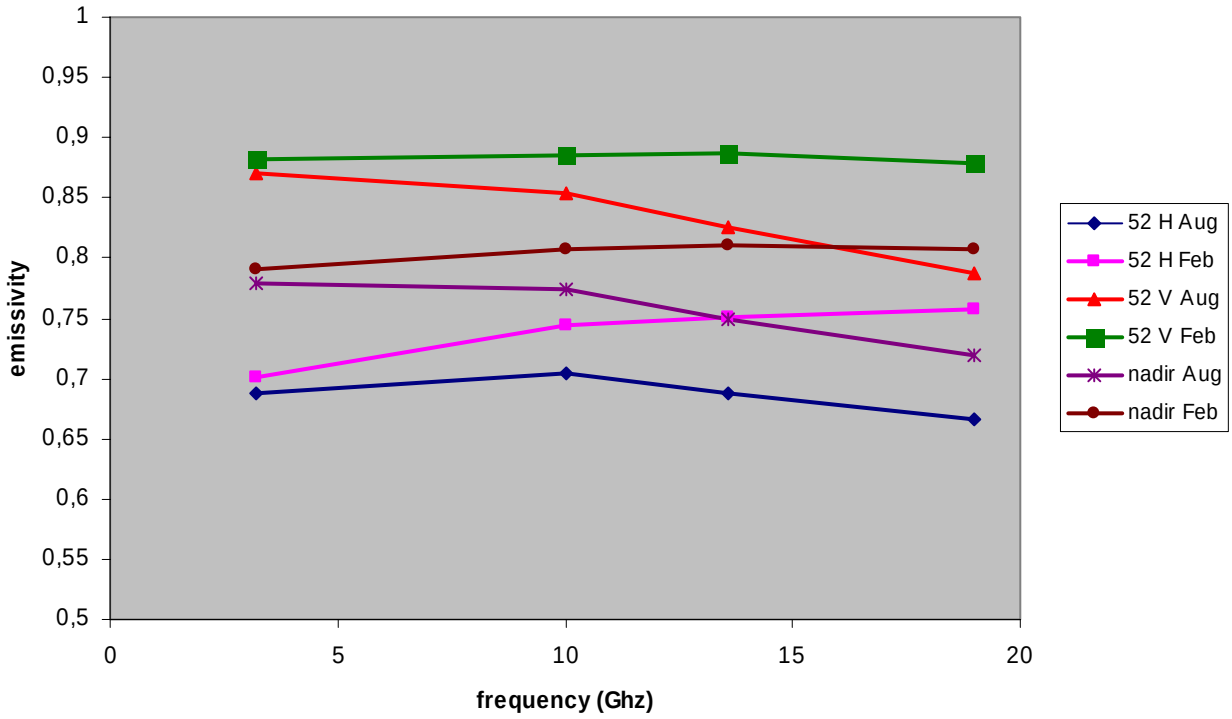

Figure 5.3 *Simulated emissivity vs. frequency for continental ice. Cases of February and August.*

For Sahara desert, the emitting layer has been assumed to have a maximum depth of 28 cm at frequencies higher than 10 GHz. This corresponds to the first two levels in ECMWF data. The medium temperature has been computed as the weighted mean of temperatures of the two levels. The soil moisture has been assumed to be equal to 1% at the top layer, and to increase with depth with the same rate of wetness data in the ECMWF files. At S band, a similar approach has been adopted, but with a maximum depth of 100 cm, corresponding to threee ECMWF levels. The average surface slope has been set equal to 0.15. This latter value is realistic for desert, and leads to the best correspondence with experimental data.

For Antarctica continental ice, temperature data have been taken in the lowest available layer, i.e. 100-255 cm, for frequencies higher than 10 GHz. According with the results published by Rott (1989) this depth is of the same order as the penetration depth at 19 GHz. As stated in Section 5.2.3, the emissivity values of Figure 5.3 refer to the snow temperature at 10 m depth, which corresponds to the long term mean annual temperature. These emissivity values have been modified, in order to refer to a different depth. At S band, the same temperature values of Figure 5.3, i.e. average values measured at 10 m depth in 3 Antarctica stations (Rott, 1989), have been taken.

Atmospheric variables available in ECMWF files have been used to compute the atmospheric mean radiative temperature T_{mr} and the optical thickness τ, according with the procedure described in Section 3. Pixels with a liquid water content higher than 0.1 cm have been discarded.

5.3.2 Validations with signatures of year 2000

The previously described procedure has been applied to the images of year 2000 listed in Section 2. The total number of processed pixels, for each frequency, is: 3931 for TMI, 2832 for SSM/I,.

Comparisons between simulated and measured top-of-atmosphere brightness temperatures are shown in Figures 5.4, for TMI data 10.6 GHz, and 5.5, for both TMI and SSMI data at 19.3 GHz. Samples belonging to different sites and/or different polarizations are identified by codes. In general, the models are able to represent the measured brightness data over the whole range. For each group of site/polarization data, the center is located close to the 45° straightline. For

Sahara and Antarctica samples there is a relatively high dispersion in measured values, which is not well represented in modeled values. This dispersion problem is more pronounced at H polarization than at V polarization.

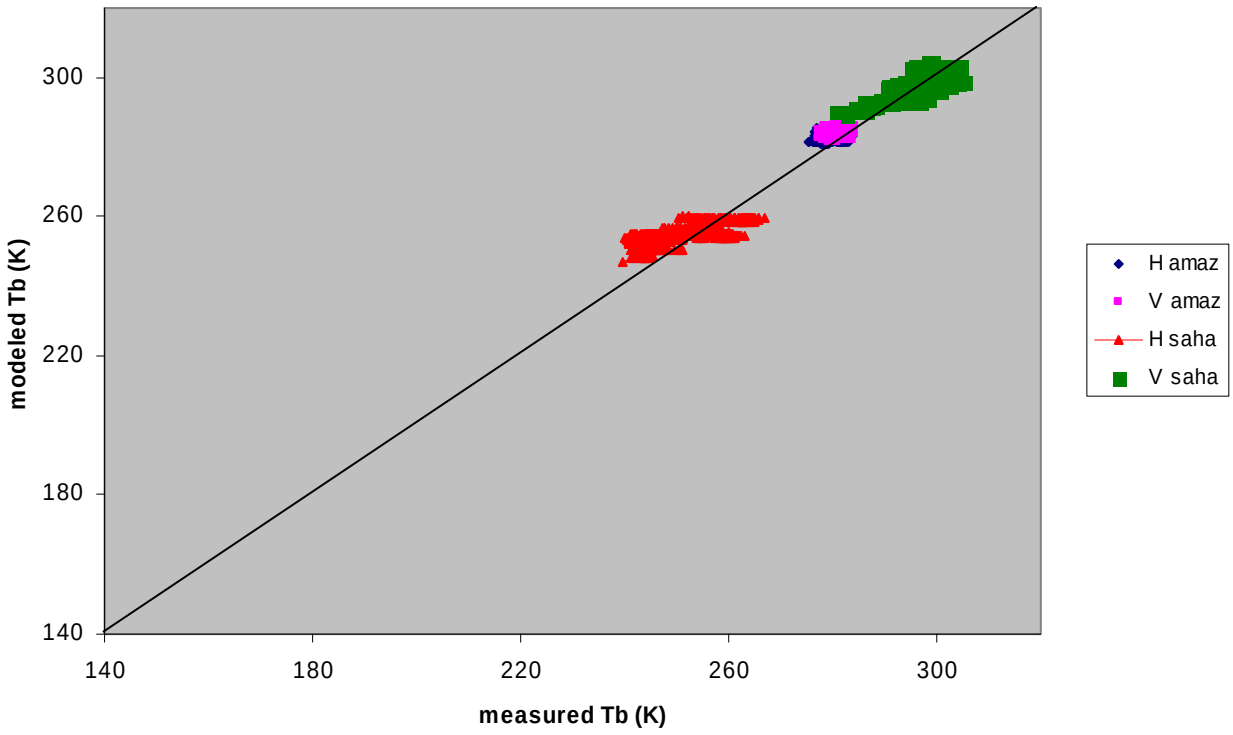

Figure 5.4 *Comparison between modeled and measured brightness temperatures. Year 2000. TMI, 10.6 GHz.*

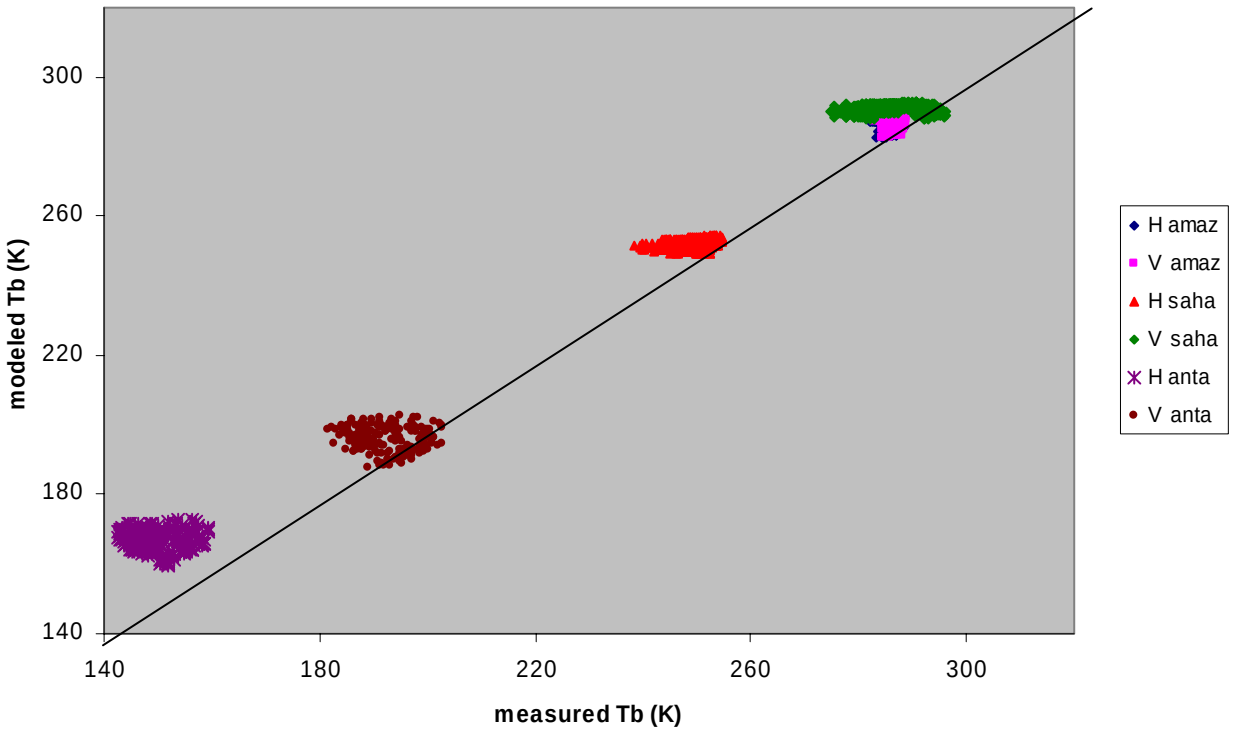

Figure 5.5 *Comparison between modeled and measured brightness temperatures. Year 2000. TMI and SSM/I, 19.3 GHz.*

An overall error analysis has been carried out, leading to results of Table 5.1, for 10.6 GHz data and Table 5.2, for 19.3 GHz data. For both instruments (TMI and SSMI) the values of rms and bias errors have been computed. Computations have been carried out over the single calibrations areas.

Table 5.1 *Error analysis for data of year 2000 at 10.6 GHz.*

	Amazonia	Sahara	Antarctica
TMI samples	1133	2798	0
SSM/I samples	0	0	0
TMI rms H pol. V pol.	3.9 3.5	6.3 2.5	- -
SSM/I rms H pol. V pol.	- -	- -	- -
TMI bias H pol. V pol.	3.5 3.0	4.2 0.6	- -
SSM/I bias H pol. V pol.	- -	- -	- -

Table 5.2 *Error analysis for data of year 2000 at 19.3 GHz.*

	Amazonia	Sahara	Antarctica
TMI samples	1133	2798	0
SSM/I samples	334	1192	1306
TMI rms H pol. V pol.	3.4 2.5	7.6 4.7	- -
SSM/I rms H pol. V pol.	1.4 1.7	5.9 5.4	12.1 8.7
TMI bias H pol. V pol.	2.9 1.7	-3.9 -3.0	- -
SSM/I bias H pol. V pol.	-0.4 -1.1	-1.3 0.3	4.3 -1.3

5.3.3 Validations with signatures of years 2002-03

TMI and SSM/I signatures collected in years 2002-03, in correspondence to RA-2 overpasses, have been used for a further validation of models. Comparisons between measured and simulated data have been performed by using the same models as those used for year 2000 simulations, as well as the same criteria to give input data.

Some new problems have been found with 2002-03 data. ECMWF information is available at 12:00 GMT and at 24:00 GMT. In 2000 simulations, we had the possibility to select times and strips of TMI and SSM/I overpasses, provided a part of the boxes (indicated in Section 5.1) was covered. We selected overpasses in such a way as to minimize the time shift with respect to ECWF acquisitions. This flexibility was not possible with 2002-2003 data, due to two main constraints:

- TMI and SSM/I strips had to be coincident with RA-2 ones;
- TMI and SSM/I overpasses times had to be as close as possible to RA-2 overpasses.

As a consequence of these limitations, some overpasses (especially TMI ones) showed appreciable time shifts, with respect to ECMWF acquisitions, with maximum values of about 4 hours. Such time intervals may produce important temperature variations, affecting the comparisons between simulated and measured brightness temperatures. Two actions have been undertaken to overcome this problem:

- ECMWF forecasts, which are available with 3 hours sampling time, have been adopted, in addition to ECMWF acquisitions at 12:00 GMT and 24:00 GMT;
- Linear interpolations and/or extrapolations have been applied to time trends of brightness temperatures.

Comparisons between simulated and measured top-of-atmosphere brightness temperatures are shown in Figures 5.6, for TMI data at 10.6 GHz, and 5.7, for both TMI and SSMI data at 19.3 GHz. Samples belonging to different sites and/or different polarizations are identified by codes. Considerations similar to those of year 2000 data may be applied.

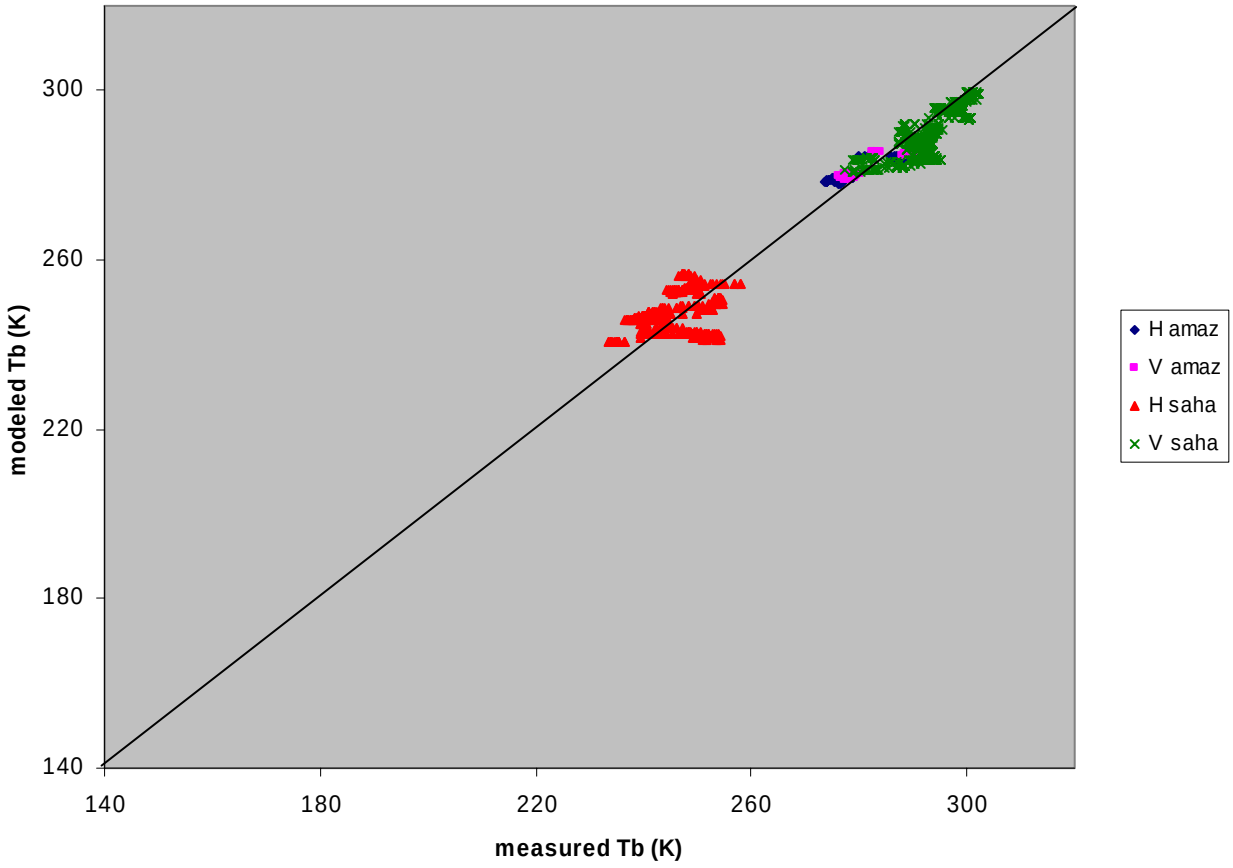

Figure 5.6 *Comparison between modeled and measured brightness temperatures. Years 2002-03. TMI, 10.6 GHz.*

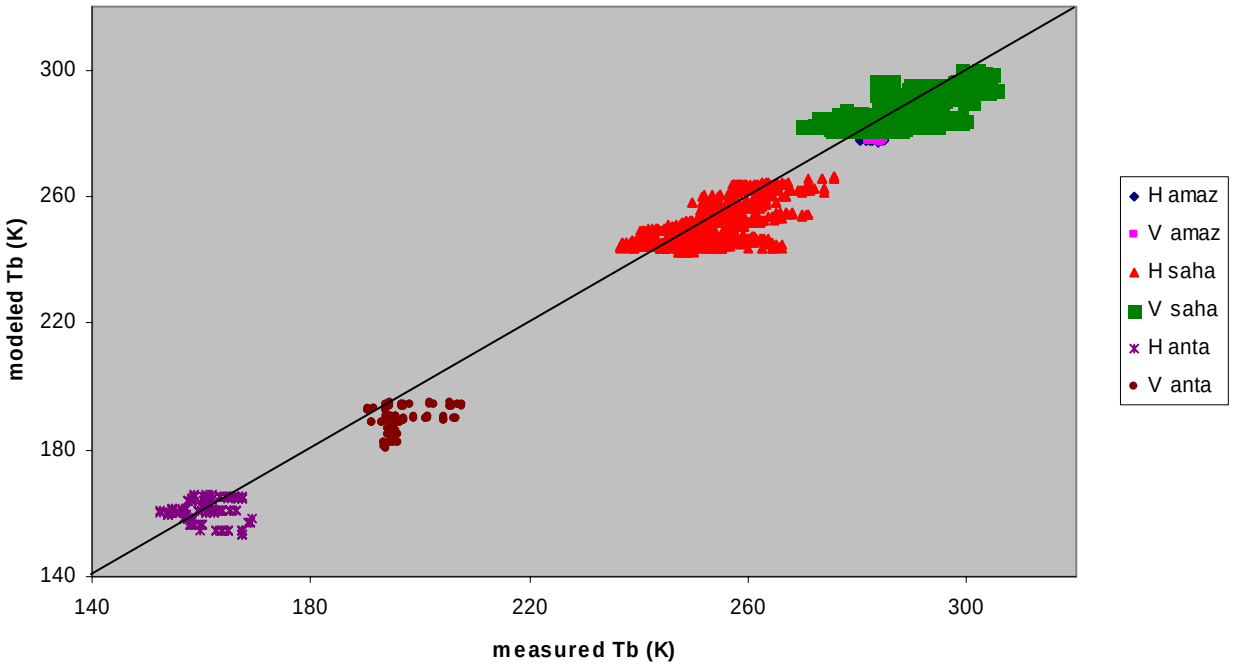

Figure 5.7 *Comparison between modeled and measured brightness temperatures. Years 2002-03. TMI and SSM/I, 19.3 GHz.*

Similarly to 2000 year case, an overall error analysis has been carried out, leading to results of Table 5.3, for 10.6 GHz data and Table 5.4, for 19.3 GHz data. For both instruments (TMI and SSMI) the values of rms and bias errors have been computed. Computations have been carried out over the single calibrations areas.

Table 5.3 *Error analysis for data of years 2002-03 at 10.6 GHz.*

	Amazonia	Sahara	Antarctica
TMI samples	116	435	0
SSM/I samples	0	0	0
TMI rms H pol. V pol.	3.2 2.5	5.7 4.3	- -
SSM/I rms H pol. V pol.	- -	- -	- -
TMI bias H pol. V pol.	1.2 0.2	2.1 -2.9	- -
SSM/I bias H pol. V pol.	- -	- -	- -

Table 5.4 *Error analysis for data of years 2002-03 at 19.3 GHz.*

	Amazonia	Sahara	Antarctica
TMI samples	116	435	0
SSM/I samples	381	1063	162
TMI rms H pol. V pol.	2.6 2.7	8.0 6.1	- -
SSM/I rms H pol. V pol.	2.7 3.4	5.2 5.1	5.2 9.0
TMI bias H pol. V pol.	0.1 -1.1	-3.2 -4.2	- -
SSM/I bias H pol. V pol.	-2.1 -3.0	-2.6 -1.9	-0.3 -7.7

5.4 Estimated accuracy of simulated brightness at Ku and S band

The models described in previous Sections, validated by comparisons with TMI and SSM/I signatures, have been used to predict nadir brightness temperatures at Ku and S band. Outputs of this work have been adopted to calibrate RA-2, according to the procedure which will be described in Section 6. An overview of expected errors in predicted brightness temperatures is given below.

5.4.1 Ku band

Ku band is located between 10 GHz and 19 GHz. RA-2 data are collected at nadir. For Amazonian site, variations with angle are low (see Fig. 5.1). For Sahara and Antarctica sites, angle effects are strong, but emission properties at nadir are intermediate between vertical and horizontal polarization ones (see Figs. 5.2 and 5.3). As a consequence of these considerations, the data reported in Tables 5.1- 5.4 are well representative of the accuracy we can expect at Ku band and at nadir.

5.4.2 S band

Estimating the accuracy of our simulation is more critical at S band than at Ku band. A general problem is related to the scarce availability of experimental brightness data at S band, especially over large areas. Other problems are specific of the various kinds of surfaces, as indicated below.

- Amazonian forest.

Soil moisture effects are negligible at high frequencies and high angles (as it is the case of TMI and SSM/I acquisitions). No significant correlations were observed between TMI and SSM/I temperatures measured in 2000 and ECMWF soil wetness estimates. Some effects of soil moisture could be present at S band and nadir. An estimate of these effects for soil moisture ranging from 10% to 30% is given in Fig. 5.1. However, in a dense forest moisture variations are generally limited, provided extreme events, such as flooding, are not considered.

Other possible inaccuracies could be related to the different nature of scattering at low frequencies. In fact, at frequencies higher than 10 GHz scattering is mainly due to leaves, while branches are dominant at lower frequencies. This could be make not totally significant our previous validations.

Despite the lack of satellite measurements at S band, some ground based radiometric measurements were carried out at several frequencies, including S band, over forest and could be considered as reference to understand the accuracy of our estimates. In particular, we have take into consideration measurements presented in the literature and performed on a submerged Pine forest (Shutko and Chuklantsev, 1982) and over Beech and Oak forests at L and C band and higher frequencies (Macelloni et al., 2001). Comparisons between our simulations and these signatures must be done with caution, since forest types are different. In any case, differences are lower than +/- 2 K in both cases. For the case of Beech and Oak forests, a linear interpolation between L and C band has been applied.

Based on the previous considerations, as for the accuracy of our simulation at S band we can roughly assume an upper and conservative figure in the order of +/- 3 K.

- Sahara desert

No S band experimental data are available for deserts. Moreover, we simulated the brightness temperatures by averaging within an upper layer with 1 m thickness. This corresponds to the maximum available depth in ECMWF data, but may not be completely appropriate. On the contrary, we may expect brightness temperature to be more stable at lower frequencies, since it is more contributed by lower depths.

The accuracy for desert data may be assumed to be +/- 5 K

- Antarctica

For Antarctica data, there are several serious inaccuracy sources at S band. The accuracy of ECMWF information, used for temperature inputs, is questionable. Moreover, emissivities have simply be estimated by extrapolating to lower frequencies SMMR values published by Rott (1989). Finally, at S band emission is due to radiation from layer much deeper than the maximum depth of 255 cm available in ECMF data. Therefore, an average value at 10 m depth, measured in some Antarctica stations and published by Rott (1989), has been taken. We definitively do not recommend to use simulations over continental ice at the present status of the simulation model, unless they confirm what has been found with the other surfaces types.

6 RA-2 RECEIVER CALIBRATION RESULTS

6.1 The RA-2 receiver chain

The expression of the altimeter radar return (waveform) at the output of an ideal antenna as function of time t is derived from document PO-NT-RAA-0004-CLS, which makes reference to the paper by Hayne, 1980:

$$V_m(t) = a_\xi \frac{P_u}{2} e^{-v} \left\{ [1+erf(u)] + \frac{\lambda_s}{6}\left(\frac{\sigma_s}{\sigma_c}\right)^3 \left\{ [1+erf(u)] c_\xi^3 \sigma_c^3 - \frac{\sqrt{2}}{\sqrt{\pi}} [2u^2 + 3\sqrt{2} c_\xi \sigma_c u + 3c_\xi^3 \sigma_c^3 - 1] \exp(-u^2) \right\} \right\} + P_n \quad (6.1)$$

parameter u is given by:

$$u = \frac{t - \tau - c_\xi \sigma_c^2}{\sqrt{2}\sigma_c} \quad (6.2)$$

where τ is the epoch (the two way delay of the sea surface echo) and parameters a_ξ, c_ξ, σ_c depend on mispointing ξ, antenna beam-width θ_0, sea roughness standard deviation σ_s and transmitted pulse width σ_p. P_n is the noise power superimposed to the signal power. An example of mean waveform is given in Fig. 6.1, where P_u=100 is assumed and the other parameters are listed in the figure caption.

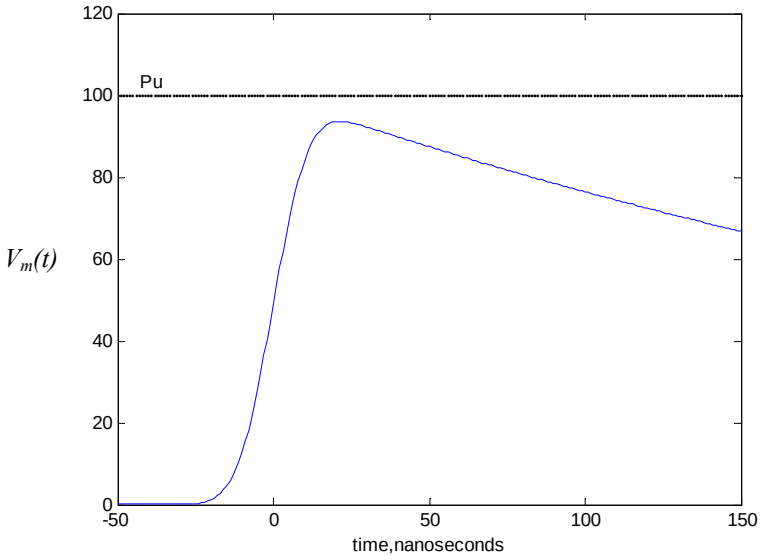

Fig.6.1 Example of altimeter mean return waveform obtained assuming P_u=100, θ_0=1.5°, ξ=0 and SWH= 5 m.

For the purpose of the sigma naught calibration, we are not interested in the shape of the waveform and in the pulse return time, but only in the amplitude of the echo. Therefore, we rewrite the previous formula as follows:

$$V_m(t) = P_u W(t) + P_n \quad (6.3)$$

According to the complete expression, P_u is the amplitude the echo achieves in the absence of mispointing for a flat Earth and an isotropic antenna pattern, as it results from the example in figure 6.1. *W(t)* represents the shape of the waveform as function of time, which depends on all the parameters mentioned above (note that when ξ=0 and $t \to \infty$, it turns out $1 + erf(u) \to 2$).

The amplitude P_u is therefore given by the standard radar equation, corresponding to the condition of maximum illuminated area, as depicted in figure 6.2. The following relation applies:

$$P_u = W_r = \frac{W_t \lambda^2}{(4\pi)^3} \frac{D^2 \sigma^0 A}{R^4} \quad (6.4)$$

where W_t is the transmitted power (the power the antenna radiates in the free space), W_r is the received available power, D is the antenna directivity, R is the range (R is assumed constant within area A and equal to the height of antenna above the surface), A is the illuminated area. At the first order, being σ_τ the width of the transmitted pulse in the space coordinate ($\sigma_\tau = c\tau/2 = c/2B$, where τ is the compressed pulse width in time units and B_{chirp} is the pulse bandwidth), from figure 6.2 it turns out that:

$$h^2 + r^2 = \left(h + \sigma_\tau\right)^2 \qquad h^2 + r^2 = h^2 + \sigma_\tau^2 + 2h\sigma_\tau$$

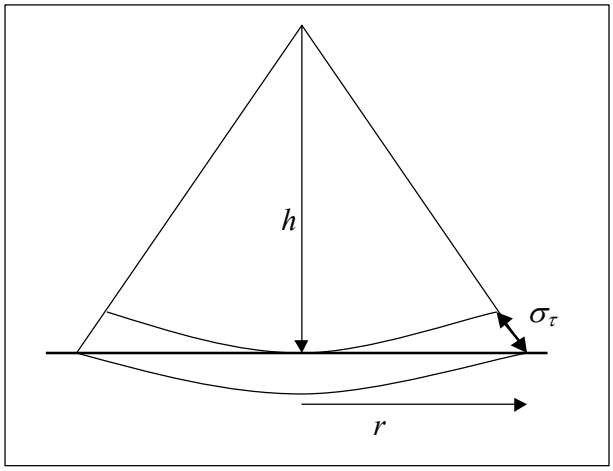

Fig. 6.2: Radar equation geometry in case of a flat Earth surface.

As $\sigma_\tau << h$, it comes out $r^2 = 2h\sigma_\tau$ and the portion of a flat Earth illuminated by the radar pulse has area A given by:

$$A = \pi r^2 = 2\pi h\sigma_\tau \tag{6.5}$$

Therefore:

$$P_u = W_r = \frac{W_t\lambda^2}{(4\pi)^3}\frac{D^2\sigma^0 2\pi h\sigma_\tau}{R^4} = \frac{W_t\lambda^2 D^2\sigma^0\sigma_\tau}{2(4\pi)^2 h^3} = \frac{W_t\lambda^2 D^2\sigma^0 c}{4(4\pi)^2 h^3 B_{chirp}} \tag{6.6}$$

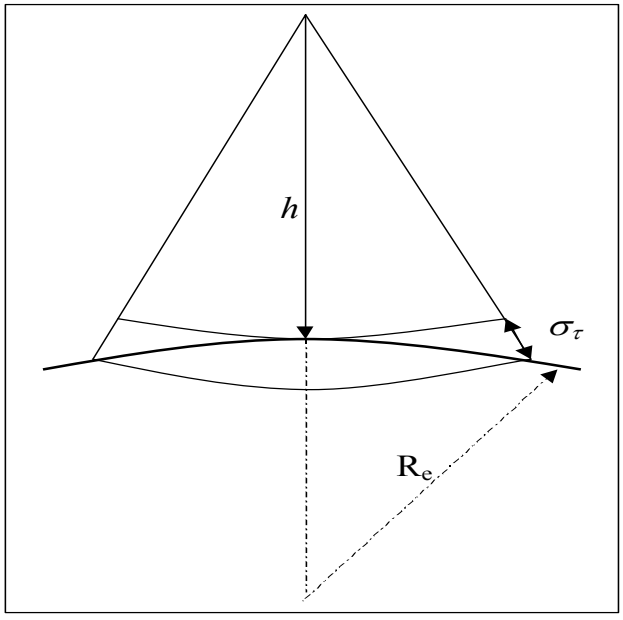

Fig. 6.3 Radar equation geometry in case of a spherical Earth surface

Note that W_r is the power at the receiver input only in case of absence of antenna losses and mismatching losses. The first are accounted for by introducing the gain G in place of directivity D. In case a spherical Earth is assumed, a

slightly different equation has to be considered that includes the Earth radius R_e, as shown in figure 6.3. It is possible to demonstrate (Rodriguez, 1988) that h has to be replaced by $h(1+h/R_e)$. A slightly different computation leads to another formula where $(1+h/R_e)$ appears at the first power (ref. private communication from ESA, Santella's thesis, 1987) and therefore we can write (M= 1 or 3):

$$P_u = W_r = W_t D^2 \frac{\lambda^2 \sigma^0 c}{4(4\pi)^2 h^3 \left(1+\frac{h}{R_e}\right)^M B} \tag{6.7}$$

The formula with M=1 has been adopted in the ESA RA-2 data processing.

At the output of the instrument, the samples of the detected signal $P(k)=I^2(k)+Q^2(k)$ (k=1, 128 for Ku band, k=1,64 for S-band) equals the received power W_r multiplied by the gain of the receiver chain, including antenna and front-end electronic losses, plus the noise. The noise includes the environmental noise (or clutter), the receiver noise and the noise due to the lossy antenna. The following scheme is considered for RA-2, which was adapted from the relevant applicable documents:

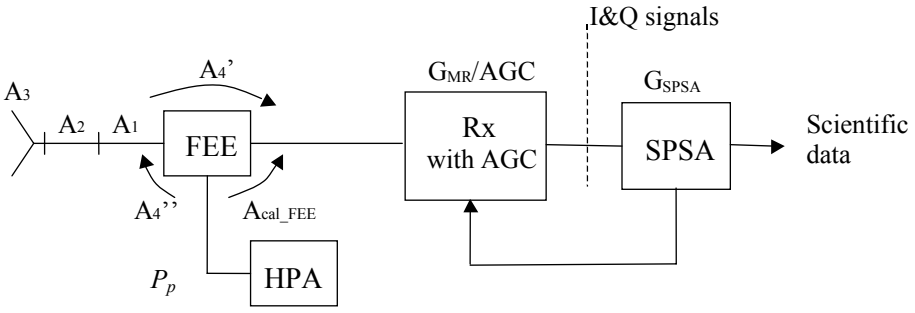

Fig. 6.4: RA-2 breakdown.

The attenuation of the radar signal due to the antenna both when transmitting and receiving is taken into account by replacing directivity D with antenna gain G_A ($G_A=D/A_3$). Therefore it turns out that:

$$P(k) = \frac{G_{Rx}}{AGC} P_u W(k) = \frac{G_{MR} G_{SPSA}}{AGC \cdot A_R} \frac{W_t \cdot \lambda^2 G_A^2 \sigma^0 c \cdot W(k)}{4(4\pi)^2 h^3 \left(1+\frac{h}{R_e}\right)^M B_{chirp}} = \frac{G_{MR} G_{SPSA}}{AGC \cdot A_R} \frac{P_p}{A_T} \frac{\lambda^2 G_A^2 \sigma^0 c \cdot W(k)}{4(4\pi)^2 h^3 \left(1+\frac{h}{R_e}\right)^M B_{chirp}} \tag{6.8}$$

where G_{RX}/AGC is the overall gain of the receiver, in which the attenuation AGC of the step attenuator is made explicit. G_{MR}/AGC is the gain of the analogical part of the receiver up to the digital output of the I&Q detector, G_{SPSA} is the gain of the digital signal processing module of the receiver chain, P_p is the power at the output of the High Power Amplifier (HPA) and A_R and A_T are the attenuations of the front-end in the receiving and transmitting path, respectively. Symbols A and AGC represent attenuation values, whilst symbol G is used to represent gain values. The digital module performs FFT, square detection and accumulation over 100 return echoes for Ku channel (25 from S channel). A_4', A_4'' and A_{cal_FEE} are the attenuations of the Front End Electronic (FEE) between the different paths of the three-port device. A_1 and A_2 are the attenuations in the waveguides and A_3 is the attenuation due to the lossy antenna.

It has been also introduced a further block ΔR_x to account for in-flight changes of the analogical receiver with respect to nominal receiver R_x, as it has been characterized on ground. ε^F is the gain of ΔR_x , i.e. the variable and unknown factor of the receiver gain. With these assumptions, during in flight nominal tracking, the scheme in figure 6.5 is applicable, where the outputs $X(k)$ of the I&Q detector and the samples $P(k)$ transmitted on ground (RAW data) are also indicated. By making explicit the factors forming A_R and A_T, Eq. 6.8 becomes:

$$P(k) = \frac{G_{MR} \cdot G_{SPSA} \cdot \varepsilon^F}{AGC \cdot A_1 A_2 A_4'} \frac{P_p}{A_4'' A_2 A_1} \frac{\lambda^2 G_A^2 c \sigma^0}{4(4\pi)^2 h^3 \left(1+\frac{h}{R_e}\right)^M B_{chirp}} \cdot W(k) \tag{6.9}$$

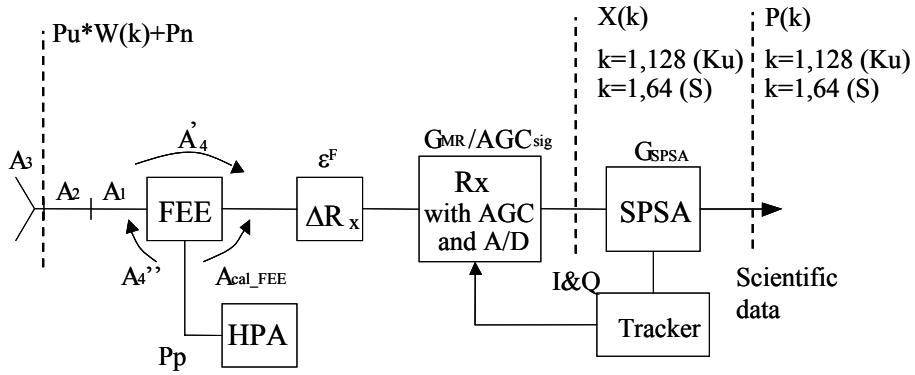

Fig. 6.5: RA-2 breakdown during in flight standard operations.

The value of *AGC* of the step attenuator in decibel is derived from the nominal setting expressed in decibel (AGC_{coarse}) by applying a transformation (function *f*) that account for non linearity of the device and for an adjustment factor of the tracking system $\Delta\alpha$ (the former only for S band). The linear value of AGC is then computed by the following (note that a different formula is used in TNO/RAS/0018/ALS, page 173):

$$AGC = 10^{f(AGC_{coarse}+\Delta\alpha)/10} \tag{6.10}$$

6.1.1 The pre-flight receiver gain

According to scheme in fig. 6.4, the pre-flight (nominal) receiver gain (including the AGC attenuation) is:

$$\frac{G_{RX}}{AGC} = \frac{G_{MR}}{AGC}\frac{G_{SPSA}}{\cdot A_R} = \frac{G_{MR}G_{SPSA}}{AGC \cdot A_1 \cdot A_2 \cdot A_4^{'}} \tag{6.11}$$

where G_{MR} is the analogical receiver gain, G_{SPSA} is the digital receiver gain and A_R includes all the waveguide attenuations.

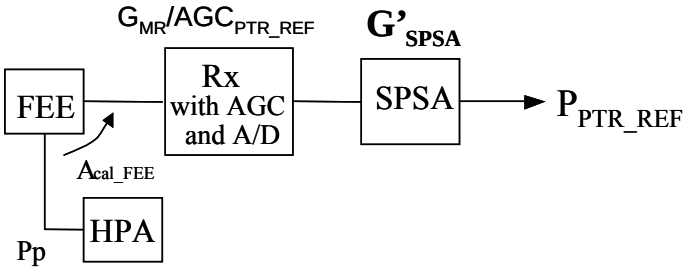

Fig. 6.6: RA-2 breakdown during pre-flight PTR calibration.

The pre-flight (nominal) gain was determined on ground via the internal calibration loop as in the configuration of figure 6.6. The output power P_{PTR_REF} has been derived by off-line processing the I&Q samples through the SPSA module, resulting in the following:

$$P_{PTR\_REF} = \frac{P_P\left(G_{MR}/AGC_{PTR\_REF}\right)G'_{SPSA}}{A_{CAL\_FEE}} \tag{6.12}$$

where AGC_{PTR_REF} was the setting of the step attenuator during the on ground characterization of the receiver. For sake of generality, it has been assumed that the processing of the I&Q samples during the on ground characterization, thus gain G'_{SPSA}, could have been different from the RA-2 on board digital processing during flight operations (gain G_{SPSA}). The overall receiver gain (analogical and digital gains) and the peak power at the output of the HPA were combined together into a global parameter named G_{Tx_Rx} (one value per band) which is therefore related to the P_{PTR_REF} measured on ground by the following:

$$G_{TX\_RX} = P_P G_{MR} G_{SPSA} = P_{PTR\_REF} A_{CAL\_FEE} AGC_{PTR\_REF} \frac{G_{SPSA}}{G'_{SPSA}} \tag{6.13}$$

Such parameter is very useful for radar characterization, being easy to be measured on ground. Therefore the pre-flight gain of the receiving path, including the attenuations in the front-end electronic can be related to G_{TX_RX} by the following:

$$\frac{1}{ACG} G_{RX} = \frac{1}{ACG} \frac{G_{TX\_RX} / P_p}{A_1 \cdot A_2 \cdot A_4^{'}} = \frac{1}{ACG} \frac{G_{TX\_RX} / P_p}{A_R} \tag{6.14}$$

where the total attenuation in the front end electronic $A_R=A_1A_2A'_4$ and the output power of the HPA were also measured during the on ground characterization. In decibel units the constant part of the gain (i.e., excluding the step attenuator) becomes:

$$G_{RX}\big|_{dB} = G_{TX\_RX} - P_p - A_R \tag{6.15}$$

From Envisat documentations (Doc. PO-TR-ALS-RA-0042) and private communication from ESA staff, the values in Table 6.1 have been assumed for the receiver operating during the Commissioning Phase (Configuration RFSS A and HPA A). Worth to point out that the attenuation from HPA to FEE input, that must be accounted for in "active" operations, should not be considered in this computation and that only A_4' must be taken into account. Values of P_{PTR_Ref} come out from private communications from ESA. From the same source we get the ratio between gains of digital processing on board and on ground, that is the ratio G_{SPSA}/G_{SPSA}'. The on board processing accumulate 100 samples for Ku band (25 for S band), performs a bit shifting amounting to a gain factor of 8 and applies an Hamming weighting producing an attenuation of H_att=3.3584. The ground processing during on ground characterization is assumed coincident with that performed on PTR calibration data in the L1B processor, whose gain will be named G_{PTR}.in the following. This module uses an individual sample and does not perform neither bit shifting nor Hamming weighting. Than it comes out that $G_{SPSA}/G'_{SPSA}= G_{SPSA}/G_{PTR}$=8*100/$H\_att$ as for Ku band (8*25/H_att as for S band).

Table 6.1: Value derived from the RA-2 on ground characterization

	Ku band	Ku band (dB)	S band	S band (dB)
Pp	60 Watt	17.782 dBW	60 Watt	17.782 dBW
A_R		1.265 dB (*)		1.4234 dB (**)
P_{PTR_REF}		-10.16		-9.003
A_{CAL_FEE}		98.99		99.17
AGC_{PTR_REF}		54.851		52.801
G_{SPSA}	800/H_att*G'$_{SPSA}$		200/H_att*G'$_{SPSA}$	
G_{TX_RX}		167.456 dBW (***)		160.717 dBW (****)

(*) A_R (Ku)=A_1+A_2+A_4'=.14+.051+1.074=1.265 dB
(**) A_R (S)= A_1+A_2+A_4'=.6524+.771=1.4234 dB
(***) G_{TX_RX}(Ku)=-10.16+98.995+54.851+23.770=167.456
(****) G_{TX_RX} (S)=-9.003+99.17+52.801+17.7490=160.717

From these values the following nominal gains were derived before launch:

$G_{RX}\big|_{dB} = G_{TX\_RX} - P_p - A_R = 167.46 - P_p - A_R = 167.456 - 17.782 - 1.265 =$ **148.4**09 **dB** for Ku band

$G_{RX}\big|_{dB} = G_{TX\_RX} - P_p - A_R = 160.70 - P_p - A_R = 160.717 - 17.782 - 1.4234 =$ **141.5**12 **dB** for S band

6.2 The calibration approach

6.2.1 RA-2 internal calibration

During PTR calibration of the receiver operating on board, the output of HPA is directly injected into the receiver through the FEE, and the resulting I&Q complex samples *X(k)* are then processed on ground through the module PTR_{PROC}, so that the following scheme is applicable,:

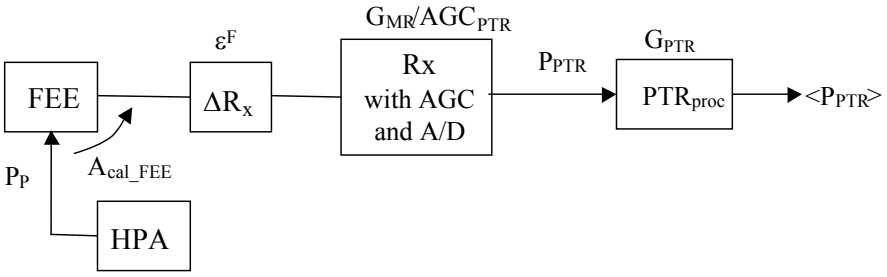

Fig.6.7 Scheme of the RA-2 during in-flight PTR calibration.

The variable component of the receiver gain is computed continuously by averaging a number of PTR measurements and then dividing the two values (i.e., $<P_{PTR}>$ and P_{PTR_REF}) scaled for the different values of AGC (i.e., AGC_{PTR} and AGC_{PTR_REF}) during the two (pre-flight and in-flight) calibration conditions. The following equation is therefore applied:

$$\varepsilon^F = \left\langle \frac{P_{PTR}}{G_{MR}G_{PTR} / AGC_{PTR}} \middle/ \frac{P_{PTR\_REF}}{G_{MR}G'_{SPSA} / AGC_{PTR\_REF}} \right\rangle = \left\langle \frac{P_{PTR}AGC_{PTR}}{P_{PTR\_REF}AGC_{PTR\_REF}} \right\rangle \frac{G'_{SPSA}}{G_{PTR}} \tag{6.16}$$

Note that in doc. TNO/RAS/0018/ALS it is assumed $G'_{SPSA}/G_{PTR}=1$, that is processing during pre-flight characterization is considered identical to PTR processing performed in the Level 1B processor, as already stated.

By introducing $A_4=A_4'A_4''$, using ε^F computed as above and substituting eq. 6.13 into eq. 6.9 we obtain the following expression for *P(k),* that is the equation to be inverted to obtain σ°:

$$P(k) = \frac{\lambda^2 G_A^2 c\sigma^0}{4(4\pi)^2 h^3 \left(1+\frac{h}{R_e}\right)^3 B_{chirp}} \frac{\varepsilon^F}{A_4(A_2A_1)^2 AGC} G_{Tx-Rx} \cdot W(k) \tag{6.17}$$

6.2.2 The receiver gain calibration equation using the passive approach

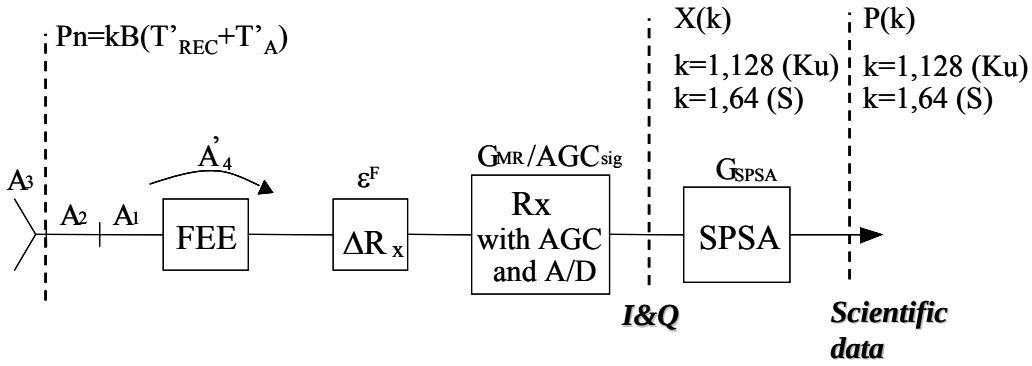

Fig.6.8 Scheme of the RA-2 during Passive calibration.

During Passive calibration, RA-2 detects only the noise that comes from the receiver, from the lossy antenna and the incoherent radiation emitted by the external scenario, as depicted in figure 6.8. The former kind of radiation is commonly described by the Brightness Temperature T_B. The equivalent temperature T_A (the Antenna Temperature) of a resistor producing the same amount of noise at the output of an ideal (lossless) antenna is given by:

$$T_A = \frac{1}{4\pi}\iint_{4\pi} T_B(\theta,\varphi)D(\theta,\varphi)d\Omega = \eta_{ML}T_{BML} + (1-\eta_{ML})T_{BSL} \tag{6.18}$$

where η_{ML} is the main lobe efficiency (describing the angular discrimination of the antenna), T_{BML} is the brightness temperature coming within the main lobe, T_{BSL} is the mean brightness temperature coming from outside the main lobe and T_0 is the antenna physical temperature. The corresponding mean available power is given by kT_AB, where k is the constant of Boltzmann and B is the bandwidth of the signal collected by the receiver,

If the antenna exhibits losses and we indicate with η_l its radiation efficiency, the equivalent temperature at the output of a real antenna is:

$$T_A^{'} = \eta_l T_A + (1-\eta_l)T_0 = \eta_l \eta_{ML} T_{BML} + \eta_l (1-\eta_{ML}) T_{BSL} + (1-\eta_l)T_0 \tag{6.19}$$

When accounting for the receiver additional noise by using the input noise equivalent temperature T'_{REC}, the mean power available at the input of the receiver is $k(T'_A + T'_{REC})B$ and therefore the mean power at the output of the receiver, according to figure 6.8, is given by:

$$< P_n >= \frac{G_{RX}}{AGC_{pass}} kB\eta_l \eta_{ML} T_{BML} + \frac{G_{RX}}{AGC_{pass}} kB\left[\eta_l (1-\eta_{ML}) T_{BSL} + (1-\eta_l)T_0 + T_{REC}^{'}\right] \tag{6.20}$$

where the AGC setting during passive operations of the altimeter has to be considered (AGC_{pass}). This is the fundamental equation for *Passive Calibration*. The relationship between P_n and T_{BML} is linear, provided all the other quantities are constant. It can be seen from the equation that if the RA-2 is capable to observe different scenarios producing different T_B values in the direction of the main lobe, the output power changes. Therefore, the slope of the line can be estimated in the P_n - T_{BML} plane if an evaluation of T_{BML} from the target producing a given $<P_n>$ can be done in some way (for example by electromagnetic modeling). The precision of the slope estimates depends on the number of available measurements. Considering the high degree of fluctuation affecting the altimeter output because of the limited bandwidth of the instrument and the high degree of uncertainty in the evaluation of the T_{BML}, a large number of observations is required to achieve a good precision.

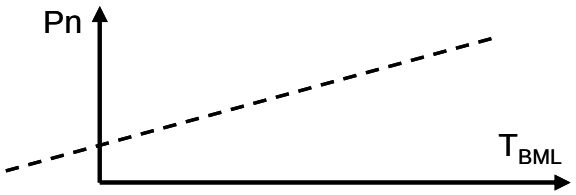

Fig. 6.9 The relationships between mean output power and input TB within the RA-2 mainlobe can be assumed linear if a number of parameter in eq. 6.20 remain constant

Simply speaking, if we observe targets whose difference in T_B is ΔT_{BML} and the corresponding difference in output power is $\Delta<P_n>$, the following ratio can be in principle evaluated:

$$\frac{\Delta < P_n >}{\Delta T_{BML}} = \frac{G_{RX}}{AGC_{pass}} kB\eta_l \eta_{ML} \tag{6.21}$$

Then the receiver gain can be computer, provided the AGC setting and some instrument parameters are known:

$$G_{RX} \approx \frac{\Delta < P_n >}{\Delta T_{BML}} \frac{AGC_{pass}}{kB\eta_l \eta_{ML}} \tag{6.22}$$

A better approach consists in observing several targets whose T_{BML} is known and considering a linear regression technique for estimating the slope of the straight line in Fig. 6.9. This is required to improve precision in the slope estimation.

An important limitation of the technique is the lack of reliable information on the instrument parameters present in eq. 6.20 due mainly to the fact that this type of analysis was not foreseen before the ENVISAT design and that not suitable ground characterizations (i.e., antenna efficiency) nor data acquisition (i.e., antenna physical temperature) have been planned. In particular, the assumptions about η_l, η_{ML} are probably not reliable and very crude. Moreover, we do not monitor T_0 and therefore both T_0, and T'_{REC} have to be assumed constant.

6.2.2 Antenna efficiency

In order to have an idea of the antenna efficiencies, we were able to rely on few measurements of the antenna gain performed on ground. Unfortunately, these measurements were available only for a limited range of directions around the antenna boresight (about eight degrees), whilst the knowledge of the mainlobe efficiency and of the antenna losses would require the measurements of the complete antenna pattern, including sidelobes. We have therefore taken the

following approach. Since the antenna efficiency η_l (accounting for antenna losses) is the ration between gain and directivity of the antenna and the integral of the directivity over all the direction (4π solid angle) is equal to 4π, the integral of the gain equals $4\pi \cdot \eta_l$. Moreover, the main lobe efficiency is the integral of the directivity within the main lobe of the antenna (-3dB main lobe) whose angular amplitude is indicated with Θ_{-3dB}. If we perform the integration of the available measurements of the gain for increasing values of the elevation angle θ (e.g., the angle with respect to the antenna boresight direction) we obtain:

$$\eta_\Theta(\Theta) = \frac{1}{4\pi}\int_{\varphi=0}^{2\pi}\int_{\theta=0}^{\Theta} G(\theta,\varphi)d\Omega \tag{6.23}$$

By extending the integration to π or to Θ_{-3dB} we obtain, respectively:

$$\eta_\Theta(\pi) = \frac{1}{4\pi}\int_{\varphi=0}^{2\pi}\int_{\theta=0}^{\pi} G(\theta,\varphi)d\Omega = \eta_l \qquad \eta_\Theta(\Theta_{-3dB}) = \eta_l\eta_{ML} \tag{6.24}$$

By using the available antenna pattern measurements, we were able to compute the integral for elevation angles up to 8 degrees as for Ku band (14 degrees for S band). The resulting plots of $\eta_\Theta(\Theta)$ are reported in figure 6.10, which shows an asymptotic behavior for increasing Θ, providing us with the value of the antenna radiation efficiency. From this figure it comes out that a reasonable value for $\eta l \eta_{ML}$ can be 0.7 for Ku band and 0.68 for S band.

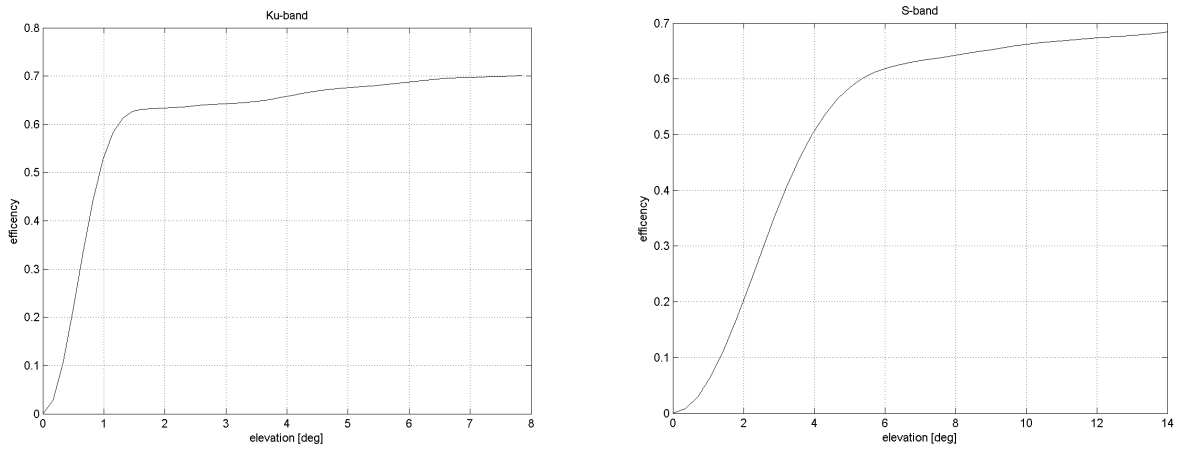

Fig. 6.10: Plots of $\eta_\Theta(\Theta)$ as function of Θ, derived from the available measurements of the antenna gain for Ku-band (left panel) and S-band (right panel) antennas.

6.2.3 Influence of sensor temperature

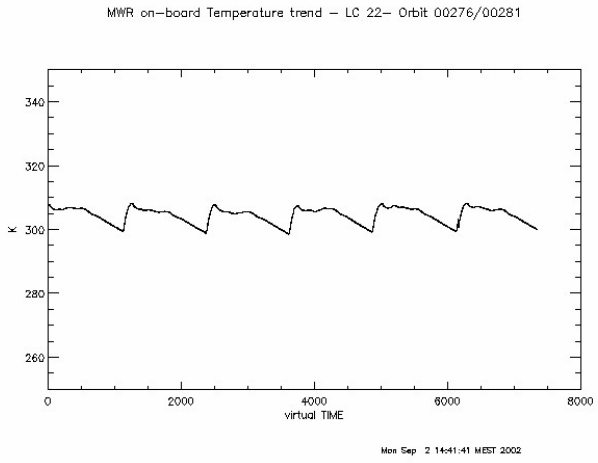

Fig. 6.11: Plots of MWR antenna physical temperature as function of time

Changes in the RA-2 antenna physical temperature must be neglected for the purpose of passive calibration since no measurements were made on board. In order to have an idea of this variability, we report in Figure 6.11 the temperature of the MW radiometer antenna on board of Envisat as function of time. The orbital thermal cycle can be easily

recognized and its dynamical range is in the order of 5-6 K. This data can not be used for our purpose, since the two antennas are located in different positions, but they can give an idea of the expected variability along the orbit. In eq. 6.20 this variation is multiplied by $1-\eta \cong 0.3$ and must be compared with T_{REC} which may be in the order of hundreds of K, so that it contribute to the bias of the regression line with fractions of percent (0.2-0.3 %).

6.3 Overview of RA-2 acquisitions for "Passive calibration"

An overview of the acquisition of RA-2 in "noise listen mode" is given in Fig. 6.12, where the boxes limiting the acquisition areas are reported on a map. A catalog of the acquisitions has been maintained updated during the projects to store or relevant information to be exchanged among participants. This catalog is reported in Appendix A.2.

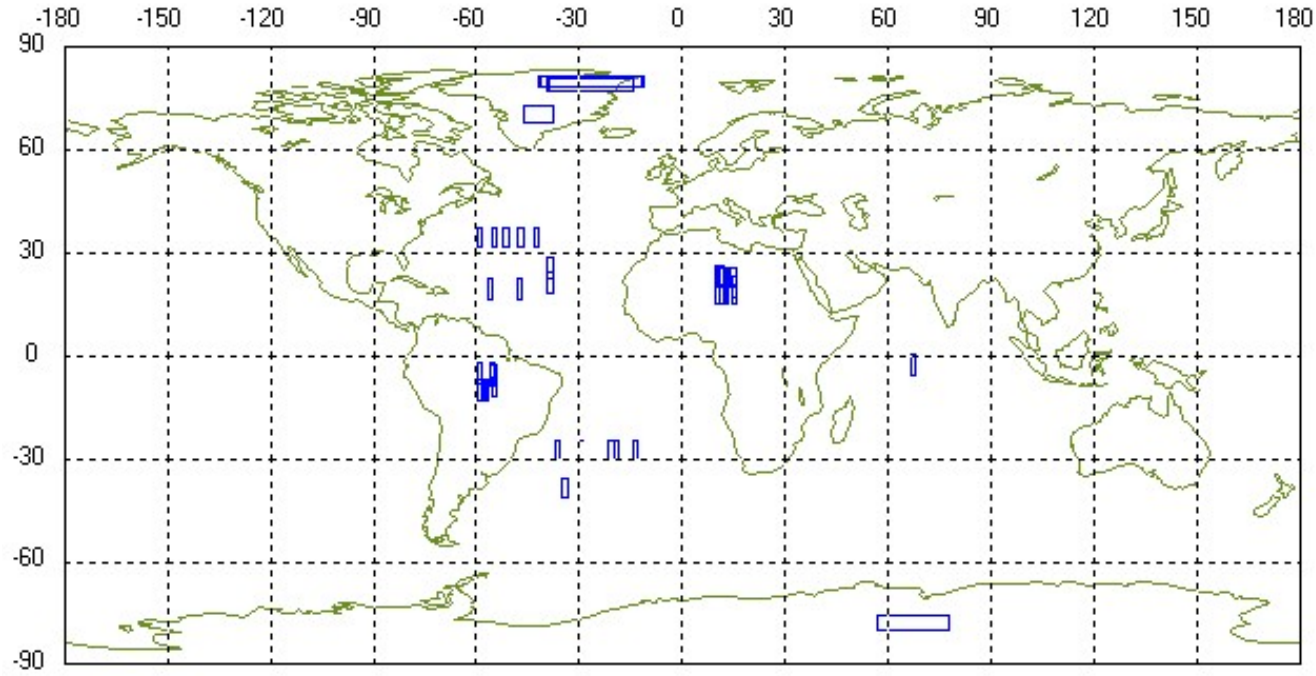

Figure 6.12: Boxes delimiting the acquisitions for Passive Calibration during the Commissioning phases and processed during the project

The summary of the number of available and processed acquisitions is reported in Table 6.2 for each calibration site. A rough idea of the time delay of RA-2 acquisitions with respect to the collection of other relevant data used in the simulation and calibration procedures is also indicated. The delay with respect to ECMWF data used for simulating the T_{ML}, as well as the time delay of radiometer measurements used for validating the simulations are both very interesting. For this reason, we have also computed the statistics of such delays and the histogram is presented in Fig. 6.13. It can be observed that the time differences can be considered acceptable in most cases. The most critical aspects are the cloudy conditions over ocean since clouds generally move very quickly and simulations might become erroneous. The quick change of the surface temperature of the Sahara Desert may also represent a problem, especially for simulation around dusk or down. These aspects have been already discussed in the relevant sessions concerning simulation models.

ESA has provided us with data acquired from RA-2 in PRESET LOOP mode, when the altimeter echo was not detected. Such data were extracted from Level 0 products and made available in a standard format. We have averaged all the 128 (for Ku band) and 64 (for S band) samples of each waveform and then we have further averaged this values within a time interval of T=1.114 sec (corresponding to 200 science data block). The total number of averaged samples is therefore equal to N_C=128x2000 at Ku band (N_C=64x2000 at S band). The *AGC* setting (AGC_{pass}) was continuously read from the data file.

The RA-2 data have been geo-located using a single state vector available in the ESA file. The Envisat orbit propagator has been used for this purpose and the latitude and longitude of each RA-2 sample have been appended to each RA-2 passive waveform. The geographical window where the RA-2 has collected the environmental noise has been also included in the catalog. The location information has been passed to the people involved in the data collections task. They have collected all the required input data to run the models and in particular the ECMWF analysis and/or forecast within the relevant geographical window closest in time to the RA-2 acquisition. At the same time, data from DMSP-SSM/I and TRMM-TMI have been also collected on the same geographical window and their T_B measurements have been co-located with respect to each RA-2 measurement. Of coarse, time of RA-2 acquisitions were not coincident with both geophysical data and measurements from spaceborne radiometer (with the exception of only few data available from MWR on board of Envisat). The RA-2 data timing and location, the geophysical data and co-located data from spaceborne radiometers have been merged in a formatted file and passed to the groups involved in

atmospheric, land and sea modeling of radiative parameters and T_{BTOA}. The atmospheric model were run at first to produce atmospheric opacity and mean radiative temperature needed to account for atmospheric effects.

Figure 6.14) gives a picture, from functional point of view, of the processing procedures we have implemented and applied to each Passive acquisition. Some details about the data sets produced by the procedure and their formats are reported in Appendix A.3.

Table 6.2: AN overview of the number of acquisition in the different calibration sites and the time delay with respect to reference data

	N° of acquisitions	N° of processed acquisitions	N° of CLS-MWR data	SSMI delay [min]	TMI delay [min]
OCEAN	23	20	5	30 < T < 90	30 < T < 90
SAHARA	13	0	n/a	30 < T < 90	30 < T < 120
AMAZONIA	7	5	n/a	30 < T < 60	90 < T < 180
CONT. ICE	14	0	n/a	/	/
Others (n/a)	14	n/a	n/a	/	/

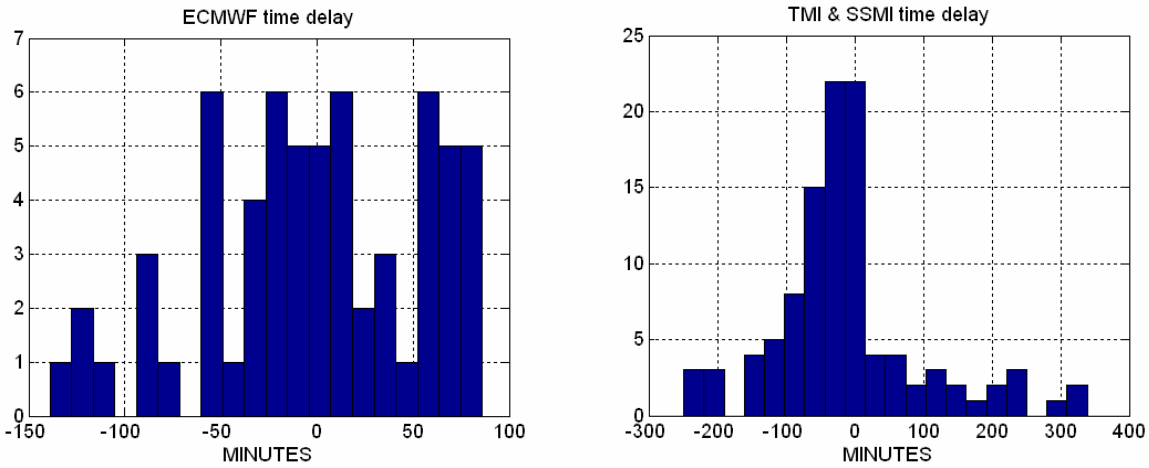

Figure 6.13: histograms of time delays of ENVISAT overpasses with respect to time of ECMWF analysis and/or forecasts, whatever have been selected (left panel) and to time of SSM/I and/or TMI overpasses (right panel)

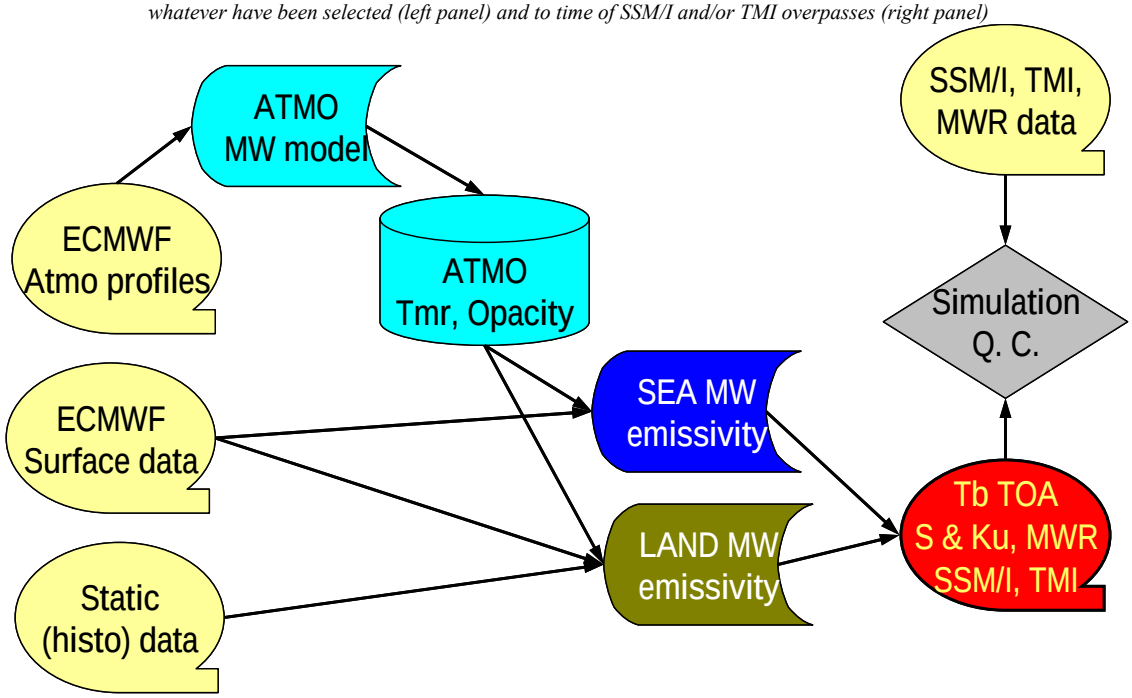

Figure 6.14: A simplified functional scheme and data flow of the procedure applied to each RA-2 data set

6.4 The RA-2 passive signature of calibration targets

It is interesting to summarize the overall dynamic range of the RA-2 measurements in Noise Listen mode acquired during the Commissioning Phase. This is sketched in figure 6.15, where we report the values of the Digital Counts in

Ku-band as function of those in S band, both averaged on an entire source packet (1.114 sec). It can be noted the fairly sensible dynamic range among ocean data (lowest values) and data over land (highest values). It is interesting to note the behavior of the intermediate values corresponding to ice covered surfaces and the greater dynamic range in Ku band with respect to S band with change in latitude. This was due to the high penetration depth at S band that make the observed ice layer deeper and less sensitivity to the surface temperature than the observation at Ku band. This aspect has an impact on the simulations and has been discussed in the relevant section.

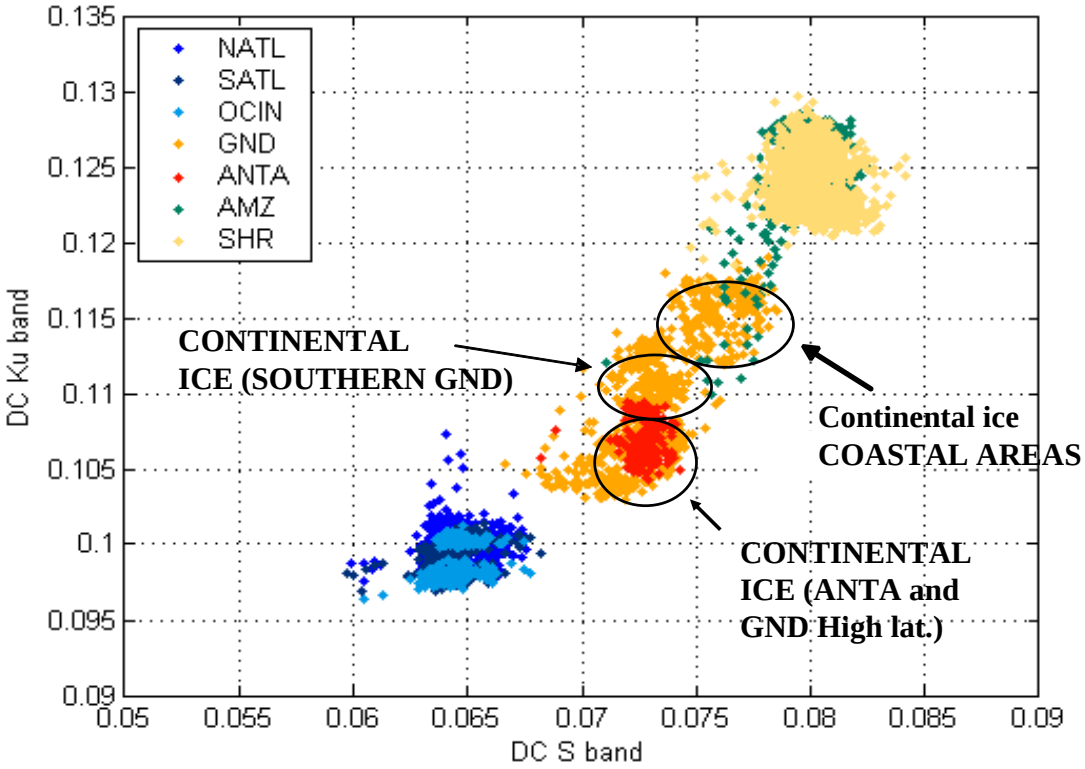

Figure 6.15: RA-2 Digital Counts in Ku-band as function of those in S band, both averaged on an entire source packet (1.114 sec)

6.5 Estimates of RA-2 receiver gains

6.5.1 Introduction

This section reports the final estimation results of the receiver gain as for Ku band and S band. As already discussed, from eq. 6.20 it is apparent that some parameters have to be considered constant whilst other parameters must be known. The parameters to be considered constants are those affecting the intercept of the calibration line, that is T'_{REC}, T_0 and T_{BSL}. The parameters to be known are those include in eq. 6.21, that is k, B, η_l, η_l. As for the latter set of parameters, we have considered the results in section 6.2.2 and the fact that the bandwidth of each sample of the waveforms is associated to the resolution of the FFT performed on board and is therefore equal to 50 kHz. Table 6.3 summarizes the values we have adopted for these parameters. The table also report the values of the AGC that have been maintained equal during all the Passive acquisition. They were derived from the look-up-table in the applicable document PO-TR-ALS-RA-0042 and from the values read in the data files (AGC1=0, AGC2=5) corresponding to 4.595 dB at Ku band. As for S band, a scaling (decreasing) factor of 4 dB must be applied to the nominal on board AGC setting before entering into the look-up table.

Table 6.3: Values of parameters to be used in eq. 6.21

Parameter	***Description***	***value***
k	Constant of Boltzmann	$1.3806\ 10^{-23}$ JK^{-1}
B	Receiver Bandwidth	50 kHz
$\eta_l \cdot \eta_l$	Product of antenna and mainlobe efficiencies	0.7 at Ku band 0.68 at S band
AGCpass Ku	AGC setting in Noise Listen Mode at Ku band	4.595 dB 2.880713
AGCpass S	AGC setting in Noise Listen Mode at S band	0.875dB 1.2232

6.5.1 Ku band

In figure 6.15 we have plotted the Digital Counts at Ku band averaged on the entire source packet as function of the simulated values of the brightness temperature T_{ML} for the observed field of view. Few data points have been discarded at the beginning of each data set or where they appeared to be not reliable and too much far from the regression line.

The estimated regression line was given by:

$$\overline{P}_n = 1.66911 \cdot 10^{-4} \cdot T_{BML} + 7.82877 \cdot 10^{-2} \tag{6.25}$$

In other words, the slope of the line was:

$$\frac{\Delta \overline{P}_n}{\Delta T_{BML}} = 1.66911 \cdot 10^{-4} \tag{6.26}$$

From which we derived the wanted gain of the receiver, both in linear and in decibel scales, using eq. 6.22:

$$G_{RX} \approx \frac{\Delta \overline{P}_n}{\Delta T_{BML}} \frac{AGC_{pass}}{kB\eta_l} \quad \Rightarrow \quad G_{RX}\big|_{dB} \approx 149.978 \text{ dB} \tag{6.27}$$

From the regression analysis we can estimate also the standard deviation of the slope estimation. This was given by:

$$\sigma_{\Delta \overline{P}_n / \Delta T_{BML}} = 2.8 \cdot 10^{-7} \tag{6.28}$$

If we assume in the regression an error on the independent variable T_{BML} equal to 5 K, the estimated slope of the line slightly increase to 1.67651 and the gain become G_{RX}=149.998 dB with a standard deviation in the order of 1.7 10^{-7}.

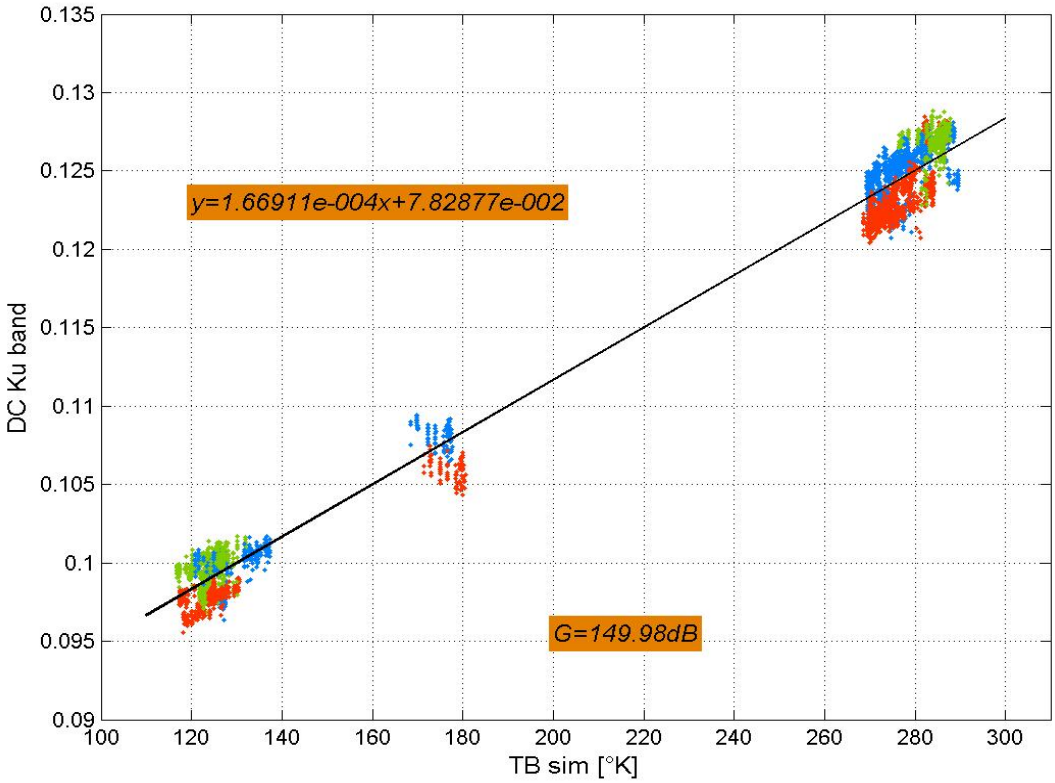

Figure 6.15: the calibration line for Ku band. Green, blue and red points refer to October, November/December and March acquisitions, respectively

6.5.2 S band

In figure 6.15 we have plotted the Digital Counts at Ku band averaged on the entire source packet as function of the simulated values of the brightness temperature T_{ML} for the observed field of view. Few data points have been discarded at the beginning of each data set or where they appeared to be not reliable and too much far from the regression line.

The estimated regression line was given by:

$$\overline{P}_n = 9.779931 \cdot 10^{-5} \cdot T_{BML} + 5.35654 \cdot 10^{-2} \tag{6.29}$$

In other words, the slope of the line was:

$$\frac{\Delta \overline{P}_n}{\Delta T_{BML}} = 0.977993 \cdot 10^{-4} \tag{6.30}$$

From which we derived the wanted gain of the receiver, both in linear and in decibel scales, using eq. 6.22:

$$G_{RX} \approx \frac{\Delta \overline{P}_n}{\Delta T_{BML}} \frac{AGC_{pass}}{kB\eta_l} \quad \Rightarrow \quad G_{RX}\big|_{dB} \approx 144.06\text{dB} \tag{6.31}$$

From the regression analysis we can estimate also the standard deviation of the slope estimation. This was given by:

$$\sigma_{\Delta \overline{P}_n / \Delta T_{BML}} = 2.2 \cdot 10^{-7} \tag{6.32}$$

If we assume in the regression an error on the independent variable T_{BML} equal to 10 K, the estimated slope of the line slightly increase to 0.994927 and the gain become G_{RX}=144.13 dB with a standard deviation in the order of 1.9 10^{-7}.

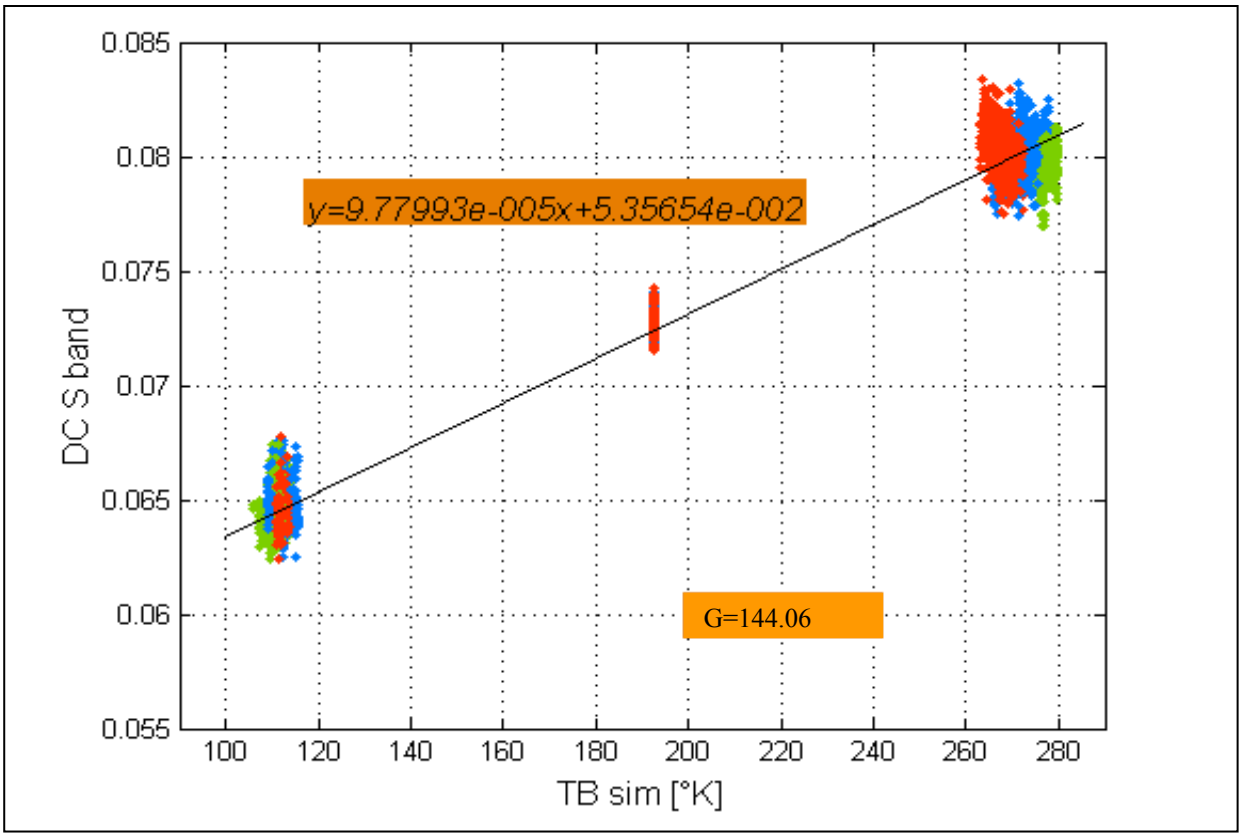

Figure 6.15: the calibration line for S band. Green, blue and red points refer to October, November/December and March acquisitions, respectively

6.6 Bias Definition

The σ^0 bias in dB is defined as the difference between the nominal sigma naught derived from RA-2 characterization and internal calibration (no external calibration applied) and the true value of sigma naught. The following equation applies:

$$\Delta\sigma^0{}_{Cal} = \sigma^0{}_{nom} - \sigma^0{}_{true} \tag{6.33}$$

where $\Delta\sigma^0{}_{Cal}$ is the sought bias, $\sigma^0{}_{nom}$ is the nominal value of σ^0 and $\sigma^0{}_{true}$ is the perfectly calibrated value (true value) of σ^0.

Since σ^0 is inversely proportional to the receiver gain G_{MR} (cfr equation 6.9), it is easy to see that, assuming the receiver gain is the only undetermined factor in the radar equation 6.9, the σ^0 bias in dB units is also given by the following equation:

$$\Delta\sigma^0{}_{Cal} = G_{MR}{}^{true} - G_{MR}{}^{pre\text{-}flight} - \varepsilon^F \tag{6.34}$$

with obvious meaning for the parameters $G_{MR}{}^{true}$ and $G_{MR}{}^{pre\text{-}flight}$, whilst the receiver gain variation ε^F is derived by the PTR calibration as described in section 6.1..

It is worth mentioning that the σ^0 values in the ENVISAT products might not be computed with the exact the pre-flight values, and this can be seen by the different value of the parameter G_{Tx_Rx} annotated in the product with respect to the real pre-flight value (cfr par. 6.1). For any information regarding the actual content and calibration approach in the ENVISAT products and related reports see the relevant ESA documents and the EO Product Control Service (PCS) web site at http://earth.esa.int/pcs/envisat/ra2/reports/pcs_cyclic/ (rif. ENVI-GSOP-EOPG-03-0011).

6.7 Error budget for gain estimation

The source of error affecting the Passive Calibration and the estimation of receiver gain can be separated into different classes:

A. Errors due to the fluctuations affecting the Digital Counts detected by RA-2
B. Random errors in the simulation of brightness temperatures observed by the radiometer (assumed with zero mean)
C. Systematic errors in the simulation of brightness temperatures observed by the radiometer (i.e., biased with respect to the real values)
D. Errors in the values of system parameters introduced for estimating the gain (e.g., antenna efficiency)
E. Variations in the system parameters that have been assumed constant during the commissioning phase (e.g., T'_{REC})

We have analyzed the effect of such errors separately and then a combined analysis has been performed.

As far as errors of class A are considered, they can be dealt on the bases of the standard regression theory. If we have to estimate the relation between a dependent variable y and an independent variable x (the *predictor*) in the form $y=ax+b$ and the N available observations of quantity to be predicted y_i are affected by errors each one with standard deviation σ_i, the estimation of the slope of the regression line a is also affected by and error with zero mean and standard deviation equal to (Press et al., 1986):

$$\sigma_a = \frac{S_{xx}}{SS_{xx} - (S_x)^2} \qquad S = \sum_{i=1}^{N} \frac{1}{\sigma_i^2} \quad S_{xx} = \sum_{i=1}^{N} \frac{x_i^2}{\sigma_i^2} \quad S_x = \sum_{i=1}^{N} \frac{x_i}{\sigma_i^2} \tag{6.35}$$

This standard deviation, which measures the precision of our estimate of the slope, is related to the number of available observations, their errors and their dynamic range. In our case, we found small values of σ_a, in the order of $2\ 10^{-7}$ with respect to a value of about $1\ 10^{-4}$ at Ku band ($2.8\ 10^{-7}$ with respect to $1.7\ 10^{-4}$ at S band). This would results in an uncertainty of the estimated receiver gain in the order of 0.2% that in decibel units corresponds to $10*\log(1+\sigma_a/a) \cong 0.009$ dB.

Considering errors of type B, it is worth reminding that the common regression formula assumes the observations of the independent variable (T_{BML} in our case) are not affected by errors. If the predictors x_i are also affected by random errors, we have to use a non standard regression technique in order to avoid biased estimation of the coefficients a and b. (Press et al., 1986). This is depicted in Fig. 6.15, where errors in both independent and dependent variables are indicated together with their effects on the uncertainties in the regression line. In the previous paragraphs this technique has been used by assuming random errors for simulations of T_{BML} with zero means and standard deviation equal to 5 K and 10 K for Ku band and S band, respectively.

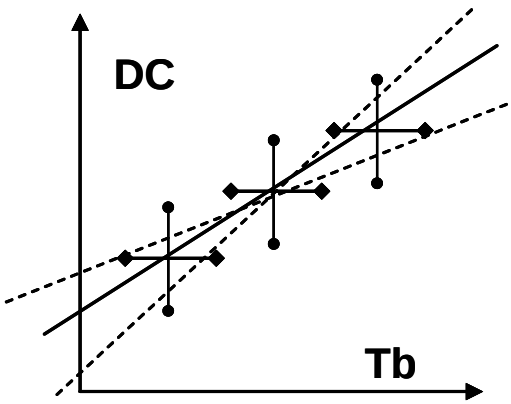

Figure 6.16: a sketch to show the effects of errors on Tb simulation on the slope of the regression line (i.e., the gain)

Errors of class C are difficult to model. They can be due to systematic errors in the radiative model and/or in the input data used by the model itself. It is obvious that if a systematic bias affects all data points this will not affect the estimation of the slope, but only of the calibration line intercept. Conversely, the worst case is represented by opposite biases for the simulations of the highest and lowest values of the T_{BML}. Moreover, it is difficult to discriminate between errors of class B (random) and class C (systematic). The paragraph dealing with modeling methods have indicated possible errors for the simulations. Since for a random variable ε the expected value of its square $<\varepsilon^2>$, the expected value $<\varepsilon>$ and the standard deviation σ_ε are related by the equation $<\varepsilon^2>=<\varepsilon>^2+\sigma_\varepsilon^2$, we may assume the model errors indicated in the previous paragraphs for land and ocean simulations represent values of $<\varepsilon^2>$, that is the so called root mean square error (rms). Than, we assume that such rms error is splinted in the two components, the bias represented by $<\varepsilon>$ and the purely random component represented by σ_ε, each one appearing in different proportions β and 1-β, respectively ($0<\beta<1$). If the overall error associated to the model is indicated with Δ, we can synthetically generate the observations affected by both systematic and random errors in different amount by the following:

$$T_{BML}^{obs} = T_{BML} + \delta \cdot \beta \cdot \Delta + (1-\beta) Run(\Delta) \tag{6.36}$$

where δ is a variable whose values can be +1 or -1, function $Run(\Delta)$ indicates a random generation with Gaussian pdf of numbers having zero mean and standard deviation equal to 2Δ and β spans from 0 (purely random errors) to 1 (purely systematic errors). We have added this error to the simulations by considering increasing value of the rms error Δ from 0 to 10 K. In order to account for different sharing between random and systematic errors, for each Δ we have considered one thousand different values of β with uniform pdf between 0 and 1. Each value of β has yield a different slope a and its standard deviation has been computed from the 1000 estimates. As far as values of δ were concerned, they have been set to values either δ=+1 for land surface and δ=-1 for sea surface (implying gain underestimation) or δ=–1 for land surface and δ=+1 for sea surface (implying gain overestimation). Moreover, the more favorable case of δ assuming the two values +1 and -1 with equal probability and with statistical independence among sea and land has been also considered. For each set of pairs β, δ, statistical independent samples of $Run(\Delta)$ have been added to all the data points.

The ratio, in decibel units, between the slope of the regression line computed in the presence of errors and the nominal value found in the previous paragraph is reported in Fig. 6.17 as function of Δ. In order to quantify the effect of the two types of errors on the bias of the final estimation of the slope, three cases have been considered: purely random errors on T_{BML} (β=0), purely systematic errors on T_{BML} (β=1), mixed case (β randomly generated with uniform distribution between 0 and 1). We can see that the random errors on T_{BML} cause an underestimation of the gain. In the previous paragraphs we have partially limited this error by making an hypothesis on the random component of the simulation error. Systematic errors produce appreciable effects on the estimated slope only in the pessimistic case in which land simulations are always overestimated whilst sea simulations are underestimated (and vice versa). We can conclude that the systematic errors on the final estimation of the receiver gain is in the order of few tenth of dB for all the situations we can envisage. The underestimation due to random error can be mitigated (and even made zero) by making assumptions on the amount of these errors within a proper regression algorithm, as done in the previous paragraphs.

In order to quantify the effect of the two types of errors (B and C) on the uncertainty of the final estimation of the slope, the standard deviation σ_a divided its nominal value a as function of Δ is reported in Fig. 6.18 in decibel units ($10*\log(1+\sigma_a/a)$) for the same three cases: purely random errors on T_{BML} (β=0), purely systematic errors on T_{BML} (β=1), mixed case (β randomly generated with uniform distribution between 0 and 1). The random uncertainty on the receiver gain due to random errors on the simulations is very small because of the large number of data points we had for the computation. Conversely, systematic errors may lead to standard deviation of the slope in decibel units reaching 0.4 dB.

The "mixed" and more realistic case leads to an error of 0.25 dB in the worst case of simulations affected by a 10 K rms error (that may represent the S band case), whilst the error is in the order of 0.15 dB as for simulation rms error equal to 5 K (that may represent the Ku band case).

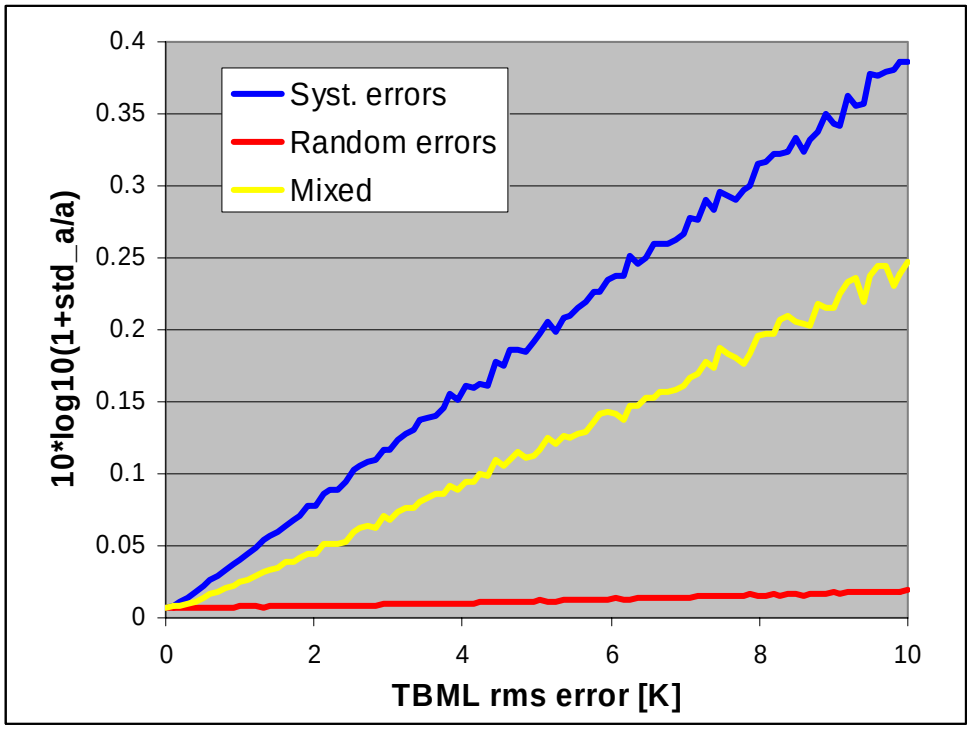

*Figure 6.17:Standard deviation of the estimated slope σ_a compared to nominal value a in decibel units (10*log(1+ σ_a/a)) as function of the rms error Δ of T_{BML} simulations for purely random errors (β=0), purely systematic errors (β=1) and mixed case (β random with uniform distribution between 0 and 1)..*

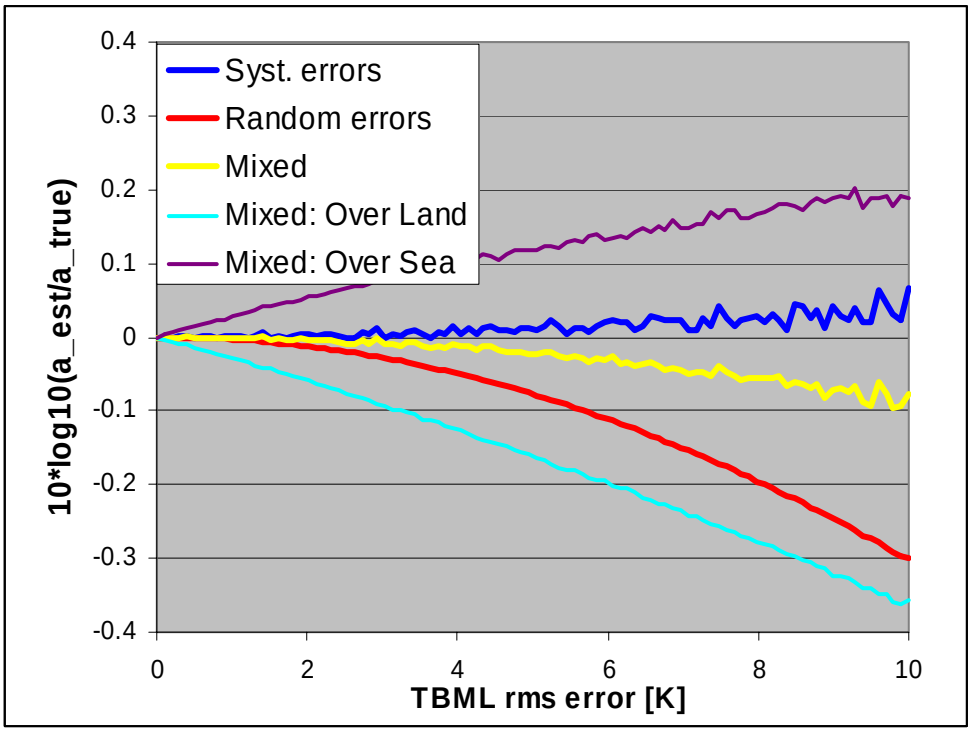

*Figure 6.18:Systematic error on estimated slope in decibel units (10*log(Estimated slope/Nominal slope)) as function of the rms error of T_{BML} simulations for purely random case (β=0), purely systematic case (β=1) and mixed case (β random, with uniform distribution between 0 and 1). Two additional curves represent the mixed case with all land simulations being overestimated (δ_land=+1 δ_sea=-1: "Ovel Land") and with all sea simulations being overestimated (δ_land=-1 δ_sea=+1: "Over Sea")*

As far as errors of type C are concerned, since the system parameters introduced for estimating the gain are all multiplicative factors, their relative error reflects directly on the relative errors on the estimated gain. Considering that the more questionable factor is the antenna efficiency, from Fig. 6.10 we can assume a possible uncertainty in the range 0.67-0.70 for Ku band and 0.65-0.68 for S band. This means a relative errors of 3÷4 % and therefore an error in dB units of 10*log(1+0.03÷0.04)=0.13÷0.17 dB

Finally, variations in the system parameters that have been assumed constant during the commissioning phase (errors of type D) can be reasonably assumed uncorrelated with respect to T_{BML}; according to equation 6.20 the only exception could be the side lobe temperature T_{BSL}. Therefore these variations contribute to the random fluctuation of the DC counts and have been already included in the computation of σ_a.

6.8 Overall error budget for sigma naught estimation

In the previous paragraph we have analyzed different sources of errors that affect the estimation of the receiver gain. The conclusion is that the expected error is in the order of few tenth of dB (say 0.3 dB). In order to compute the sigma naught, it must be considered that the radar equation (eq. 6.8) contains further parameters to be accounted for, thus other sources of errors. In order to give a rough indications of the overall accuracy of the calibration we have to introduce these errors. Table 6.4 resumes the value of errors affecting each parameter we have considered here. When possible they were based on what found in the applicable documents. In other cases they are only presumptive figures.

By combining the errors in dB of each parameter χ trough the summation of their square values, we found the figures in the last line of the table as for the precision of the sigma naught calibration.

$$\Delta\sigma^{\circ}\big|_{dB} = \sqrt{\sum \left(\Delta\chi\big|_{dB}\right)^2} \tag{6.37}$$

Table 6.4: Presumptive values of parameter errors for error budget

	Nominal Value Ku band	Nominal Value S band	Error Ku band	Error S band
Antenna gain G_A	42 dB	29.3 dB	0.15 dB PO-TR-ALS-RA-0042	
FEE Attenuations A_R	1.265 dB	1.4234 dB	0.05 dB	
Transmitted Power P_p	60 W	60 W	2 Watt, 3%, 0.14 dB	
Receiver gain G_{RX}	*From Passive Cal*	*From Passive Cal*	0.2 dB	0.3 dB
Chirp Bandwidth B_{chirp}	320 MHz	160 MHz	.5 MHz, 0.16%, .007 dB	0.5 MHz, 0.3%, 0.014 dB PO-TR-ALS-RA-0042
Flight elevation h	*measured*	*measured*	0.01%, 0.0005 dB	
Sigma naught σ°			0.29 dB	0.37 dB

6.9 Interfrequency bias

The estimation of the difference of the receiver gain between the two bands is more insensitive to unaccounted parameters with respect to the individual calibration of each band. In fact, most of the relevant parameters needed for the calibration can be assumed very similar in the two channels (same output power, similar antenna efficiency, same antenna physical temperature, ecc.) and therefore vanish when the ratio between $\sigma^{\circ}(Ku)$ and $\sigma^{\circ}(S)$ is performed (difference in decibel units). Then, we may be interested in evaluating the interfrequency bias which is defined as in the following (σ° values are in dB):

$$IFB = \left[\sigma^0_{true}(S) - \sigma^0_{true}(Ku)\right] - \left[\sigma^0_{nom}(S) - \sigma^0_{nom}(Ku)\right] = \left[\sigma^0_{nom}(Ku) - \sigma^0_{true}(Ku)\right] - \left[\sigma^0_{nom}(S) - \sigma^0_{true}(S)\right] \tag{6.38}$$

where subscripts "*true*" and "*nom*" indicate the values of the absolutely calibrated sigma naught and of the nominal one, respectively. Based on eq. (6.34) introducing the pre-fligth data, in the hypothesis the receiver gain is the only undetermined factor, it comes out (gains are in dB) :

$$\begin{aligned} IFB &= [G_{MR}{}^{true}(Ku) - G_{MR}{}^{nom}(Ku)] - [G_{MR}{}^{true}(S) - G_{MR}{}^{pre\text{-}fligth}(S)] = \\ &= [G_{MR}{}^{true}(Ku) - G_{MR}{}^{pre\text{-}flight}(Ku) - \varepsilon^F(Ku)] - [G_{MR}{}^{true}(S) - G_{MR}{}^{pre\text{-}fligh}(S)^t - \varepsilon^F(S)] \end{aligned} \tag{6.39}$$

From Passive Calibration we can state that the final value of IFB is:

$$IFB = 1.08\ dB \tag{6.39}$$

The associated uncertainty can be estimated from table 6.4, where the errors in the true receiver gain is the only to be retained, since the others are common factors almost vanishing when doing ratio between frequency channels. An error of 0.36 dB can be reasonably assumed for the Interfrequency bias IFB.

As soon as a reliable and complete set of transponder calibration data is collected and a more precise estimation of sigma naught is available for *Ku* band (i.e., the systematic error, or bias, affecting the nominal value) the above IFB evaluation will allow one to determine a better value of the sigma naught in *S*-band (i.e., the error affecting the nominal value).

7 CONCLUSIONS

In this report we have described the activities carried out to perform Passive Calibration of the RA-2 sigma naught during the Envisat Commissioning Phase. The project has demonstrated that the proposed method can be very valuable and the obtained results are aligned to what was expected according to pre flight and in flight calibrations. In order to validate the differences obtained with respect to nominal values, it is required to have at least a further reference for comparison. This reference can be represented by modeling of the sigma naught for different surfaces, even if models can be of course questionable. An important reference has been provided us by the calibration using an active device (transponder) performed by ESA during the Commissioning Phase for Ku channel only. It was very significant, and at some extent even surprising, how well the results of Passive Calibration for Ku band compare with those of Transponder Calibration. This is resumed in the following table 6.5, where the Passive Calibration result is reported together with the pre-flight calibration gain that must be corrected by the internal calibration (PTR) data. The residual difference among the 149.98 dB gain we have found here and the 148.41+0.7=149.11 coming from pre- and in-flight measurements almost coincides with the σ° bias of 0.95 dB found from transponder data (these figures have been derived from what reported at the last RA-2 CCVT meeting).

These results represents a valuable proof of the reliability of the technique we have developed here. As discussed in this report, it could be even improved in the future once specific data were collected on board and during ground characterization of the instrument. In summary, the following recommendation can be made:

- To envisage in the future altimeter missions the operational mode of the altimeter providing measurements of the noise (Noise Listen mode)
- To perfome a better characterization of the antenna and in particular measurements of the antenna gain in a wider range of angles ans measurement of the antenna efficiency
- To collect on board data on the physical temperature of the antenna and the guideline as well as moeasuremens of the power supplied by the transmitter

Table 6.5: Comparison of Passive Calibration results against standard ESA calibration methods. Values are in dB units

Band	*Passive Rx-Gain*	*Pre-flight Rx Gain*	*PTR (ε_F) calibration (typical)*	*Pre-flight Rx Gain corrected*	*$\Delta\sigma^0_{Cal}$ from Passive Calibration*	*$\Delta\sigma^0_{Cal}$ from Transponder Calibration*
Ku	**149.98**	148.41	+ 0.7	**149.11**	**0.87 ±0.3**	**~ 0.95**
S	**144.06**	141.51	+ 0.6	**142.11**	**1.95 ± 0.4**	**N/A**
IFB	**1.08 dB ± 0.36**					

For any information regarding the actual content and calibration approach in the ENVISAT products and related reports see the relevant ESA documents and the EO Product Control Service (PCS) web site at http://earth.esa.int/pcs/envisat/ra2/reports/pcs_cyclic/ (rif. ENVI-GSOP-EOPG-03-0011).

REFERENCES

Decker, M. T., E. R. Westwater, and F. O. Guiraud, "Experimental evaluation of ground-based microwave radiometric remote sensing of atmospheric temperature and water vapour profiles", *J. Applied Meteorology*, 17, pp. 1788-1795, 1978.

Dzura M.S., V.S.Etkin, A.S. Khrupin, M.N. Pospelov, and M.D. Raev, "Radiometers-Polarimeters: Principles of Design and Applications for Sea Surface Microwave Emission Polarimetry", Proc. IGARSS'94, IEEE N.94CH3378-7, pp. 1432-1434, 1994.

Ellison W.J., Balana A., Delbos G., Lamkaouchi K., Eymard L., Guillou C., Prigent C. (1996), "Study and Measurements of the Dielectric Properties of Sea Water". Final Report ESTEC/Contract 11197/94/NL/CN.

El-Rayes M. A., F. T. Ulaby, ``Microwave dielectric spectrum of vegetation - Part I: Experimental observations", IEEE Trans. Geosci. Remote Sensing, vol. GE-25, pp. 541-549, 1987.

Ferraro R.R., and G. F. Marks, "The development of SSM/I rain-rate retrieval algorithms using ground-based radar measurements," J. Atmos. And Oceanic Techn., vol. 12, pp.755-772, 1995Gasiewski, A.J., and D.B. Kunkee, "Polarized Microwave emission from water waves", *Radio Science*, vol. 29, n.6, 1449-1466, 1994.

Ferrazzoli P., L. Guerriero, "Emissivity of vegetation: theory and computational aspects", J. Electromagnetic Waves Applicat., vol. 10, pp. 609-628, 1996b.

Ferrazzoli P., L. Guerriero, "Passive microwave remote sensing of forests: a model investigation", IEEE Trans. Geoscience and Remote Sensing, vol. GE-34, pp. 433-443, 1996.

Fung A.K., Microwave Scattering and Emission Models and Their Applications, Artech House, Norwood (USA), 1994.

Gerard E. and L. Eymard, "Remote sensing of integrated cloud liquid water: Development of algorithms and quality control", *Radio Science*, vol. 33, N. 2, pp. 433-447, March-April 1998

Greco, B.,N. Pierdicca,…, 2002.

Hayne G.S. 1980 : "Radar Altimeter Mean Return Waveforms from Near-Normal-Incidence Ocean Surface Scattering". IEEE Trans. on antennas and propagation, Vol. AP-28, n°5, pp. 687-692

Johnson J.T., J.A. Kong, R.T. Shin, D.H. Staelin, K.O'Neill, and A. Lohanick, "Third Stokes Parameter Emission From a Periodic Water Surface", *IEEE Trans. Geosci. and Rem. Sens*., vol.31, n.5, pp. 1066-1080, 1993.

Johnson J.T., J.A. Kong, R.T.Shin, S.H.Yueh, S.V. Nghiem, and R. Kwok, "Polarimetric Thermal Emission from Rough Ocean Surfaces", *J. Electromag. Waves Appl*., Vol.8, N.1, 43-59, 1994.

Karam M. A., A. K. Fung, "Electromagnetic scattering from a layer of finite length, randomly oriented, dielectric, circular cylinders over a rough interface with application to vegetation", Int. J. Remote Sensing, vol. 9, pp. 1109-1134, 1988.

Klein L.A., and C.T. Swift, "An improved model for dielectric constant of sea water at microwave frequencies", IEEE Trans. Antenna and Prop., vol. 25, pp. 104-111, 1977.

Le Vine D. M., R. Meneghini, R. H. Lang, S. S. Seker, "Scattering from arbitrarily oriented dielectric disks in the physical optics regime", Journal of the Optical Society of America, vol. 73, pp. 1255-1262, 1983.

Lemaire D., P. Sobieski, and A. Guissard, "Full range sea surfae spectrum in nonfully developed state for scattering calculations", *IEEE Trans. Geosci.Remote Sens.*, vol. 37, pp. 1038-1051, 1999.

Liebe, H.J., "An updated model for millimeter propagation in moist air", *Radio Sci*., 20, 1069-1089, 1985.

Liebe, H.J.,G. A. Hufford, and M. G. Cotton, "Propagation modeling of moist air and suspended water/ice at frequencies below 1000 GHz", *Proceedings of the AGARD 52nd Specialists' Meeting of the Electromagnetic Wave Propagation Panel*, 3-1–3-10, 1993.

Macelloni G., S. Paloscia, P. Pampaloni, R. Ruisi, "Airborne multifrequency L- to Ka- band radiometric measurements over forests", IEEE Trans. Geosci. Remote Sensing, vol. GE-39, pp. 2507-2513, 2001.

Obligis, E, L. Eymard, and O.- Z. Zanife, "Comparison between spaceborne microwave radiometer measurements and simulations: surface model effects", Proc. of IEEE-IGARSS 2001, Sidney, Australia

Pampaloni, P., L. Guerriero, G. Macelloni, N. Pierdicca, "'SEAWIND': a physical model for simulating ocean wind measurements by means of radio polarimetry", Proc. of an International Workshop POLRAD '96 Polarimetric Radiation, ESA WPP-135, ISSN 1022-6656, August 1996.

Pandey, P.C., and R. K. Kakar, "An empirical microwave emissivity model for a foam-covered sea", *IEEE Journal of Oceanic Engineering*, 7, 3, pp. 165-140, 1982.

Pierdicca N., F.S. Marzano, L. Guerriero, and P. Pampaloni, "On the effect of atmospheric emission upon passive microwave polarimetric response of azimuthally anisotropic sea surface", J. Electromag. Waves Applic., vol. 14, pp. 355-358, 2000.

Press W.H., S. A. Teukolsky, W. T. Vetterling, B. P. Flannery, "Numerical Recipes in Fortran. The Art of Scientific Computing. Second edition", Cambridge University Press, 1986.

Rodriguez E., "Altimetry for non-Gaussian oceans: Height biases and estimations of parameters", J. Geophys. Res., vol.93, no. C11, pp. 14 107- 14 120, 1988.

Rott H., "Multispectral microwave signatures of the Antarctic ice sheet", in Microwave Radiometry and Remote Sensing Applications, edited by P. Pampaloni, Utrecht (NL), VSP Press, pp. 89-101, 1989.

Schiavon G., P. Ferrazzoli, D. Solimini, P. De Maagt, J.P.V. Poiares Baptista, "A global high-resolution microwave emission model for the Earth", Radio Science, vol. 33, pp. 753-766, 1998.

Shutko A.M., A.A. Chukhlantsev, "Microwave radiation peculiarities of vegetation covers", IEEE Trans. Geosci. Remote Sensing, vol. GE-20, pp. 27-29, 1982.

Sobieskii, P., A. Guissard, and C. Baufays, "Synergic Inversion Techniques for Active and Passive Microwave remote Sensing of the Ocean", *IEEE Trans. Geosci. and Rem. Sens*., vol.29, n.3, pp. 391-406, 1993.

Trokhimovski Y.G., G.A. Bolotnikova, V.S Etkin., S.I. Grechko, and A.V. Kuzmin, "The dependence of S-band surface brightness and temperature on wind vector at normal incidence". IEEE Trans. Geosci. and Rem. Sens., vol. 33, n.4, pp. 1085-1088, 1995.

Tsang, L., J.A. Kong, R. Shin, *Theory of Microwave Remote Sensing*, A Wiley Interscience publication, John Wiley & Sons, Inc., New York, 1985.

Ulaby F. T., R. K. Moore, and A. K. Fung, Microwave Remote Sensing: Active and Passive, vol.II- Surface Scattering and Emission Theory, Addison Wesley, Reading (USA), 1982.

Ulaby F. T., R. K. Moore, and A. K. Fung, Microwave Remote Sensing: Active and Passive, vol.III- From Theory to Applications, Artech House, Dedham (USA), 1986.

Ulaby F.T. and C. Elachi, *Radar Polarimetry for Geoscience Applications*, Artech House: Norwood, 1992.

Ulaby F.T., R.K. Moore, and A.K. Fung, *Microwave Remote Sensing: Active and Passive*, vol. I, Addison-Wesley: Reading (MA), 1981.

Veysoglu, M.E., H.A. Yueh, R.T. Shin, and J.A. Kong, "Polarimetric passive remote sensing of periodic surfaces", *J. Electro. Waves Applic*., vol.5, n.3, pp. 267-280, 1991.

Wentz, F.J. and T. Meissner, "AMSR ocean algorithm", RSS tech. Proposal 121599A, Dec. 15, 1999.

Wentz, F.J., "Measurement of Oceanic Wind Vector Using Satellite Microwave Radiometers", *IEEE Trans. Geosci. and Rem. Sens*., vol.30, n.5, pp. 960-972, 1992.

Wentz, F.J., L.A. Mattox, and S. Peteherych, "New algorithms for microwave measurements of ocean winds: Applications to SEASAT and the Special Sensor Microwave Imager", *J. Geophys. Res.*, vol.19(C2), p. 2289-2307, 1986.

Wilheit, T.T., "A model for the microwave emissivity of the ocean's surface as a function of wind speed", *IEEE Trans. Geosci. Remote Sens.*, vol. 17, pp. 244-249, 1979.

Wu S.C., "Optimum frequencies of a passive microwave radiometer for tropospheric path-length correction", *IEEE Trans. Antennas Propag*., vol. 27, pp. 233-239, 1979

Yueh S. H., "Modeling of wind direction signals in polarimetric sea surface brightness temperatures", *IEEE Trans. Geosci. and Rem. Sens.,* vol. 35, pp. 1400-1418, 1997.

Yueh S.H., R. Kwok, F.K. Li, S.V. Nghiem, W.J. Wilson, and J.A. Kong, "Polarimetric Passive Remote Sensing of Ocean Wind Vectors", *Radio Science*, vol.29, n.4, pp. 799-814, 1994b.

Yueh S.H., S.V. Nghiem, W. Wilson, F.K. Li, J.T. Johnson, J.A. Kong, "Polarimetric Thermal Emission From Periodic Water Surface", *Radio Science*, vol.29, n.1, pp. 87-96, 1994a.

Yueh, H.A., R.T. Shin and J.A. Kong, " Scattering of electromagnetic waves from a periodic surface with random roughness", *J. Appl. Phys*. vol. 64, n.4, pp. 1657-1670, 1988.

Yueh, S. H., W. J. Wilson, S. J. Dinardo, and F. K. Li, "Polarimetric microwave brightness signature of ocean wind directions", IEEE Trans. Geosci. and Rem. Sens., vol. 37, pp. 949-959, 1999.

Yueh, S.H., and R. Kwok, "Electromagnetic fluctuations for anisotropic media and the generalized Kirchhoff's law", *Radio Science*, 28, pp. 471-480, 1993.

Yueh, S.H., W.J. Wilson, F.K. Li, S.V. Nghiem, W.B. Ricketts, "Polarimetric Measurements of Sea Surface Brightness Temperatures Using an Aircraft K-band Radiometer", IEEE Trans. Geosci. and Rem. Sens., Vol.33, n.1, pp. 85-92, 1995.

APPENDIX A.1

Superimposed and almost coincident data from SSM/I and TMI available over the calibration training areas in the year 2000, separately listed with respect to Land and Sea background surfaces. The table basically specifies for each spaceborne radiometer the box crossing time of the considered orbit and corresponding RAOB available data. In bold are listed the dates which have been selected for ECMWF data acquisition and consequent model evaluation during Phase-1.

Land – Amazon calibration area

DMSP SSM/I TDR	Box crossing time (GMT) or Orbit start time (GMT)	RAOB (GMT)	ECMWF analysis
27/4/1999	12:24	24:00	
5/1/2000	**23:11**	**24:00**	**24:00**
7/1/2000	12:35	12:00	
6/4/2000	23:40	24:00	
7/4/2000	**11:48**	**12:00**	**12:00**
5/7/2000	**12:43**	**12:00**	**12:00**
5/7/2000	23:16	No data	
19/11/2000	**23:25**	**24:00**	**24:00**
20/11/2000	12:49	12:00	
TRMM TMI	Box crossing time (GMT) or Orbit start time (GMT)	RAOB	
27/4/1999	11:31	24:00	
5/1/2000	**22:48**	**24:00**	
6/1/2000	10:58	12:00	
6/4/2000	23:08	24:00	
7/4/2000	**11:18**	**12:00**	
5/7/2000	**12:07**	**12:00**	
6/7/2000	00:18	No data	
20/11/2000	**01:13**	**00:00**	
20/11/2000	13:24	12:00	

Land – Sahara calibration area

DMSP SSM/I TDR	Box crossing time (GMT) or Orbit start time (GMT)	RAOB	ECMWF analysis
16/1/2000	**15:16**	**12:00**	**12:00**
28/1/2000	03:59	00:00	
2/4/2000	**15:56**	**12:00**	**12:00**
27/4/2000	05:17	00:00, 12:00	
19/7/2000	**14:55**	**12:00**	**12:00**
24/7/2000	05:06	00:00, 12:00	
14/10/2000	14:50	12:00	
29/10/2000	**04:32**	**00:00**	**00:00**
TRMM TMI	Box crossing time (GMT) or Orbit start time (GMT)	RAOB	
16/1/2000	**11:26**	**12:00**	
27/1/2000	21:33	24:00	
2/4/2000	**11:04**	**12:00**	
26/4/2000	22:33	24:00	
19/7/2000	**10:57**	**12:00**	
24/7/2000	00:31	00:00	
14/10/2000	12:34	12:00	
28/10/2000	**23:34**	**24:00**	

Land – Antarctica calibration area (MAWSON AUS-BASE)

DMSP SSM/I TDR	Box crossing time (GMT)	RAOB	ECMWF analysis
4/1/2000	**23:24**	**24:00**	**24:00**

5/1/2000	18:44	24:00	
5/4/2000	18:39	12:00, 24:00	
5/4/2000	**23:34**	**24:00**	**24:00**
30/6/2000	22:48	24:00	
1/7/2000	**18:44**	**12:00, 24:00**	**18:00,**
16/10/2000	22:43	24:00	
17/10/2000	**19:12**	**12:00, 24:00**	**18:00**

Atmosphere/Sea – Pacific Ocean (Hawaii islands) calibration area

TRMM TMI	Box crossing time (GMT)	RAOB	ECMWF analysis
8/3/2000	**11:26**	**12:00**	**12:00**
22/3/2000	21:33	24:00	
1/4/2000	11:04	12:00	
24/4/2000	22:33	24:00	
9/5/2000	10:57	12:00	
24/7/2000	00:31	00:00	
15/5/2000	12:34	12:00	
8/6/2000	23:34	24:00	
10/6/2000	11.30	12:00	
2/7/2000	23.47	24:00	
23/7/2000	**12.53**	**12:00**	**12:00**
11/8/2000	10.53	12:00	
17/8/2000	00.22	00:00	

Atmosphere/Sea – North Atlantic calibration area (Capo Verde Island)

DMSP SSM/I TDR	Box crossing time (GMT)	RAOB	ECMWF analysis
27/4/1999	**12:24**	**NO**	**12:00**
7 /3/2000	**11.21**	**12:00**	**12:00**
31/3/2000	23:45	NO	
5 /4/2000	**11.25**	**12:00**	**12:00**
4 /5/2000	11.20	12:00	
24 /5/2000	11.45	12:00	
2 /6/2000	11.20	12:00	
7 /6/2000	11.50	12:00	
8 /7/2000	11.20	NO	
1/8/2000	23.40	NO	
12 /7/2001	**11.20**	**12:00**	**12:00**
30 /8/2001	11.20	12:00	
TRMM TMI	Box crossing time (GMT)	RAOB	
27/4/1999	**11:31**	**NO**	
7 /3/2000	**12:05**	**12:00**	
31 /3/2000	23:32	NO	
5 /4/ 2000	**12.40**	**12:00**	
24 /5/2000	11.36	12:00	
7 /6/2000	12.25	12:00	
8 /7/2000	12:10	12:00	
1/8/2000	23.38	12:00	
12/7/2001	**12.25**	NO	
30/8/2001	11.24	NO	

Atmosphere/Sea – South Atlantic (Gough Island) calibration area

DMSP SSM/I TDR	Box crossing time (GMT) over Gough island	RAOB	ECMWF analysis
27/4/1999	**12.24**	**23:00**	**12:00**
10/3/2000	23.18	24:00	

2/4/ 2000	23.01	24:00	
15/5/ 2000	23.06	24:00	
20/6/2000	**23.07**	**24:00**	**24:00**
12/7/2000	23.02	24:00	
9/8/2000	23.12	24:00	
DMSP SSM/I TDR	Box crossing time (GMT)	RAOB	
27/4/1999			
1/3/2000	22.27	24:00	
9/4/ 2000	**23.05**	**24:00**	**24:00**
29/5/ 2000	22.32	24:00	
1/6/2000	22.27	24:00	
15/7/2000	22.21	24:00	
28/8/2000	22.23	24:00	
TRMM TMI	Box crossing time (GMT)	RAOB	
27/4/1999			
1/3/2000	22.44	24:00	
9/4/ 2000	**24.00**	**24:00**	**24:00**
29/5/ 2000	23.29	24:00	
1/6/2000	23.04	24:00	
15/7/2000	23.15	24:00	
28/8/2000	23.25	24:00	

Atmosphere/Sea – Indian Ocean (Cocos island) calibration area

DMSP SSM/I TDR	Box crossing time (GMT)	RAOB	ECMWF analysis
19/3/2000	23.00	24.00	
11/4/2000	**12.00**	**12:00**	**12:00**
13/4/2000	11.36	12:00	
5/5/2000	23.10	24:00	
16/6/2000	11.30	12:00	
21/6/2000	**23.18**	**24:00**	**24:00**
16/7/2000	11.51	12:00	
31/7/2000	**12.02**	**12:00**	**12:00**
5/8/2000	23.49	24:00	
22/8/2000	**23.33**	**24:00**	**24:00**
TRMM TMI	Box crossing time (GMT)	RAOB	
20/03/2000	00.08	00:00	
11/4/2000	**12.24**	**12:00**	
13/4/2000	11.36	12:00	
5/5/2000	23.54	24:00	
16/6/2000	11.48	12:00	
21/6/2000	**23.40**	**24:00**	
16/7/2000	11.09	12:00	
31/7/2000	**12.23**	**12:00**	
6/8/2000	00.14	00:00	
23/8/2000	**00.40**	**00:00**	

APPENDIX A.2

Catalog with all available acquisitions of RA-2 in PRESET LOOP MODE with relevant ancillary information

n°	site	orbit#	date	in-time	in-lat	In-lon	fin-time	fin-lat	fin-lon	NOTE
1	HOLL	2960	23-SEP-2002	20:53:02	49.485	6.677	20:54:28	54.516	4.283	A
2	HOLL	3003	26-SEP-2002	20:58:43	49.313	5.316	21:00:18	54.795	2.701	A
3	NATL	3084	02-OCT-2002	13:13:02	37.419	-41.664	13:14:40	31.648	-43.354	
4	SHR	3096	03-OCT-2002	09:23:28	25.937	13.328	09:25:06	20.137	11.891	
5	NATL	3106	04-OCT-2002	01:31:11	16.574	-55.326	01:32:49	22.379	-56.714	C
6	HOLL	3111	04-OCT-2002	10:24:23	54.32	5.955	10:25:41	49.806	3.803	A
7	SATL	3119	05-OCT-2002	00:43:13	-41.423	-33.196	00:44:51	-35.684	-35.022	C
8	SATL	3161	07-OCT-2002	23:11:30	-30.433	-12.808	23:11:35	-30.105	-12.897	C
9	SATL	3197	10-OCT-2002	10:58:10	-24.597	-18.444	10:59:48	-30.375	-19.956	
10	NATL	3199	10-OCT-2002	14:01:54	37.421	-53.882	14:03:32	31.649	-55.572	
11	HOLL	3232	12-OCT-2002	20:55:57	49.474	5.96	20:57:26	54.63	3.502	A
12	SATL	3240	13-OCT-2002	11:03:54	-24.597	-19.878	11:05:34	-30.438	-21.407	
13	SATL	3262	15-OCT-2002	00:28:49	-41.441	-29.592	00:28:55	-41.118	-29.701	
14	SATL	3269	15-OCT-2002	11:41:15	-24.569	-29.209	11:41:22	-24.96	-29.307	
15	ANTA	3279	16-OCT-2002	04:38:57	-65.284	61.333	04:40:36	-70.67	54.645	B
16	OCIN	3294	17-OCT-2002	05:29:11	0.392	67.79	05:30:48	-5.359	66.524	
17	GND	3301	17-OCT-2002	16:48:14	81.484	-8.956	16:49:53	79.92	-45.19	B
18	SHR	3318	18-OCT-2002	20:57:40	15.067	13.299	20:59:20	20.938	11.913	
19	NATL	3320	19-OCT-2002	00:19:50	18.472	-37.795	00:21:29	24.337	-39.223	
20	HOLL	3340	20-OCT-2002	10:21:24	54.612	6.832	10:22:53	49.455	4.376	A
21	NATL	3342	20-OCT-2002	13:47:31	37.431	-50.278	13:49:10	31.597	-51.985	
22	GND	3343	20-OCT-2002	15:14:41	80.579	-14.334	15:16:20	76.933	-38.95	D
23	GND	3344	20-OCT-2002	16:53:57	81.471	-9.039	16:55:36	80.026	-45.644	B
24	SHR	3590	06-NOV-2002	21:00:34	15.112	12.571	21:02:11	20.854	11.216	
25	SHR	3597	07-NOV-2002	09:23:27	25.878	13.322	09:25:04	20.144	11.903	
26	GND	3601	07-NOV-2002	15:48:36	81.237	-11.32	15:50:14	78.371	-40.97	D
27	HOLL	3612	08-NOV-2002	10:24:21	54.286	5.94	10:25:39	49.77	3.792	A
28	SHR	3640	10-NOV-2002	09:29:12	25.944	11.896	09:30:50	20.144	10.46	
29	NATL	3642	10-NOV-2002	12:49:41	28.475	-37.745	12:51:19	22.68	-39.223	
30	GND	3644	10-NOV-2002	15:54:19	81.291	-11.26	15:55:57	78.528	-41.542	D
31	AMZ	3671	12-NOV-2002	13:35:52	-2.816	-54.362	13:37:30	-8.631	-55.65	
32	NATL	3700	14-NOV-2002	14:01:54	37.411	-53.888	14:03:32	31.64	-55.577	C
33	NATL	3714	15-NOV-2002	13:30:17	37.412	-45.984	13:31:55	31.64	-47.673	
34	HOLL	3733	16-NOV-2002	20:55:57	49.474	5.96	20:57:25	54.569	3.535	A
35	SHR	3912	29-NOV-2002	09:32:02	25.948	11.178	09:33:40	20.148	9.743	
36	AMZ	3943	01-DEC-2002	13:38:29	-2.06	-54.912	13:40:07	-7.876	-56.197	
37	SHR	3962	02-DEC-2002	20:44:42	20.079	15.707	20:46:20	25.879	14.272	
38	HOLL	3962	02-DEC-2002	20:53:02	49.49	6.68	20:54:29	54.521	4.287	A
39	AUT	3976	03-DEC-2002	20:20:29	46.222	15.919	20:20:57	47.845	15.274	A
40	AUT	3998	05-DEC-2002	09:37:18	47.983	15.239	09:37:46	46.36	14.591	A
41	SHR	3132	05-OCT-2002	21:06:20	15.056	11.133	21:07:58	20.864	9.762	C
42	NATL	3141	06-OCT-2002	12:49:42	28.487	-37.746	12:51:20	22.691	-39.225	C
43	SATL	3212	11-OCT-2002	12:07:10	-24.63	-35.697	12:08:46	-30.343	-37.192	
44	NATL	3213	11-OCT-2002	13:30:18	37.375	-45.991	13:31:56	31.603	-47.679	
45	SHR	3232	12-OCT-2002	20:46:47	17.093	15.694	20:48:25	22.898	14.299	
46	NATL	3349	21-OCT-2002	00:56:41	16.616	-46.704	00:58:18	22.356	-48.076	
47	AMZ	3592	07-NOV-2002	01:54:28	-12.937	-56.625	01:56:06	-7.127	-57.93	
48	AMZ	3635	10-NOV-2002	02:00:14	-12.914	-58.072	02:01:52	-7.104	-59.377	
49	SATL	3662	11-NOV-2002	23:11:29	-30.399	-12.816	23:13:07	-24.621	-14.328	
50	HOLL	3232	12-OCT-2002	20:56:42	52.059	4.791	20:57:25	54.569	3.535	A

51	GND	3615	08-NOV-2002	15:17:30	80.637	-14.342	15:19:08	77.079	-39.108	D
52	GND	3616	08-NOV-2002	16:56:47	81.464	-8.884	16:58:25	80.127	-45.408	B
53	SHR	3633	09-NOV-2002	21:06:19	15.081	11.138	21:07:57	20.889	9.767	
54	SHR	3740	17-NOV-2002	09:10:30	21.022	15.694	09:12:08	15.214	14.322	
55	OCIN	3795	21-NOV-2002	05:29:12	0.43	67.785	05:30:50	-5.387	66.505	
56	AMZ	3800	21-NOV-2002	13:52:54	-2.077	-58.515	13:54:32	-7.892	-59.8	
57	GND	3802	21-NOV-2002	16:48:17	81.489	-8.911	16:49:55	79.962	-44.87	B
58	AUT	4456	06-JAN-2003	09:31:33	47.898	16.651	09:32:01	46.275	16.004	A
59	AUT	4477	07-JAN-2003	20:20:28	46.223	15.916	20:20:56	47.846	15.27	A
60	NATL	3850	25-NOV-2002	00:56:41	16.591	-46.702	00:58:19	22.397	-48.09	
61	AMZ	3864	26-NOV-2002	01:57:22	-12.89	-57.364	01:58:59	-7.146	-58.654	
62	GND	3906	28-NOV-2002	23:04:53	67.852	-37.747	23:06:31	73.069	-46.019	D
63	SHR	3819	22-NOV-2002	20:57:42	15.058	13.291	20:59:20	20.866	11.921	
64	NATL	3829	23-NOV-2002	14:19:08	37.409	-58.202	14:20:46	31.638	-59.891	
65	HOLL	3841	24-NOV-2002	10:21:24	54.609	6.814	10:22:52	49.514	4.386	A
66	GND	3844	24-NOV-2002	15:14:41	80.578	-14.441	15:16:19	76.973	-38.835	D
67	GND	3845	24-NOV-2002	16:53:57	81.474	-8.753	16:55:35	80.085	-45.139	B
68	ANTA	3861	25-NOV-2002	20:35:35	-79.834	77.581	20:37:13	-75.816	56.966	
69	SHR	3869	26-NOV-2002	09:26:20	25.903	12.599	09:27:58	20.103	11.164	
70	GND	3873	26-NOV-2002	15:51:28	81.259	-11.503	15:53:06	78.43	-41.389	D
71	AMZ	3900	28-NOV-2002	13:33:50	-6	-54.342	13:35:28	-11.813	-55.642	
72	AMZ	5367	11-MAR-2003	01:57:21	-12.908	-57.357	01:58:59	-7.097	-58.662	
73	GND	5409	13-MAR-2003	23:05:01	68.263	-38.274	23:06:32	73.053	-46.016	D
74	AMZ	5410	14-MAR-2003	02:03:06	-12.95	-58.786	02:03:10	-12.686	-58.846	
75	SATL	5480	18-MAR-2003	23:16:58	-41.436	-11.634	23:18:36	-35.697	-13.46	C
76	AMZ	5510	21-MAR-2003	01:43:44	-10.319	-54.352	01:45:22	-4.505	-55.645	
77	ANTA	5526	22-MAR-2003	04:04:42	-66.088	69.143	04:06:20	-71.381	62.097	B, C
78	SATL	5273	04-MAR-2003	11:41:12	-24.619	-29.217	11:42:50	-30.397	-30.73	
79	SHR	5279	04-MAR-2003	20:51:53	15.099	14.728	20:53:31	20.907	13.357	
80	SHR	5286	05-MAR-2003	09:14:46	25.924	15.49	09:16:24	20.124	14.054	
81	OCIN	5298	06-MAR-2003	05:29:08	0.432	67.796	05:30:46	-5.384	66.516	
82	AMZ	5303	06-MAR-2003	13:52:50	-2.06	-58.501	13:54:28	-7.875	-59.787	
83	GND	5305	06-MAR-2003	16:48:13	81.483	-8.989	16:49:51	79.95	-44.904	B
84	SHR	5322	07-MAR-2003	20:57:38	15.047	13.299	20:59:16	20.855	11.928	
85	SHR	5329	08-MAR-2003	09:20:33	25.906	14.044	09:22:11	20.106	12.608	
86	NATL	5346	09-MAR-2003	13:47:29	37.391	-50.293	13:49:07	31.62	-51.982	C
87	GND	5347	09-MAR-2003	15:14:38	80.59	-14.19	15:16:16	77	-38.686	C
88	ANTA	5364	10-MAR-2003	20:35:34	-79.832	77.641	20:37:12	-75.818	57.01	
89	SHR	5365	10-MAR-2003	21:03:25	15.085	11.851	21:05:03	20.893	10.479	
90	SHR	5372	11-MAR-2003	09:26:18	25.931	12.611	09:27:56	20.131	11.175	
91	AMZ	5403	13-MAR-2003	13:33:52	-6.049	-54.357	13:35:30	-11.861	-55.657	
92	SHR	5415	14-MAR-2003	09:32:04	25.906	11.166	09:33:42	20.106	9.73	
93	SHR	5508	20-MAR-2003	20:49:04	15.097	15.439	20:50:42	20.905	14.068	C
94	AMZ	5532	22-MAR-2003	13:50:00	-2.041	-57.784	13:51:38	-7.857	-59.069	C

A: NON INTERESTING ZONES

B: PASS OVER COASTAL ZONES

C: S-BAND DATA ERROR

D: NO SIMULATED DATA

APPENDIX A.3

Format of files exchanged among various project tasks.

FORMAT OF NUMERICAL WEATHER PREDICTION DATA INTERCHANGE VERSION 2.0

Fomat of files to interchange meteorological (analysis and/or forecast) data. Source files are NCEP or ECMWF data in GRIB format. The name of the file should contain "Time of data", "Box area identification" as reference information.
Revision 1.0 by Marzano, Pierdicca, date 7/3/2002
Revision 2.0 by Pierdicca, date 3/3/03: It includes liquid water and ice profiles coming from forecasts standard pressure levels

The format and file content is the following:

HEADER RECORD [7 data ASCII]
>Number of gridpoints within the file
>Year
>Month
>Day
>Hour
>Minute
>Data Source [ECMWF analysis=1, NCEP analysis =2, RAOB=3, ECMWF forecast=11, NCEP forecast=12]

---------- One block for each grid point
RECORD 1 [19 data ASCII]
>Data-block sequential number
>x-Grid point number
>y-Grid point number
>latitute from –90° tp +90° [deg]
>longitude from 0° to 360° [deg]
>number NL of levels of profile data (depending on data source)
>Year
>Month
>Day
>Hour
>Minute
>land-sea mask [(0,1)]
>Total column water (vapor+drops+ice) [kg/m2]
>Total column water vapor [kg/m2]
>cloud cover total [0-1]
>cloud low [0-1]
>cloud mid [0-1]
>cloud high [0-1]
>cloud convective [0-1]

RECORD 2 [25 data ASCII]
>geopotential (orography) [m2 s-2]
>soil temperature levels 1 (0-7 cm down) [K]
>soil temperature levels 2 (7-28 cm)[K]
>soil temperature levels 3 (28-100) [K]
>soil temperature levels 4 (100-255) [K]
>soil wetness level 1 (come sopra) [m (H20)]
>soil wetness level 2 (come sopra) [m (H20)]
>soil wetness level 3 (come sopra) [m (H20)]
>soil wetness level 4 (come sopra) [m (H20)]
>Snow Depth [m]
>Mean Sea Level Pressure [Pa]
>u-wind at 10 m [ms-1]
>v-wind at 10 m [ms-1]
>Temperature at 2 m [K]
>Dewpoint at 2 m [K]
>sfc roughness [m]
>Standard deviation of orography
>Anisotropy of subgrid scale orography
>Angle of subgrid scale orography
>Slope of subgrid scale orography
>sfc vegetation cover [%]
>apparent sfc humidity [kg/kg]

>log sfc roughness
>skin temperature [K]
>Surface Pressure [Pa]

ARRAY [NL levels x 8 data (x 10 data for Data Source =11 or 12) ASCII] => 1 record of 8 (10 data for Data Source =11 or 12) data for each level containing:
>pressure [hPa]
>height [m]
>temperature [K]
>relative humidity [%]
>specific humidity [kg/kg]
> add new TBD data (present if Data source =11 or 12)
> add new TBD data (present if Data source =11 or 12)
>u-component of wind [ms-1]
>v-component of wind [ms-1]
>vertical velocity [Pa s-1]
---------- End of block for

FORMAT OF ATMO MODULE DATA INTERCHANGE VERSION 2.3

Fomat of files to interchange the output of the atmospheric Work Package 1.3 during Phase 1. Source files of WP 1.3 are RAOB data or Numerical weather prediction data (ECMWF/NCEP) or radiometer data (Envisat-MWR, TRMM-TMI, DMSP-SSM/I). The file contains simulated values of Mean Radiative Temperaure Tmrup and Tmrdn [K] (Tmrup for the upward direction and Tmrdn for the downward directions) and atmospheric opacity tau [Neper] computed from the input data at the relevant frequency channels of 3.2 13.575 10.6 19.3 21.2, 22.3, 37. GHz (i.e., SSM/I, TMI, MWR). It also contains flags about cloud cover and rain, integrated water vapour IPWV and liquid water ILC as given by the RTE model as well as few meteorological parameters at the first profile level (T1 and Rh1). The last are not necessarily surface data (such as in the case of radiosounding source) and therefore they should be used for emissivity computation only in case surface data are not available.
Revision 1.1 by Bonafoni, date 4/4/2002.
Revision 2.3 by Pierdicca, date 3/3/03: it includes indication of Liebe model version, cloud absorbtion model, more data sources (i.e., forecasts) in the header. It include more channel in the water vapour absorbtion line.

The format and file content is the following.

From record 1 to record 9: Header records containing self-explaining information about source of data and file format, number of simulation point (NPOINT) and observation angle THETA, version of Liebe model.

From record 10 to record NPOINT+10: NPOINT records each of them corresponding to each simulation point (RAOB location or meteo analysis grid point, or radiometer pixel) [36 data ASCII]

Columns:
1 Numerical code to identify source of input (ECMWF=1, NCEP=2, RAOB=3, SSMI=4, TMI=5, ECMWF forecast=11, NCEP forecast=12]
2 year
3 month
4 day
5 hour
6 lat
7 lon
8-15 Tmrup [K] at 3.2 13.575 10.6 19.3 21.2 22.3 23.8 37. GHz at observation angle THETA as indicated in the file name convention
16-23 Tmrdn [K] at 3.2 13.575 10.6 19.3 21.2 22.3 23.8 37. GHz at observation angle THETA as indicated in the file name convention
24-31 Tau [Np] at 3.2 13.575 10.6 19.3 21.2 22.3 23.8 37. GHz at observation angle THETA as indicated in the file name convention
32 Integrated water vapor IPWV [cm] as computed by the RTE model
33 Integrated liquid [cm] as computed by the RTE model
34 flag_rain identifyng presence of rain (0: no rain, 1: presence of rain, -99 flag not available)
35 temperature of first level of profile T1 [K] (it is not necessarily the surface skin temperature)
36 Pressure [mb]
37 Relative humidity of first level of profile Rh1 (it is not necessarily the soil moisture)
---------- End of file

FORMAT OF RA-2 DATA INTERCHANGE. VERSION 1.1

Format of the file containing the RA-2 data in Passive Calibration mode, their time and location and co-located brightness temperature values from different sensors (ENVISAT-MWR, DMSP-SSM/I, TRMM-TMI).

Source of the file: Task Data processing, Dept. Electronic Engineering
Destination of the file: Task ATMO (Perugia), LAND (Tor Vergata), SEA (La Sapieza")
Name of the file (extension ".clc") is: ZZZ(Z)_YYYYMMDD_hhmmss.clc

ZZZ(Z) indicates the geographical area (3 o 4 characters) (AMZ=Amazzonia, SHR=Sahara, GND=Groenlandia, NATL=Nord Atlantico, SATL=Sud Atlantico, OCIN=Oceano Indiano, ANTA=Antartico, OCPA=Oceano Pacifico) , YYYY is the year, MM is the month, DD is the day, hh mm and ss are hour minute and second, respectively.

The format is:

HEADER RECORD 1 [9 data ASCII]
> NRA2: total number of RA-2 data acquisition (it does not include number of header records) [ASCII]
> name of the TMI file [ASCII]
> name of the SSM/I file [ASCII]
> name of the MWR file [ASCII]
> day of processing [ASCII]
> month of processing [ASCII]
> day of processing [ASCII]
> time of processing: hour:min:sec [ASCII STRING]
> year of processing [4 ASCII)

HEADER RECORD 2 [27 data ASCII]

It contains the acronyms of the parameters of columns in the data record columns [27 ASCII STRINGS] ARRAY [NRA2 record x 27 data] [27 ASCII per record] (–99.99 indicates lack of data)

Col .1: Julian time of the RA-2 sample (fractions of day since the first day of the year)
Col. 2-3: lat & lon RA-2 (degrees)
Col. 4-5: Digital Count RA-2 (Ku & S bands)
Col. 6-7: TB MWR (23.8 & 36.5 GHz) (K)
Col. 8: Time difference, in fractions of hour, between the acquisition of the RA-2 pixel and that of the associated TMI pixel
Col. 9: Distance (Km) between the RA-2 pixel and the associated TMI pixel
Col.10-18: TB TMI (K)
Col. 19: Time difference, in fractions of hour, between the acquisition of the RA-2 pixel and that of the associated SSM/I pixel
Col. 20: Distance (Km) between the RA-2 pixel and the associated SSM/I pixel
Col.21-27: TB SSM/I (K)

---------- End of file

TB @ 85 GHz for DMSP-SSM/I and TRIMM-TMI are averaged inside low resolution pixel.

FORMAT OF RA-2 "HIGH RESOLUTION" DATA INTERCHANGE. VERSION 1.1

Format of the file containing the RA-2 data in Passive Calibration mode, their time and location and co-located brightness temperature values from different sensors (ENVISAT-MWR, DMSP-SSM/I, TRMM-TMI) at their high resolution band.

Source of the file: Task Data processing, Dept. Electronic Engineering
Destination of the file: Task ATMO (Perugia), LAND (Tor Vergata), SEA (La Sapieza")
Name of the file (extension ".clc") is: ZZZ(Z)_YYYYMMDD_hhmmss_hr.clc

ZZZ(Z) indicates the geographical area (3 o 4 characters) (AMZ=Amazzonia, SHR=Sahara, GND=Groenlandia, NATL=Nord Atlantico, SATL=Sud Atlantico, OCIN=Oceano Indiano, ANTA=Antartico, OCPA=Oceano Pacifico) , YYYY is the year, MM is the month, DD is the day, hh mm and ss are hour minute and second, respectively. The suffix hr indicates "high resolution" data.

The format is:

HEADER RECORD 1 [9 data ASCII]
> NRA2: total number of RA-2 data acquisition (it does not include number of header records) [ASCII]
> name of the TMI file [ASCII]
> name of the SSM/I file [ASCII]
> name of the MWR file [ASCII]
> day of processing [ASCII]
> month of processing [ASCII]
> day of processing [ASCII]
> time of processing: hour:min:sec [ASCII STRING]
> year of processing [4 ASCII)

HEADER RECORD 2 [23 data ASCII]

It contains the acronyms of the parameters of columns in the data record columns [23 ASCII STRINGS] ARRAY [NRA2 record x 23 data] [23 ASCII per record] (–99.99 indicates lack of data)

Col .1: Julian time of the RA-2 sample (fractions of day since the first day of the year)
Col. 2-3: lat & lon RA-2 (degrees)
Col. 4-5: Digital Count RA-2 (Ku & S bands)
Col. 6-7: TB MWR (23.8 & 36.5 GHz) (K)
Col. 8: Time difference, in fractions of hour, between the acquisition of the RA-2 pixel and that of the associated TMI pixel
Col. 9: Distance (Km) between the RA-2 pixel and the associated TMI pixel
Col.10-13: TB TMI (K) @85 GHz
Col. 14: Time difference, in fractions of hour, between the acquisition of the RA-2 pixel and that of the associated SSM/I pixel
Col. 15: Distance (Km) between the RA-2 pixel and the associated SSM/I pixel
Col.16-23: TB SSM/I (K) @85 GHz

---------- End of file

FORMAT OF RA-2 "WATER CONTENTS" DATA INTERCHANGE. VERSION 1.0

Format of the file containing the RA-2 data in Passive Calibration mode, their time and location and co-located brightness temperature values from ENVISAT-MWR.
Source of the file: Task Data processing, Dept. Electronic Engineering
Destination of the file: Task ATMO (Perugia), LAND (Tor Vergata), SEA (La Sapieza")
Name of the file (extension ".clc") is: ZZZ(Z)_YYYYMMDD_hhmmss_wc.clc

ZZZ(Z) indicates the geographical area (3 o 4 characters) (AMZ=Amazzonia, SHR=Sahara, GND=Groenlandia, NATL=Nord Atlantico, SATL=Sud Atlantico, OCIN=Oceano Indiano, ANTA=Antartico, OCPA=Oceano Pacifico) , YYYY is the year, MM is the month, DD is the day, hh mm and ss are hour minute and second, respectively. The suffix wc indicates "water contents" data.

The format is:

HEADER RECORD 1 [7 data ASCII]

> NRA2: total number of RA-2 data acquisition (it does not include number of header records) [ASCII]
> name of the MWR file [ASCII]
> day of processing [ASCII]
> month of processing [ASCII]
> day of processing [ASCII]
> time of processing: hour:min:sec [ASCII STRING]
> year of processing [4 ASCII)

HEADER RECORD 2 [11 data ASCII]

It contains the acronyms of the parameters of columns in the data record columns [11 ASCII STRINGS]

ARRAY [NRA2 record x 11 data] [11 ASCII per record] (–99.99 indicates lack of data)

Col .1: Julian time of the RA-2 sample (fractions of day since the first day of the year)
Col. 2-3: lat & lon RA-2 (degrees)
Col. 4-5: Digital Count RA-2 (Ku & S bands)
Col. 6-7: TB MWR (23.8 & 36.5 GHz) (K)
Col. 8: Water vapour content (Kg/m2)
Col. 9: Cloud liquid water content (Kg/m2)
Col.10-11: Attenuations in S-band and Ku-band (dB)

---------- End of file

FORMAT OF SIMULATIONS DATA INTERCHANGE. VERSION 1.0

Format of the file containing the simulation corresponding to each point of the "RA2 data interchange file" at the frequency of RA-2 (S and Ku) and ENVISAT-MWR, DMSP-SSM/I, TRMM-TMI (except the higher Frequency 85 GHz channels).

Source of the file: LAND (Tor Vergata), SEA (La Sapienza")

Destination of the file: Task Data processing, Dept. Electronic Engineering
Name of the file (extension ".sim"): same of the "RA-2 data interchange file", except for extension.

For each record of the NRA2 record of the "RA2 data interchange file" , a record with the simulated TB has to be produced. Therefore the number of records of the simulation file must be the same of the RA-2 one.

The format is:

HEADER RECORD 1 [8 data ASCII]

> NSIM: total number of simulation data point (it does not include number of header records). Same as the corresponding "RA2 data interchange file" [ASCII]
> name of the RA-2 file [ASCII]
> name of the ECMWF-ATMO file containing the atmospheric data [ASCII]
> time of processing [ASCII]

HEADER RECORD 2 [8 data ASCII]

It contains the acronyms of the parameters of columns in the data record columns [14 ASCII STRINGS], ARRAY [NSIM record x 14 data] [14 ASCII per record] (–99.99 indicates lack of data)

Col. 1-2: lat & lon of the RA-2 data sample (degrees)
Col. 3-4: lat & lon of the ECMWF-ATMO pixel associated to the RA-2 one (degrees)
Col. 5-6: simulated TB at S and Ku band, at nadir (K)
Col. 7-16: simulated TB at 10GHz v pol. , 10 GHz h pol., 19 GHz v pol., 19 GHz h pol., 21 GHz v pol., 22 GHz v pol., 23.8 GHz nadir, 37 GHz v pol., 37 GHz h pol., 37 GHz nadir (K)

---------- End of file